University of Alberta

PREDICTION OF PERFORMANCE OF LARGE SYNCHRONOUS MACHINES WITH SKEWED STATORS

by

Svetlana G. Troitskaia

A thesis submitted to the Faculty of Graduate Studies and Research in partial fulfillment of the requirements for the degree of **Doctor of Philosophy**.

in

Power Engineering and Power Electronics

Department of Electrical and Computer Engineering

Edmonton, Alberta
Fall 2008

Library and Archives Canada

Published Heritage Branch

395 Wellington Street
Ottawa ON K1A 0N4
Canada

Bibliothèque et Archives Canada

Direction du Patrimoine de l'édition

395, rue Wellington
Ottawa ON K1A 0N4
Canada

Your file Votre référence
ISBN: 978-0-494-46440-3
Our file Notre référence
ISBN: 978-0-494-46440-3

NOTICE:
The author has granted a non-exclusive license allowing Library and Archives Canada to reproduce, publish, archive, preserve, conserve, communicate to the public by telecommunication or on the Internet, loan, distribute and sell theses worldwide, for commercial or non-commercial purposes, in microform, paper, electronic and/or any other formats.

The author retains copyright ownership and moral rights in this thesis. Neither the thesis nor substantial extracts from it may be printed or otherwise reproduced without the author's permission.

AVIS:
L'auteur a accordé une licence non exclusive permettant à la Bibliothèque et Archives Canada de reproduire, publier, archiver, sauvegarder, conserver, transmettre au public par télécommunication ou par l'Internet, prêter, distribuer et vendre des thèses partout dans le monde, à des fins commerciales ou autres, sur support microforme, papier, électronique et/ou autres formats.

L'auteur conserve la propriété du droit d'auteur et des droits moraux qui protège cette thèse. Ni la thèse ni des extraits substantiels de celle-ci ne doivent être imprimés ou autrement reproduits sans son autorisation.

In compliance with the Canadian Privacy Act some supporting forms may have been removed from this thesis.

While these forms may be included in the document page count, their removal does not represent any loss of content from the thesis.

Conformément à la loi canadienne sur la protection de la vie privée, quelques formulaires secondaires ont été enlevés de cette thèse.

Bien que ces formulaires aient inclus dans la pagination, il n'y aura aucun contenu manquant.

Canada

Abstract

Large synchronous machines produce the majority of electric energy in Canada. To improve quality of the electric energy, manufacturers skew stators of these machines. Skewing causes axial shifting of magnetic fields, so that power losses in these machines differ from the losses in unskewed machines. Numerical methods are incapable of analyzing a large skewed machine in a reasonable time. To evaluate losses, fast simulation tools have been needed to aid designers of skewed synchronous generators at a preliminary stage of design.

This work is devoted to analytical modeling of harmonic magnetic fields, harmonic currents and high-frequency energy losses in large synchronous generators with skewed stators. A fast and accurate simulation tool has been developed on the basis of the model; it can be used for preliminary design of a skewed synchronous machine.

Acknowledgements

I would like to thank my research adviser Professor A. M. Knight for organization and management of this project, for guidance and support.

I wish to thank Vladimir Troitsky for discussions on algorithms, mathematics, debugging programs, for installing Debian Linux on computers at home and at work. I am thankful to Yang Zhan for questions and discussions, leading to better understanding of theory of a skewed synchronous machine.

I would like to acknowledge support of General Electric Canada, who provided input data, test and FEA results. This work has been funded by GE Canada and NSERC via the Collaborative Research Grant Program.

Table of Contents

1 Introduction 1

2 Construction of a salient-pole synchronous machine 4
- 2.1 Basic construction . . . 4
- 2.2 Modeling of the rotor quantities . . . 5
- 2.3 Construction of three-phase double-layer windings . . . 6
  - 2.3.1 Integral slot windings . . . 8
  - 2.3.2 Fractional slot windings . . . 10
- 2.4 Skew . . . 11
  - 2.4.1 Definition of skew . . . 11
  - 2.4.2 Voltage in a skewed winding and the skew coefficient . 12
  - 2.4.3 Damping of noise with skew . . . 15

3 Literature review 16
- 3.1 Machine models . . . 16
- 3.2 Prediction of magnetic field . . . 18
  - 3.2.1 Analytical methods to predict magnetic field . . . 18
  - 3.2.2 Numerical methods to predict magnetic field . . . 20
- 3.3 Prediction of losses . . . 21
  - 3.3.1 Iron losses due to magnetic fluxes . . . 21
  - 3.3.2 Currents in conductors and ohmic losses . . . 22
  - 3.3.3 Iron loss due to interbar currents . . . 23
- 3.4 Summary . . . 24

4 Prediction of air gap magnetic fields 25
- 4.1 Calculation of air gap permeance . . . 26
  - 4.1.1 Air gap permeance due to the pole shape . . . 26
  - 4.1.2 Air gap permeance due to the damper slotting . . . 31
  - 4.1.3 Air gap permeance due to the pole shape and the damper slotting . . . 34
  - 4.1.4 Air gap permeance due to the stator slotting . . . 35
  - 4.1.5 Air gap permeance due to the pole shape, damper slotting, and stator slotting . . . 36
- 4.2 Calculation of air gap MMF . . . 36
  - 4.2.1 Field mmf . . . 37

4.2.2 Armortisseur currents and mmf 38

5 Prediction of losses that depend on skew **49**
5.1 Magnetic field in iron of the stator 49
5.1.1 Magnetic flux density in the stator tooth 49
5.1.2 Stator back fluxes in open circuit 52
5.2 Formulae for iron loss evaluation 55
5.2.1 Traditional eddy current loss 56
5.2.2 Excess loss 56
5.2.3 Hysteresis loss 56
5.3 Pole face loss 57
5.3.1 Computation of magnetic field in a lamination 57
5.3.2 Eddy current density in a lamination 61
5.3.3 Computation of the pole face loss 61

6 Validation of the analytical model **62**
6.1 Prediction of magnetic flux density 62
6.2 Prediction of open circuit voltage 65
6.3 Prediction of losses 66
6.3.1 Open circuit losses 68
6.3.2 Short circuit losses 69

7 Design studies **72**
7.1 Losses 72
7.2 Damper bar currents 79
7.2.1 Bar currents in open circuit 80
7.2.2 Bar currents in short circuit 83
7.2.3 Bar currents versus skew value 83

8 Conclusion and recommendations for future work **90**

Bibliography **92**

A Conformal transformations **101**
A.1 The idea of the method 101
A.2 A symmetrical problem of the rectangular pole across the smooth armature 102
A.3 A problem of rectangular poles against the infinite smooth armature 105

B Calculation of eddy current loss density at one frequency **109**

C A product of two waves with axial phase shifts **110**

List of Tables

2.1 Pitch factor for a case of six slots per pole. 10

4.1 Impedance matrix of a damper network for a machine with 2 poles, 4 bars per pole, three slices. 43

6.1 Machine data. 62
6.2 RMS value of the phase voltage fundamental harmonic of the stator winding in the open circuit condition. 65
6.3 Calculated and measured open circuit losses. 69
6.4 Calculated and measured short circuit losses. 71

List of Figures

2.1 A salient pole synchronous machine. 5
2.2 Direct and quadrature axes. 6
2.3 MMF waveform versus winding design. 6
2.4 A coil and the coil pitch. 7
2.5 The n-th emf harmonic induced in the coil. 7
2.6 A double-layer integral slot full-pitch and short-pitched winding. 9
2.7 Calculation of the emf due to the coil group. 9
2.8 Skew. 12
2.9 A skewed coil. 13
2.10 Variation of magnetic path. 15

3.1 A multi-slice model of a skewed slot. 17
3.2 A *B-H* curve. 18
3.3 A cross-sectional interbar current model. 24

4.1 Functions to approximate the pole shape permeance. 27
4.2 Geometry of the pole and the stator. 29
4.3 Normalised permeance due to the pole shape, calculated from the model (left) and by FEA (right), on the half a pole pitch. 30
4.4 A mapping from α to θ_e. 32
4.5 Permeance due to the pole shape and damper slotting, calculated from the model (left), and the normalised permeance obtained by FEA (right), on the half a pole pitch. 35
4.6 The normalized permeance due to stator slotting. 35
4.7 37
4.8 *BH* linear and nonlinear characteristics. 38
4.9 Voltages in skewed bars. 39
4.10 Cross-sectional interbar current model. 40
4.11 A model of the damper winding including interbar currents. . 40
4.12 Mmf on the total rotor surface produced by one loop. 42
4.13 Indexing slices in the damper winding. 45
4.14 Mmf produced by a constant loop current. 46

5.1 Flux lines outside and inside the tooth. 50
5.2 Flux lines entering a stator packet. 51
5.3 A stator tooth partitioned in layers. 52

5.4 To the calculation of the tooth flux phase. 52
5.5 Fluxes outside and inside the stator yoke. 53
5.6 The magnetic circuit for stator flux calculation. 53
5.7 Magnetic flux density curve. 57
5.8 Cartesian coordinates for computation of magnetic field in the pole. 58
5.9 Equality of normal components of magnetic field density. . . . 60

6.1 Air gap flux density in Machine 5, obtained by test. 63
6.2 Air gap flux density in Machine 5, obtained by the model. . . 64
6.3 Measured variation in the magnitude of magnetic flux density fundamental with axial position for Machine 5. 64
6.4 Simulated variation in the magnitude of magnetic flux density fundamental with axial position for Machine 5. 64
6.5 Comparison of test, the model, and FEA results in Machine 1. 66
6.6 Comparison of test, the model, and FEA results in Machine 2. 66
6.7 Comparison of test, the model, and FEA results in Machine 3. 67
6.8 Comparison of test, the model, and FEA results in Machine 4. 67
6.9 Comparison of test, the model, and FEA results in Machine 5. 67
6.10 Phase voltage harmonics versus bar-to-iron resistance in Machine 1 and Machine 5 for the open circuit condition. 68
6.11 Relative permeability in rotor iron and pole face losses. 69
6.12 Open circuit total loss in Machines 1 and 3. 70
6.13 Open circuit total loss in Machine 5. 70
6.14 Short circuit total loss in Machines 1 and 3. 71
6.15 Short circuit total loss in Machine 5. 71

7.1 OC bar and inter-bar losses in Machine 1. 73
7.2 OC pole face and stator losses in Machine 1. 73
7.3 OC total loss in Machine 1. 73
7.4 OC bar and inter-bar losses in Machine 3. 74
7.5 OC pole face and stator losses in Machine 3. 74
7.6 OC total loss in Machine 3. 74
7.7 OC bar and inter-bar losses in Machine 5. 75
7.8 OC pole face and stator losses in Machine 5. 75
7.9 OC total loss in Machine 5. 75
7.10 SC bar and inter-bar losses in Machine 1. 76
7.11 SC pole face and stator losses in Machine 1. 76
7.12 SC total loss in Machine 1. 76
7.13 SC bar and inter-bar losses in Machine 3. 77
7.14 SC pole face and stator losses in Machine 3. 77
7.15 SC total loss in Machine 3. 77
7.16 SC bar and inter-bar losses in Machine 5. 78
7.17 SC pole face and stator losses in Machine 5. 78
7.18 SC total loss in Machine 5. 78

7.19 OC bar currents, 720 Hz, in Machine 1. 80
7.20 OC bar currents, 1440 Hz, in Machine 1. 81
7.21 OC bar currents, 720 Hz, in Machine 3. 81
7.22 OC bar currents, 1440 Hz, in Machine 3. 82
7.23 SC bar currents, 360 Hz, in Machine 1. 84
7.24 SC bar currents, 720 Hz, in Machine 1. 84
7.25 SC bar currents, 1080 Hz, in Machine 1. 85
7.26 SC bar currents, 1440 Hz, in Machine 1. 85
7.27 SC bar currents, 360 Hz, in Machine 3. 86
7.28 SC bar currents, 720 Hz, in Machine 3. 86
7.29 SC bar currents, 1080 Hz, in Machine 3. 87
7.30 SC bar currents, 1440 Hz, in Machine 3. 87
7.31 OC bar currents, 720 Hz, in Machine 1 and 5. 88
7.32 OC bar currents, 1440 Hz, in Machine 1 and 3. 88
7.33 SC bar currents, 720 Hz, in Machine 1 and 3. 89
7.34 SC bar currents, 1080 Hz, in Machine 1 and 5. 89
7.35 SC bar currents, 360 and 1440 Hz, in Machine 3 and 5. 89

A.1 Mapping from the z-plane to the w-plane. 102
A.2 A rectangular capacitor with infinitely stretched plates. 103
A.3 The pole and the armature of the same length. 103
A.4 The air gap in the z-plane and the w-plane. 103
A.5 Mapping from the z-plane to the $\psi\eta$-plane in a one-pole model. 106
A.6 Mapping from w-plane to xy-plane in a two-pole model. 108

List of Symbols

B magnetic flux density
E electromotive force (emf)
F magnetomotive force (mmf)
H magnetic field intensity
I current
J current density
K_p, K_d pitch and distribution coefficients
K_{skew}, K_s skew coefficient
L inductance
N number
P permeance, power loss
R resistance, radius of a circumference
S area
T period
V, v voltage
Z impedance, impedance matrix
d length, diameter, width
g length of the air gap
f frequency, function
k step, number
l length
m number of phases
n, m, k, i, j harmonic number
p number of pole pairs
q number of slots per pole per phase
r radius of a circumference
x magnetic flux
y span of an integral slot winding in stator slots
Δ penetration depth
β skew
β_s, β_{slot} angle, in electrical and mechanical radians, respectively
λ width, angle
λ_s, λ_{slot} slot pitch, in electrical and mechanical radians, respectively
μ magnetic permeability
ν magnetic reluctivity
τ pole pitch, in stator slots or radians
ψ flux linkage
Φ magnetic flux, phase

ω angular speed
$A, B, C, D, M, k, a, b, c, d, e, \sigma$ constants or coefficients
$\alpha, \beta, \gamma, \psi, \theta, \phi$ angles

Chapter 1

Introduction

Large synchronous machines may be found in a range of applications, either as generators or as large synchronous motors. Electric power generated using hydro electric plants is a large component of the electricity market; it comprises 59.6% of the electricity produced in Canada [1, 2] and 16.5% worldwide [3]. In 2005, large-scale hydro electric projects employing large generators produced 91.9% of the total hydro electric energy in the world [5]. These plants commonly use large low-speed salient-pole synchronous generators. Large synchronous motors have higher efficiency comparing to induction motors and are preferred in applications that require high horsepower and low speed, such as water pumping, flour mills, rubber mills and mixers, crushing and grinding [6]; they are sometimes used as traction motors and as synchronous condensers for power factor correction.

In some designs, manufacturers skew stators of large synchronous machines. The primary effect of *skewing*, or tilting, slots of a generator is improvement of the output voltage waveform. If harmonics exist in the voltage, they induce harmonic currents in conductors of electrical cables and loads; harmonic currents can cause excessive heating and premature aging of insulation. In motors, the induced harmonic currents create magnetic fields that can produce parasitic pulsating torques, resulting in a difficulty to start a motor or mechanical oscillations in a turbine-generator or a motor-load system [7]. Harmonic currents in power conversion apparatus can induce electric and magnetic fields, which impair performance of communication systems, metering equipment and data processing equipment. Harmonics in the input voltage can cause iron losses in transformers and motors, resulting in additional heating. The joule and iron losses increase with increase of frequency, so that higher-frequency harmonics may be more important to avoid than lower-order components [7]. Manufacturers specify voltage harmonic output of a generator in a form, for example, of a telephone interference factor (TIF), which rapidly increases with frequency [7]. To be competitive in the market, manufacturers strive to produce machines with an output voltage waveform close to a sinusoid, sometimes by skewing.

Another effect of skewing is reduction of audible noise in machines pro-

duced by magnetic tension force between the stator and the rotor slots. In most machines, the frequency of this noise is in the range of 700 Hz to 1400 Hz, where the human ear is most sensitive [8]. F. W. Carter emotionally described the effect of the noise on a human being [9]: "A persistent and penetrating sound, variously described as singing, howling, and whistling, which accompanies the working of certain rotating machines... The untoward character of the noise irritates the operator and his neighbours, whilst its erratic incidence has long perplexed the designer; for no sure means has hitherto been devised either for its avoidance or remedy. Designers are indeed often reduced to making tentative changes with the object of alleviating or curing the trouble, sometimes to the detriment of a machine in other respects". However, while skewing reduces the voltage harmonic spectrum and noise, it complicates the analysis of the machine performance.

Skew causes axial variation of magnetic flux density harmonics in the air gap between the rotor and the stator, affecting high-frequency losses, or *stray losses*. Stray losses in synchronous machines are the losses due to harmonic magnetic fluxes in iron and harmonic currents in windings and iron. Because they cannot be measured or calculated from measured quantities, stray losses are estimated using the following methods:

- calculating as 0.2-0.5% of the input power of a machine, according to IEC 34-2 or IEEE Standard 112 [10, 11, 12]

- using the electric-input method according to IEEE Standard 115-1995 [13]. The total loss curve consists of friction and windage, core and short-circuit losses. Extrapolation of the curve to zero armature current gives a value of loss in open circuit; this value corresponds to the sum of the friction and windage and core loss. "By subtracting this sum from the total loss at any armature current, the short-circuit loss for that armature current is obtained. The short-circuit loss is the sum of $I^2 R_a$ and stray-load losses. The stray-load loss is then determined by subtracting the armature $I^2 R_a$ loss calculated for the temperature of the winding during test" [13].

- using empirical formulas, based on test data from previously manufactured machines.

It has been noticed that losses are influenced by skew; however, these phenomena have not been well understood. Utility companies charge manufactures as much as $US 2000-5000 for 1kW of extra losses, so that manufacturers are concerned with better understanding of causes for losses and techniques for their evaluation. The existing methods described above may be unavailable or unreliable at the design stage, and they do not provide information about causes of stray losses and impact of design variables on stray losses. Investigation of literature shows abundance of analytical means to evaluate performance of skewed induction machines, but shortage of those for skewed

synchronous machines. Finite element analysis (FEA) can be used to verify the performance of skewed synchronous generators, but simulation times are prohibitive at the design stage, due to the large size of these machines. There is a clear need for new methods that would quickly analyze stray losses in a large skewed synchronous machine. Designs for machines could be improved if there was a tool available to provide a detailed picture of losses, and the cost of a skewed synchronous machine could be reduced.

A combination of analytical methods with FEA of an unskewed machine has recently become an attractive choice in machine analysis. While mathematical descriptions provide fast evaluation, data obtained with FEA provide accuracy and can be reused for a number of simulations. The combined approach has also been adopted in this work.

The goals of this work are to

- develop analytical models to predict performance of a large synchronous machine with a skewed stator
- develop software that evaluates losses using these models
- investigate the impact of design changes on stray and total losses

The thesis is structured as follows. Chapter 2 outlines construction of a salient-pole synchronous machine with a skewed stator, describes integral slot and fractional slot windings and shows calculation of the electromotive force (emf) in coils of these windings. Harmonic skew is defined, and expressions for harmonic voltages in the stator winding and for the harmonic skew coefficients in the skewed magnetic field are obtained. This background information is used in the following chapters. Chapter 3 reviews literature with respect to evaluation of magnetic fields and power losses in electric machines; some of the reviewed models are used to develop the analytical model. In Chapter 4, the air gap permeance and the air gap mmf harmonic series are modeled, including the mmf component formed by the armortisseur bar currents, and the air gap flux density is predicted by means of a permeance model. The obtained air gap flux density distribution serves as an input for modeling of flux distribution in the stator iron and evaluation of stator iron, pole face, damper bar and inter-bar losses in Chapter 5. Chapter 6 is devoted to validation of the analytical model, developed in Chapters 4 and 5, based on provided measurements. The impact of skew and inter-bar resistance on the loss components, the total loss, and the armortisseur current distribution is investigated in Chapter 7. Chapter 8 states contributions to the field, draws conclusions and recommendations on loss minimization.

Chapter 2

Construction of a salient-pole synchronous machine

This chapter is devoted to the basic construction of a low-speed, salient pole synchronous machine and to details of construction that are relevant to this work, such as construction of integral and fractional slot stator windings, skew. It is shown that a properly constructed double-layer stator winding reduces higher-order harmonics other than slotting harmonics in the stator voltage. The voltage in a skewed coil is obtained; the expression includes a novel definition of the harmonic skew coefficient. Skew is discussed as the means to reduce higher-order harmonics, including slotting harmonics, in the voltage waveform; to reduce audible noise, resulting from magnetic forces between the stator and the rotor.

2.1 Basic construction

A cross-section of a low-speed large synchronous machine is shown schematically in Fig. 2.1. As a rule, this machine has a large diameter and a small axial length [6]. It consists of stationary and rotating parts, called *stator* (sometimes *armature*) and *rotor*, respectively. The stator inner surface is slotted and contains a three-phase winding, wye-connected with the neutral earthed [8]. The rotor consists of a shaft, a spider ring fixed on the shaft, and multiple poles mounted on the rim of the spider ring [14]. The stator and the poles are assembled from laminations; the poles can be solid, cast or cut from steel. The stator is axially divided in packets distanced from each other for cooling; these air ways are called *air ducts*.

A field winding, made of copper or aluminum, is wound around each pole to provide magnetic flux. The direct current is supplied to the field winding either by a dc supply through slip rings and brushes [14] or a brushless exciter, which is most commonly an ac permanent magnet generator [15]. A damper winding is embedded in the surface of the *pole face*, or *shoe*, on each pole. It consists of copper or aluminum bars, interconnected similar to a squirrel cage.

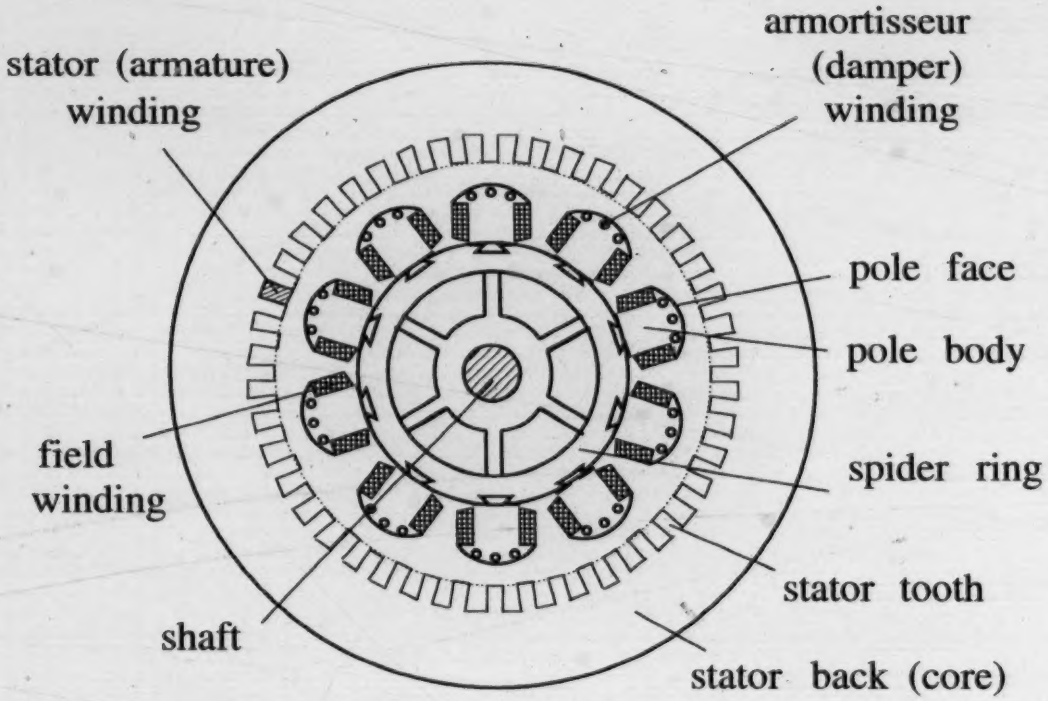

Figure 2.1: A salient pole synchronous machine.

In the case of a generator, as the prime mover (a hydro turbine, for example) rotates the rotor, the magnetic field produced by the field winding moves and induces voltage in the armature winding. If a three-phase load is connected to the stator winding, the voltage can be delivered to the load.

2.2 Modeling of the rotor quantities

A well recognized theory, called Park's transformation, considers electric quantities of a two-pole machine projected on a set of orthogonal coordinates d and q rotating with the synchronous speed. This representation allows one to consider the stator and the rotor equations simultaneously [16]. The model can be used to analyze multiple-pole machines on an electrical period of two poles. A synchronous machine is a convenient object for d-q analysis, because the rotor rotates with the synchronous speed.

In a salient-pole synchronous machine, the direct axis d is located along the pole, and the quadrature axis is the axis of symmetry between two poles (Fig. 2.2).

In this work, q-axis is used only as the origin for measuring phase angles of voltage, current and air gap quantities. It is assumed that the q-axis is aligned with the centre of a stator tooth at the time $t = 0$.

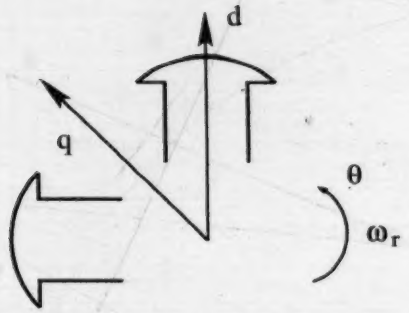

Figure 2.2: Direct and quadrature axes.

2.3 Construction of three-phase double-layer windings

The most common type of stator windings is a three-phase double-layer winding. A double-layer winding provides a magnetomotive force (mmf) waveform close to a sinusoid (Fig. 2.3). A double-layer integral-slot short-pitched winding is symmetrical, which allows one to manufacture identical coils [14].

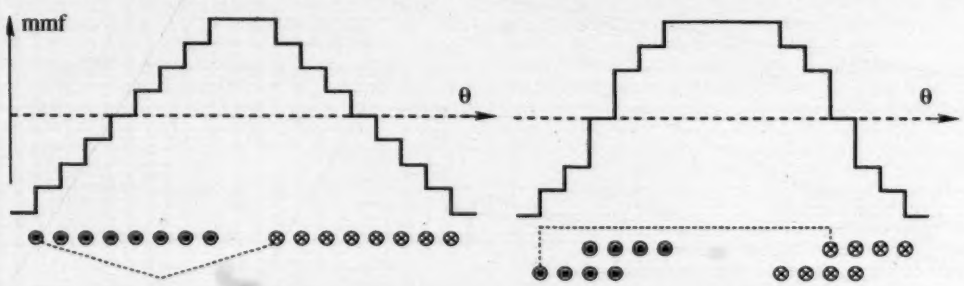

Figure 2.3: MMF waveform versus winding design.

A *coil* is defined as a closed loop of conducting material, and is located in two slots, as shown in Fig. 2.4. The coil can be described as being formed by two *coil sides*, separated by a *span* or *coil pitch* (measured in slots), and connected by end windings. A coil can be formed by one or more turns of wire.

An emf harmonic of the coil can be computed as the phasor difference of emf harmonics induced in the coil sides, as shown in Fig. 2.5. The coil pitch in electrical radians for the n-th harmonic is calculated as

$$\xi_n = n \frac{2\pi}{N_s} p\, y \tag{2.1}$$

where N_s is the number of slots in the stator, p is number of pole pairs, y is the span in slots. It is clear from Fig. 2.5 that the coil emf harmonic magnitude equals [14, 17]

$$E_{coil,n} = 2E_n \sin \tfrac{\xi_n}{2} \tag{2.2}$$

where E_n is the magnitude of the n-th voltage harmonic induced in one coil side.

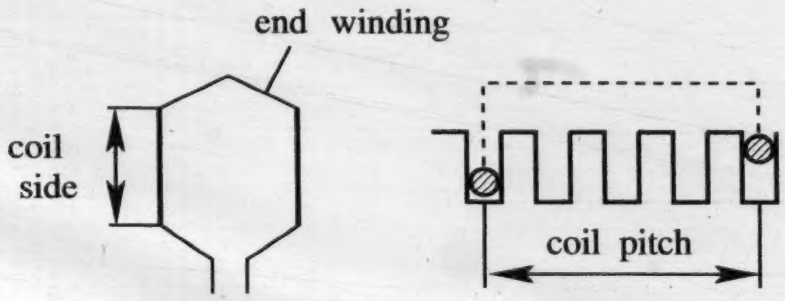

Figure 2.4: A coil and the coil pitch.

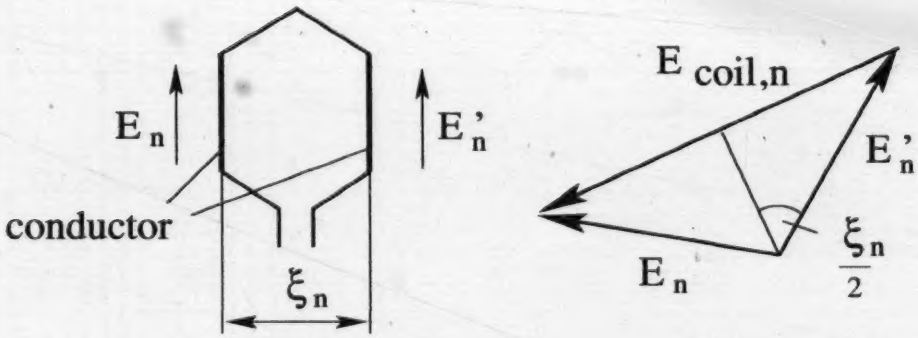

Figure 2.5: The n-th emf harmonic induced in the coil.

Alternatively, the n-th emf harmonic can be computed as

$$E_{coil,n} = N \frac{\partial}{\partial t} \int_S B_n \, dS \tag{2.3}$$

where N is the number of turns in the coil, B_n is the n-th flux density harmonic penetrating the coil (assuming the flux perpendicular to the cross-sectional area), S is the cross-sectional area of the coil.

Several coils, next to each other in one layer, can be connected in series and form a *coil group* of one phase. Coil groups of one phase are located under different poles; they can be connected in series, in parallel, or a combination of both, and provide the emf of the phase to be an arithmetical sum of emfs of the coil groups. In *parallel branches*, induced emfs have similar magnitudes and phase angles.

The *pole pitch* can be thought of as the number of slots per pole. The *number of slots per pole per phase* is calculated as

$$q = \frac{N_s}{2p\,m} \tag{2.4}$$

where m is the number of phases. If q is an integer, the winding is an *integral slot* winding. Otherwise, the winding is a *fractional slot* winding.

A three-phase double-layer winding has a capability to reduce induced voltage harmonics, produced by space harmonics of air gap magnetic field. However, there are harmonics of the space order [18]

$$n_s = k\frac{Ns}{p} \pm 1 = 2mq \pm 1 \tag{2.5}$$

called *slotting harmonics*, that are not affected by the double-layer winding construction. It is shown that these harmonics may be reduced or eliminated in the emf waveform using a fractional-slot winding or by *skewing* slots either on the stator or on the rotor.

2.3.1 Integral slot windings

If the span of the coil equals the pole pitch, the winding is called a *fully-pitched* winding. If the span is less, the winding is called *short-pitched*, or sometimes *fractional-pitch* or *chorded*, winding. These windings are schematically shown in Fig. 2.6.

In Fig. 2.6, a coil of phase A has the "going" side at a and the "returning" side at a'. Most frequently, a phase is chosen to occupy 60 electrical degrees per pole pitch [8, 17]. Fig. 2.6 illustrates that an integral slot winding is periodic with the pole pitch. This pattern facilitates computation of the phase emf. It is sufficient for analysis of properties of the winding to consider emf induced in a group of q coils.

Calculation of an emf harmonic in a coil group. The emf harmonics of q coils can be represented as phasors apart of each other by a slot pitch angle $n\gamma$, as shown in Fig. 2.7. [11, 17, 18]. Summation of the q coil emf phasors yields the coil group emf $E_{q,n}$. It can be seen that the coil emf phasors form a "circumference" of a radius R and the emfs can be expressed as

$$E_{coil,n} = 2R\sin\frac{n\gamma}{2} \tag{2.6}$$

$$E_{q,n} = 2R\sin\tfrac{n\alpha}{2} \tag{2.7}$$

where $\alpha = q\gamma$. The ratio of the phasor sum to the arithmetical sum of the coil emfs is called *distribution* factor [18]:

$$K_{d,n} = \frac{E_{q,n}}{qE_{coil,n}} = \frac{\sin\frac{n\alpha}{2}}{q\sin\frac{n\alpha}{2q}} \tag{2.8}$$

From (2.8), the emf harmonic of the coil group is

$$E_{q,n} = qE_{coil,n}K_{d,n} \tag{2.9}$$

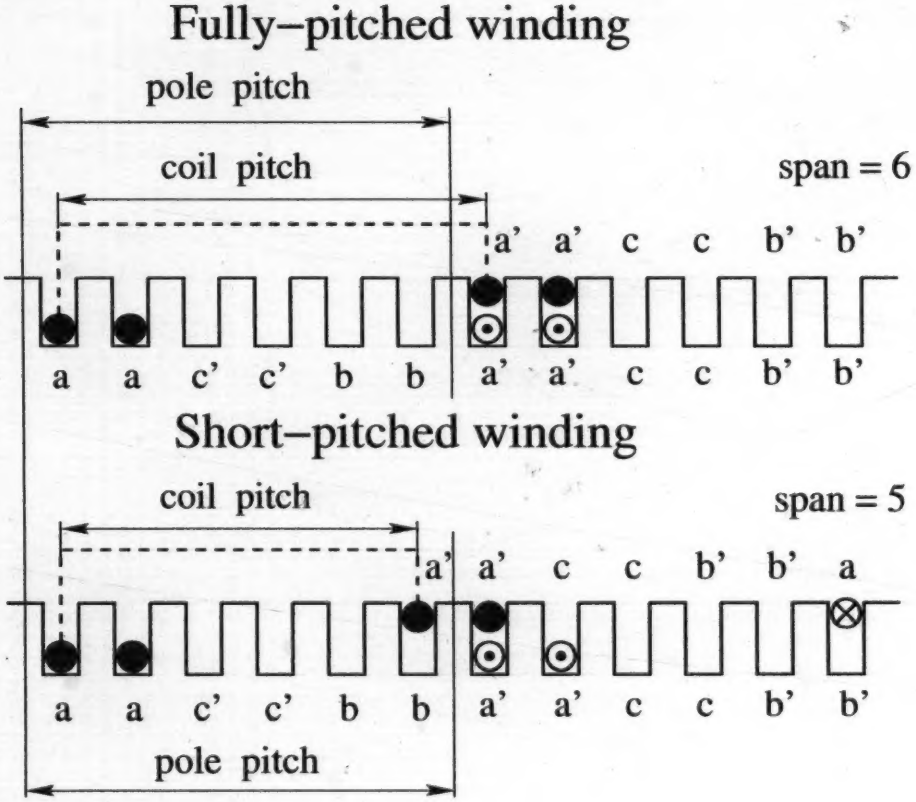
Fully–pitched winding
pole pitch
coil pitch
span = 6
a' a' c c b' b'
a a c' c' b b a' a' c c b' b'
Short–pitched winding
coil pitch
span = 5
a' a' c c b' b' a
a a c' c' b b a' a' c c b' b'
pole pitch

Figure 2.6: A double-layer integral slot full-pitch and short-pitched winding.

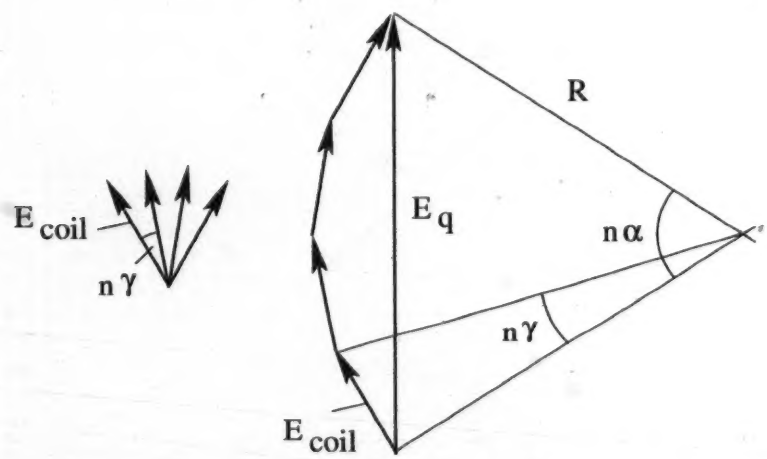

Figure 2.7: Calculation of the emf due to the coil group.

From (2.2)

$$E_{q,n} = 2qE_n \sin\tfrac{\xi_n}{2} K_{d,n} = 2qE_n K_{p,n} K_{d,n}, \tag{2.10}$$

where

$$K_{p,n} = \sin\frac{\xi_n}{2} \tag{2.11}$$

is called the *pitch* factor [18].

Improvement of the emf waveform. A shorter span than the number of slots per pole may reduce or eliminate a space harmonic. Table 2.1 illustrates variation of the pitch factor with span, in the case of an integral slot stator winding of six slots per pole. The pitch factor has been calculated using the equation (2.11), where the angle between the harmonic emfs of the coil sides is determined as

$$\xi_n = \frac{180^\circ}{6} \times \text{span} \times n \tag{2.12}$$

harmonic number	1	3	5	7	9
span = 6	1	-1	1	-1	1
span = 5	0.9659	-0.707	0.2588	0.2588	-0.707
span = 4	0.8660	0	-0.8660	0.8660	0

Table 2.1: Pitch factor for a case of six slots per pole.

One can see that changing the span (coil pitch) changes the pitch factor, reducing or eliminating the emf harmonics. A shorter span makes the magnitude of the fundamental emf to be less, because less area is enclosed by the coil, but the change is not significant.

However, for slotting harmonics the angle between the coils is

$$\gamma_{n_s} = n_s\gamma_1 = \left(k\frac{N_s}{p} \pm 1\right)\frac{2\pi p}{N_s} = 2\pi k \pm \gamma_1 \tag{2.13}$$

where γ_1 is the angle between the coils for the first harmonic. By the equations (2.11) and (2.8), the pitch and distribution factors remain the same for the first and a slotting harmonics. Therefore, the magnitude of the n-th slotting harmonic cannot be reduced much less than the magnitude of the fundamental by reducing the span.

With increase of q, the space order of slotting harmonics that show up in the emf waveform increases. Higher-order harmonics tend to be smaller with increase of the space order, so that increase of q improves the emf waveform.

In salient-pole synchronous machines, q cannot be high, as the number of slots per pole is limited by mechanical considerations.

2.3.2 Fractional slot windings

Fractional slot double-layer windings are often used in low-speed, multiple pole synchronous machines. The total number of slots must be a multiple of the

number of phases to maintain phase symmetry [8, 17, 18]. However, for a high number of poles the pole pitch is small and cannot spread under many stator slots with large conductors, so that it is not always possible to construct a machine with an integer number of slots per pole per phase.

An example below [18] illustrates the construction of a fractional-slot winding in a three-phase machine. If the machine has 10 poles, the number of slots must be 30 to have $q = 1$, or 60 for $q = 2$ by (2.4). Choosing 42 slots gives $q = \frac{42}{3\times10} = \frac{14}{10} = \frac{7}{5}$ slots per pole per phase. That means that 7 slots that belong to one phase should be distributed over 5 poles, suggesting that a pattern will repeat. If conductors of the phase occupy 1 or 2 slots over a pole, a slot pattern could be, for instance, 21121 or 11221 over the 5 poles.

Further constructing of the fractional slot winding may be done by an arbitrary choice of a coil span, checking that the pitch coefficient for the first harmonic is close to unity. In the example described, there are $7 \times 3 = 21$ slots in total distributed over 5 poles, and the coil pitch can be chosen 4 slots. If the pattern repeats after 21 slots, it is sufficient to draw the first 21 slots and insert a coil into each slot with the chosen span. The emf phasors of the coil sides can be drawn, taking care of the phase shift from slot to slot. One phase occupies 60 electrical degrees, so that all emf phasors within 60 degrees may be claimed to belong to one phase, and the corresponding coils are assigned to the phase. In this way, all coils may be assigned to a certain phase [18].

A winding with a fractional q may significantly reduce slotting harmonics. Slotting itself does not induce voltage harmonics in the stator winding. However, slotting may induce currents in the rotor, which produce a magnetic flux component that induces voltage harmonics in the stator. A fractional q allows only voltage slotting harmonics of the space orders described by (2.5) to be induced in the stator winding [17]. As the air gap magnetic field does not contain harmonics of fractional space orders, the greatest slotting harmonics are not present in the stator voltage waveform.

If the stator has a fractional slot winding, it is possible to produce a balanced winding with a winding pattern that does not repeat. In this case, it is necessary to consider the whole circumference of the machine to determine the emf induced in a phase.

2.4 Skew

2.4.1 Definition of skew

Skew is defined as the variation in the angular position of a conductor along the axial length of a machine. It is usually measured in slot pitches. As an example, a conductor with a skew of k slot pitches will undergo an angular shift such that if one end of the conductor is at the position θ_1, the other end will be at the angular position $\theta_1 + \beta$, where β is the skew in mechanical

radians (Fig. 2.8):

$$\beta = \frac{kN_s}{2\pi} \tag{2.14}$$

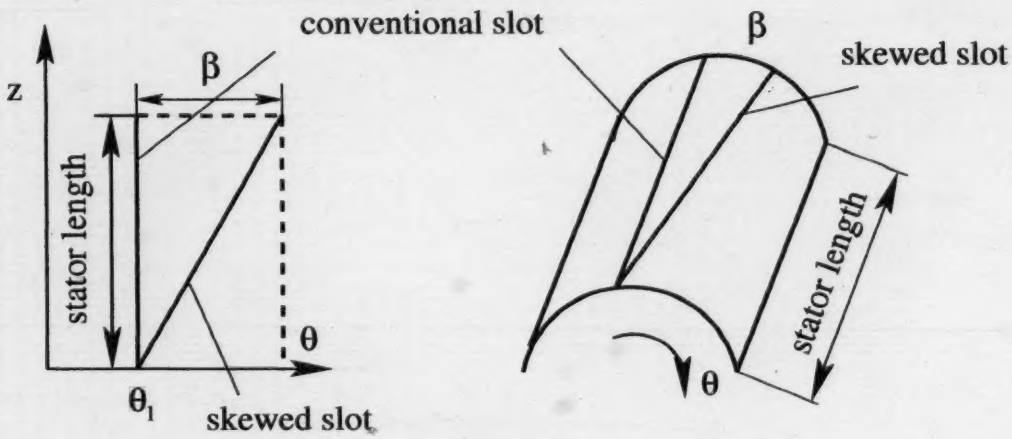

Figure 2.8: Skew.

At any z, the angular position of the conductor along the axial length may be found as

$$\theta = \theta_1 + \alpha z \tag{2.15}$$

where

$$\alpha = \frac{\beta}{l} \tag{2.16}$$

and may be referred as the *axial phase shift* of the coil; l is the stator length.

For the n-th space harmonic, the angle must be n times greater than for the fundamental [14, 17], and the harmonic axial phase shift becomes

$$\alpha_n = \frac{\beta}{l} n \tag{2.17}$$

2.4.2 Voltage in a skewed winding and the skew coefficient

The expression (2.3) can be used to evaluate a voltage harmonic in a skewed coil, if the flux density harmonic penetrating the coil is known. In a general case of a skewed magnetic field, each harmonic of the air gap magnetic flux density can be expressed as

$$B_m = \widehat{B} \cos(m\theta + \phi + \alpha z - \omega t) \tag{2.18}$$

where $\widehat{B}$ is the harmonic magnitude, m is space order, θ is angular position in mechanical radians, ϕ is phase, α is axial phase shift of the skewed field per unit length, ω is electrical angular velocity.

Considering Fig. 2.9, the flux linkage m-th harmonic can be determined from

$$\psi = N \int_S B dS \tag{2.19}$$

$$= Nr \int_0^l \int_{\lambda_1 + \frac{\beta z}{l}}^{\lambda_2 + \frac{\beta z}{l}} \widehat{B} \cos(m\theta + \phi + \alpha z - \omega t) d\theta \, dz \tag{2.20}$$

where N is number of turns in the coil, S is surface area of the coil, λ_1 and λ_2 are angular positions of the coil sides at one end of the stator, β is stator conductor skew in mechanical radians, l is effective stator length, r is radius of the stator inner circumference. It is assumed that the vector of magnetic flux density B is perpendicular to S.

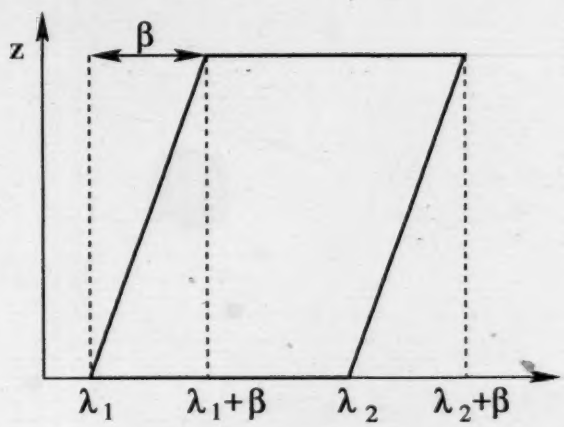

Figure 2.9: A skewed coil.

Integration of (2.20) gives

$$\psi = Nr\widehat{B} K_1 K_2 l \cos\left[\frac{m(\lambda_2 + \lambda_1)}{2} + \frac{(\frac{m\beta}{l} + \alpha)l}{2} + \phi - \omega t\right] \tag{2.21}$$

where

$$K_1 = \frac{\sin\frac{m(\lambda_2 - \lambda_1)}{2}}{\frac{m}{2}} \tag{2.22}$$

$$K_2 = \frac{\sin\frac{m\beta + \alpha l}{2}}{\frac{m\beta + \alpha l}{2}} \tag{2.23}$$

The expression can be further reduced to

$$\psi = Nr\widehat{B} K_1 K_2 l \cos(\phi_\psi - |\omega| t) \tag{2.24}$$

where

$$\phi_\psi = K_3 \left(\frac{m}{2}(\lambda_2 + \lambda_1) + \frac{\alpha l + \beta m}{2} + \phi\right) \tag{2.25}$$

$$K_3 = \text{sign}(\omega) \tag{2.26}$$

It is assumed that the angular velocity of the magnetic flux density ω can be negative, depending on the direction in which the field harmonic rotates. However, the flux linking the coil has only "positive" frequency.

The voltage harmonic in the coil can be computed as

$$v_{\text{coil}} = -\frac{\partial \psi}{\partial t} = \omega N r \widehat{B} K_1 K_2 l \cos(\phi_\psi + \tfrac{\pi}{2} - \omega t) \tag{2.27}$$

If the magnetic field is unskewed (for example, the magnetic field formed by the field mmf and the permeance due to the pole shape), $\alpha = 0$ in the expression (2.18), and (2.23) reduces to

$$K_2 = \frac{\sin \frac{m\beta}{2}}{\frac{m\beta}{2}} \tag{2.28}$$

This is a classical definition of the harmonic *skew coefficient* [14, 17]. One can see that if the machine slots are also unskewed, then $\beta = 0$, and $K_2 = K_{\text{skew,n}} = 1$.

To remove the m-th harmonic of the coil voltage, the numerator of the expression (2.28) has to be zero. If the skew is chosen to be

$$\beta = \frac{2k\pi}{m} \tag{2.29}$$

then the m-th harmonic skew coefficient becomes

$$K_2 = \frac{\sin \frac{m}{2}\frac{2k\pi}{m}}{\frac{m}{2}\frac{2k\pi}{m}} = \frac{\sin k\pi}{k\pi} = 0 \tag{2.30}$$

Taking the expression for voltage induced in a single coil, it is possible to carry out a phasor summation of all the coil voltages in a winding to obtain the total voltage induced in any arbitrary winding connection.

For a double layer, short-pitched winding with a span of y slots and a parallel paths, with a "going" coil side located at the bottom layer at a position λ_1, the "returning" coil side at the upper layer at λ_2, where

$$\lambda_2 = \lambda_1 + y\frac{2\pi}{N_s} \tag{2.31}$$

and N_s is total number of slots in the armature, a phase voltage can be found as

$$\vec{v}_{\text{phase}} = \frac{1}{a}\sum_i \vec{v}_{\text{coil},i} \tag{2.32}$$

where a is the number of parallel paths.

The line-to-line voltage can be found as

$$\vec{v}_{\text{LL}} = \vec{v}_{\text{phase 1}} - \vec{v}_{\text{phase 2}} \tag{2.33}$$

2.4.3 Damping of noise with skew

Noise can result from at least two sources: so-called magnetic noise and vibration of the rotor due to mechanical unbalance [8].

Magnetic noise is caused by pulsations of magnetic flux in the air gap. A simplified magnetic circuit is shown in Fig. 2.10. It can be seen that the number of slots over the pole may vary, providing magnetic paths with a different reluctance. In the left-hand side of the figure, the reluctance is maximum, so that the flux is minimum, and vice versa in the right-hand side [14].

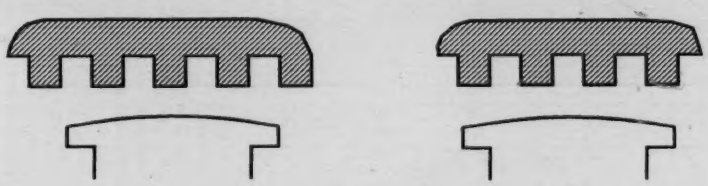

Figure 2.10: Variation of magnetic path.

The pulsating flux produces a tension force proportional to the square of the air gap flux density magnitude at the double frequency of the flux density harmonic [8, 10, 19]. For example, if the flux density vector is perpendicular to the magnetic surface, the m-th flux density harmonic

$$B = \widehat{B}\cos(m\theta + \phi + \alpha z - \omega t) \tag{2.34}$$

produces the m-th radial force density harmonic [20]

$$f_m = \frac{1}{2\mu_0}B^2 = \frac{\widehat{B}^2}{4\mu_0}(1 + \cos 2(m\theta + \phi + \alpha z - \omega t)) \tag{2.35}$$

In fractional slot machines, there may be subharmonics of the space order m lower than of the fundamental [21] which also produce noise. Measurements give a total range of the open-circuit noise frequency in the most machines from 700 to 1400 Hz [8].

A skewed slot pattern reduces vibration, because flux becomes more uniform across the air gap.

Chapter 3

Literature review

A review of literature is presented to allow investigation of existing techniques to estimate performance, factors that influence stray losses and existing models which have been used to quantify losses. The literature on skewed synchronous machines is scarce, so that research done on other types of skewed machines is also reviewed.

3.1 Machine models

Models of electrical machines including, but not limited to, synchronous machines are described in this section. The models that have been or can be developed to account for skew are reviewed in more detail.

An expanded equivalent circuit has been used to evaluate performance of an induction machine [10, 18, 22, 23, 24, 25, 26]. Neglecting magnetic saturation, each magnetic field harmonic can be treated separately, and using supersposition, added to form the resulting waveform. Thus the circuit consists of loops connected in series, a loop describing electric quantities of a certain space harmonic [22]. The parameters of such a model can be determined analytically [11, 18] or numerically [23, 24, 27]. Skew can be included in the model in the form of harmonic skew factors [23, 24, 28] or harmonic inter-bar factors [25, 26].

Well-known numerical models are the *eddy current model* and the *coupled circuit model* [29, 30, 31, 32]. The eddy current model employs simultaneous solution of the stator circuit equations, rotor circuit equations, and magnetic field equations for each region in a two-dimensional finite element model. As the rotor moves, the system of equations is time-stepped to obtain values corresponding to the movement. The coupled circuit method time-steps the stator and the rotor circuit equations, using FEA to update the circuit parameters at each time step. These two models have been futher developed to account for skew [29, 30, 32, 33]. In the eddy current model, the machine can be "sliced" axially, as shown in Fig. 3.1. In each slice, skew is zero, but the slot is shifted to approximate skew. All equations in all slices must be solved simul-

taneously to provide continuous current in the slot [29, 32, 33, 34, 35, 36, 37]. The coupled circuit model accounts for skew by skew factors incorporated into parameters of the circuit equations, or using the multi-slice approach as well [24, 30, 31, 32, 38, 39]. The majority of this work has been devoted to induction machines; however, the coupled circuit model has also been used to simulate a small skewed salient-pole synchronous generator [40]. One drawback of numerical models is high time consumption, and a compromise between computational accuracy and time is sometimes required. As an alternative to time-domain FEA, frequency domain FEA has been employed to lower time requirements. The method considers a harmonic of the field at a time. Calculations in this case require less time than simulating an instantaneous field [33, 41].

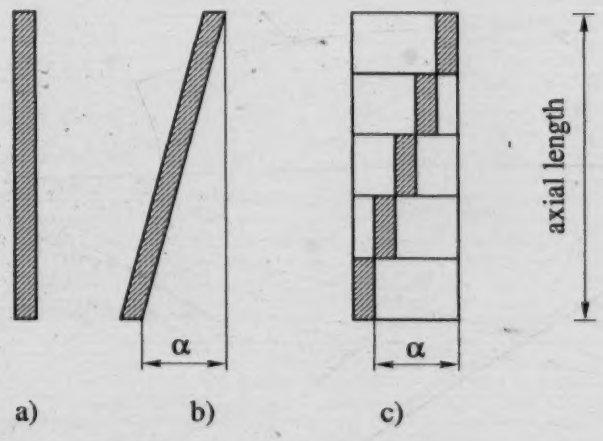

Figure 3.1: A multi-slice model of a skewed slot.

A *permeance model*, where air gap magnetic flux density is obtained as a product of air gap permeance and mmf waves, can be used to evaluate performance of a salient pole synchronous generator [10, 20, 42, 43, 44] (see Chapter 4). Permeance and mmf harmonic series can be obtained by magnetostatic FEA, keeping either the former or the latter constant to determine the other [42]. A skewed salient pole machine without a damper has been simulated neglecting saturation [43]; mmf waveforms are represented in a piecewise-linear form, and permeances computed directly from the air gap geometry. A large unskewed machine with a damper winding has been analyzed in [20], where the field mmf has been approximated by Carter's equation, and permeance waveforms obtained from a magnetostatic FE model. Given magnetic flux density in the air gap, voltages and currents induced in a damper winding can be obtained [20, 44, 45].

Magnetic circuits of a machine can be represented by *reluctance networks* [46, 47, 48, 49, 50] or *permeance networks* [51], where a characteristic part is replaced by a reluctance or permeance element, either constant or varying. Magnetic circuits of a machine can also be modeled by equivalent *cascade*

circuits [52], where the vector magnetic potential is an analogue to voltage, and the magnetic field intensity is analogous to current.

Ladder networks, or equivalent circuits to represent a squirrel-cage rotor, have been used [10] to find current and voltage distribution in bars, including *interbar current* effect (see Section 4.2.2). Ladder networks have been extensively used to model transmission lines [53].

3.2 Prediction of magnetic field

Evaluation of magnetic field is an essential component in the prediction of losses. A *B-H* curve (Fig. 3.2) shows variation of the magnetic field magnitude in steel of a machine with the increase of load; when the dependence becomes nonlinear, the steel is called *saturated*. Magnetic saturation is helpful because it reduces harmonic mmfs and harmonic magnetic fluxes in iron [54]. Currents induced in bars of the armortisseur windings of synchronous machines increase non-linearly due to saturation in open circuit [45], similarly to the shape of the *B-H* curve. The saturation makes prediction of fields more difficult.

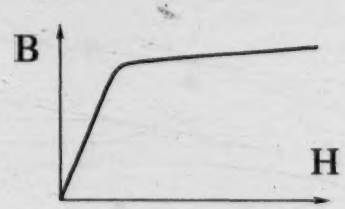

Figure 3.2: A *B-H* curve.

There are numerous analytical and numerical methods that can be applied to computation of magnetic fields in a machine. They can be modified to account for magnetic saturation and to incorporate skew.

3.2.1 Analytical methods to predict magnetic field

In early machine design, it was acceptable to estimate average values of magnetic fluxes and flux densities in distinct parts of a machine, to determine a size of the part [11, 18, 19]. Adoption of linear superposition enabled one to consider magnetic fields as a sum of fields from different sources and to view a waveform as an harmonic series. The latter made it possible to apply already developed mathematical techniques to analyze physical fields in the machine.

Generalised Ampere's and Faraday's Laws, known as Maxwell equations, can be transformed into Helmholtz equations to describe a sinusoidal magnetic field:

$$(\nabla^2 + k)A = 0 \tag{3.1}$$

where k is a constant, A is an unknown twice differentiable function. Using the equation (3.1), many results have been obtained. Magnetic field, induced

by eddy currents on and under the smooth surface of a pole, solid or laminated, due to a moving slotted surface across the air gap, has been described [19, 56]. Magnetic flux density and current density distributions in a rectangular slot that contains a current-carrying conductor can be obtained at each frequency [18]. If $k = 0$, the equation (3.1) becomes Laplace's equation, which can be used to: give a picture of magnetic flux density in iron, if the flux density in the air is known [23]; obtain the scalar magnetic potential as a harmonic series in poles and slots in a strip "pole-slot-pole..." [52]; describe the magnetic field in a model of a salient-pole machine, where the field winding is represented by a thin current sheet located at the bottom of an interpole space [52].

A *magnetic vector potential* has been introduced to avoid discontinuities in magnetic flux density and magnetic field intensity on a boundary between two media. It has been widely used in numerical methods, as described in Section 3.2.2. The magnetic vector potential has been used to analytically find distribution of the magnetic field in semi-closed slots of several configurations, filled with current-carrying conductors [52].

Conformal transformations is yet another technique that allows one to analytically describe electrostatic or magnetostatic fields in the area of interest [57] (see *Appendix A*). With this method, magnetic flux density distribution has been found in the air gap between

- a rectangular pole and a solid surface, in the cases of an isolated pole and adjacent poles [58]
- a succession of slots across solid surface (pole face), slots of infinite depth [59, 57] and of finite depth [59]

Conformal transformation method becomes more attractive with recent development of software, which allows one to quickly evaluate *elliptic* integrals and functions [60], involved in computations. Air gap permeance harmonics have been computed for a slotted surface against a smooth surface using the conformal method and by FEA [61], with results in excellent agreement. Air gap permeance between two teeth of the same size opposite each other have been computed using the conformal method and confirmed by FEA [62].

Use of the conformal mapping method is limited by well-conditioned examples; there has been no general outline for what geometries the method does not work. Some dependencies have been found in [57, 62].

A general drawback of analytical methods is the limitation of the use of regular geometries. Attempts to improve analysis include partition an area of interest in layers with distinct properties or size [18, 23], considering a partially-layered model, as was done to analyze a salient pole machine [52].

Another drawback of analytical methods is that they assume infinitely permeable iron, which can be visualised as a B-H characteristic with the slope of 90°. Characteristics of practical machines have finite slopes that decrease when the machine parts become saturated (Fig. 3.2).

Investigations to account for magnetic saturation include modifying parameters of an equivalent circuit representing a machine. For example, reactive elements in a machine equivalent circuit can be multiplied by saturation factors, calculated as single values [6, 19, 63, 64] or polynomials of air gap mmf [65]. A phasor diagram coupled with a *B-H* curve can be used to find saturation factors in a salient pole synchronous machine [11]. Saturation factors and *d*, *q* *B-H* curves can be used to evaluate reduction in air gap magnetic flux due to saturation [66]. A saturation function of armature voltage can be used in place of the factor in modeling a synchronous generator by reactances [67]. Alternatively to modeling saturated reactances, an effective air gap can be modified by a saturation factor [54].

In general, steels used to manufacture electric machines have narrow hysteresis loops, which allows one to approximate their magnetic properties by a single *B-H* curve. A single value of permeability (or its reciprocal, reluctivity) depends on a definition of permeability [68]. For example, effective reluctivity can be defined as a time average of the ratio of magnetic flux strength and magnetic flux density [33].

An iterative method has been proposed to determine permeability on the surface of poles in synchronous machines [55]. A nonlinear equation was proposed to be coupled with curves of relative permeability versus an argument that includes *H*.

It is possible to incorporate skew into analytical methods. A term that includes the axial coordinate can be added to the phase of the armature mmf waveform in a synchronous generator [43]. A skew coefficient is commonly used for the armature voltage computations [11, 6, 17, 18].

3.2.2 Numerical methods to predict magnetic field

Most common methods used to analyze an electrical machine are two-dimensional finite element analysis (FEA) and, less common, two-dimensional finite difference analysis [69, 70]. In these methods, a cross-sectional area of the machine is covered by a mesh consisting of polygons, most commonly, triangles, or *elements*, and one principal variable is used to aproximate magnetic field in each element [68, 71, 72]. The magnetic vector potential or the scalar magnetic potential (in current-free media) can be chosen as the principal variable; currents in conductors are sources of magnetic field. Maxwell equations can be developed and modified to include information about vertices, or nodes, of each element. The resulting linearized system of equations describes magnetic field over the area. To obtain a time-varying field, the system must be updated at each time step [33, 68].

Assuming a single-valued *B-H* curve, magnetic saturation may be taken into account using an iterative method such as *Newton-Raphson method* [34, 68, 70, 71]. This technique involves recalculation of Jacobian, which depends on reluctivity and its rate of change, and recalculation of reluctivity, until the residual in the linearized system is close to zero. To account for skew, which

is in the third dimension, a multi-slice model has been used, as described in Section 3.1.

Numerical methods have a capability of predicting fluxes in places where magnetic field changes direction, for example, in tooth tips and backs. A level of polarization, or extent of rotation, of magnetic flux density has been determined in tooth roots, slot backs, core back and tooth tips of a stator in an induction machine using frequency-domain finite element method [41, 73].

Three-dimensional FE methods have been proposed to compute magnetic field in steel laminations [74, 75] and in a skewed machine [76, 77, 78]. They give very accurate results, but simulations take significantly longer than for two-dimensional models, so that they are essentially impractical for analysis of large machines.

Numerical methods produce more accurate data than analytical solutions in a case of complex geometry. A drawback of two-dimensional numerical models is significant time required for computations.

3.3 Prediction of losses

Losses in electrical machines can be divided as losses in iron due to changes in magnetic flux, ohmic conductor losses, and loss due to macro current flow in iron between conducting bars. Each loss can be considered independently.

3.3.1 Iron losses due to magnetic fluxes

Iron losses due to changes in magnetic flux can be classified as *hysteresis loss*, *eddy current loss*, and *excess loss*. Hysteresis loss arises during magnetizing and re-magnetizing of the magnetic material, because energy is required to orient magnetic domains comprising the material [79]. Eddy current losses are associated with varying magnetic fluxes that induce emfs in iron. Eddy current excess loss is believed to occur due to microscopic eddy currents induced on the walls of moving domains [80].

Traditionally, hysteresis and eddy current losses have been determined using manufacturer's curves of the loss per unit volume or mass versus amplitude of flux density [18, 79]. This technique does not account for the losses due to higher-frequency magnetic fields [23]. To account for changes with frequency, manufacturers of steel provide curves of loss versus frequency [79] for approximate calculation of high-frequency losses.

If magnetic flux density in magnetic parts of the machine is known, iron losses can be evaluated directly from the flux density distribution [23, 80, 81] (see Section 5.2) or Poynting vector for eddy current loss calculation [56, 82]. Calculation of eddy current loss in steel can be directly included in FEA [82]. Constants used to compute hysteresis losses have to be obtained empirically [11, 18, 83]. A correcting factor has been derived to account for hysteresis losses due to minor loops on a boundary of the main B-H loop [84]. An eddy

current loss formula versus geometry has been derived for a permanent magnet motor [83, 85].

To account for hysteresis effects, Preisach developed a theory that allows one to track changes of magnetic flux density with varying magnetic field intensity [86, 87, 88]. In the theory, a domain consists of electrical dipoles, which can be in either "on" or "off" states, depending on value of magnetic field intensity. If a distribution function of the dipoles is determined, magnetic flux density is easily calculated. Because of statistical nature of this theory, it can be implemented in software in straightforward manner [88]. Using statistical Preisach theory coupled with FEA, hysteresis, eddy current losses [89] and excess losses [90] can be evaluated.

Eddy current losses on a smooth pole surface due to the stator slotting can be found analytically using Maxwell's equations. The magnetic flux pulsation due to slotting has been predicted to penetrate iron along lamination edges much deeper than it was accounted for by a penetration depth constant, to comprise more than 60% of the total eddy current loss in the pole [56]. A harmonic factor to account for higher order harmonics has been included in an equation of eddy current loss in a pole [55]. Damping effect of eddy currents on the magnetic flux density waveform has been included [55]. Pole face losses, obtained with this approach, have been found to be close to the results obtained by finite difference and finite element methods for solid poles [69, 70], A deeper penetration of the tooth-ripple magnetic flux into a pole has also been confirmed numerically [70].

Hysteresis, eddy current, and excess losses due to *rotational flux* in parts of a magnetic circuit where flux changes direction, have been found to comprise about 50% of iron losses in an induction motor [73]. A dependence of these losses on flux density, given in [91], has been used to estimate the losses in stators of induction motors using finite element methods [92]. A linear dependence of the rotational hysteresis loss on hysteresis loss due to alternating fluxes has been obtained empirically [93].

As synchronous machines are often manufactured with stator fractional slot windings, mmf harmonics, with orders lower than that of the fundamental harmonic, might exist in these windings [10, 21]. The author of [21] points that these *subsynchronous* harmonics induce additional rotor loss, particularly in damper windings, which is appreciable compared with the loss caused by higher-order harmonics.

3.3.2 Currents in conductors and ohmic losses

When an electric current flows in a conductor, electrical energy is converted into heat at a rate proportional to the current squared. Electrical resistance can be evaluated depending on the current frequency [18], the conductor shape [18, 94], stranding and transposition of conductors [18]. If voltages and resistances in a circuit are known, one can find currents and losses associated with them.

Distribution of currents in the armortisseur winding of a synchronous machine has been evaluated using combined analytical and numerical approach [20, 44, 95, 96]. If damper bars of the whole machine are connected and the currents flow in loops, then the obtained circuit can be analyzed using mesh analysis. Assuming linear superposition, damper bar currents can be represented as a harmonic series, and a system of equations can be solved for a current component at each frequency.

3.3.3 Iron loss due to interbar currents

If the machine is skewed and contains a winding with non-insulated bars, then there are losses in iron due to currents flowing among the bars. Investigations have shown that losses due to these *transverse*, or *interbar*, currents could constitute about 30% of stray-load losses in an induction motor [26]. A good guide on references addressing evaluation of interbar currents has been given [53]; some of these references and others are reviewed below.

Assuming a bar-to-bar path, starting from works by Rossmaier [10, 53], Odok [10] found analytical expressions for the bar and interbar currents. The expressions have been found for a "slice" of a bar. He showed theoretically that for zero skew, interbar currents are zero, and also that the bar-to-iron impedance is purely resistive. This analysis has been used to obtain interbar losses analytically in an induction machine, assuming a stator integral slot winding [10, 22, 97]. Similar work has been done in [19, 98]. A theoretical curve of the interbar loss in an induction machine versus the cross-path (contact) resistance has a maximum [10], which has been confirmed by simulations of full-load efficiency versus contact resistance in an induction machine [25, 26].

On the basis of the work by Odok, Subba Rao and Butler [97] improved a chain equivalent circuit of an induction squirrel-cage machine, introducing an equivalent rotor bar impedance that included the effect of interbar currents, and effective skew factor. These results have been further developed. They have been combined with the general harmonic analysis model [25, 26], where a new harmonic interbar factor has been introduced. They have been used to account for interbar effects with bars partitioned by a large number of slices [28].

The results obtained in [10, 22] have also been used in a finite element model of a machine to include interbar current effect [36, 99].

It was recently suggested that interbar currents go in all directions in iron rather than between adjacent bars, and the cross-sectional model evolved as shown in Fig. 3.3 [53, 100].

The difficulty of estimating interbar resistance, especially as it can vary along the length of the bar, has been discussed by a number of authors, starting by [22]. Schemes to measure the resistance have been developed in [10, 101].

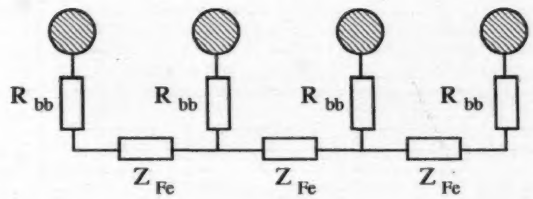

Figure 3.3: A cross-sectional interbar current model.

3.4 Summary

The work in this thesis applies methods described in this chapter to the analysis of large synchronous machines. The permeance model is used to predict the air gap flux density. Skew is incorporated into the analytical model by adding an axial phase shift to the phase angle of the permeance, mmf and magnetic field waveforms. Losses due to each harmonic are predicted using the formulae given in [80]. Ohmic losses in the armortisseur winding due to each slotting harmonic are calculated as a product of the current magnitude squared and the resistance at the frequency of interest. Finally, the inter-bar model is used to evaluate inter-bar currents and losses associated with them.

Chapter 4

Prediction of air gap magnetic fields

A *permeance model* can be used to compute magnetic flux density distribution in the air gap. In this model, the air gap flux density is a product of air gap permeance and air gap mmf waves:

$$B = PF, \tag{4.1}$$

where P is air gap permeance per unit area, F is air gap mmf. Each term can be represented by a Fourier series of the form

$$f(x) = f_{dc} + \sum_n \hat{f}_n \cos(m_n\theta + \theta_{n,0} + \alpha_n z - \omega_n t) \tag{4.2}$$

where f_{dc} is an average (dc) component, m_n is space order, $\hat{f}_n$ is amplitude of the n-th harmonic, θ is angular position from a reference point, $\theta_{n,0}$ is initial phase angle of the n-th harmonic, α_n is phase axial shift of the n-th harmonic due to skew, z is the axial coordinate, ω_n is angular velocity of the n-th harmonic.

In this chapter, the air gap permeance, the air gap mmf and the air gap flux density waveforms are obtained. The air gap permeance consists of three components: the permeance due to the non-uniform air gap (or the permeance due to the pole shape), the permeance due to the damper slotting, and the permeance due to the stator slotting. The air gap mmf consists of the field mmf, armature mmf and the armortisseur mmf. The field mmf is scaled to account for magnetic saturation of steel. The damper (or armortisseur) mmf component is formed by the damper bar currents. As the air gap magnetic field is skewed, inter-bar currents also exist and flow in iron of the pole; the *inter-bar model* is used to account for these currents to accurately predict the armortisseur mmf. The air gap magnetic flux density is evaluated using the permeance model.

4.1 Calculation of air gap permeance

The air gap permeance waveform is influenced by several factors: the shape of the pole, stator slotting, and damper slotting. The pole and the damper permeance harmonics have constant magnitudes, distributed in space and rotating with the rotor. The stator slotting harmonics are stationary, and their magnitudes vary with time, due to variation of the air gap length in the salient-pole machine. It is convenient to model the impact of each component separately and then to consider their combined effect.

The air gap permeance due to the pole shape can be modeled analytically. The effect of slotting can be modeled using data from linear magnetostatic FEA [20, 44]:

1. air gap flux density distribution over the damper slot pitch, located in the centre of the pole, with a smooth stator and a slotted pole,

2. air gap flux density distribution over the stator slot pitch, located in the centre of the pole, with a slotted stator and a smooth pole.

4.1.1 Air gap permeance due to the pole shape

The field mmf can be represented by a rectangular waveform, constant over the pole pitch (see Section 4.2). In this case, the permeance waveform over the pole pitch is identical to the flux density waveform up to a factor, by the equation (4.1). The normalised permeance curve is identical to the normalised flux density curve over the pole pitch.

Carter's expression of the normalised air gap flux density (see *Appendix A*) is exact for a rectangular pole and interpole space between two rectangular poles. One can suggest that that the expression can be valid for curved poles, if the pole curvature is taken into account. Thus an expression for the air gap permeance has been formed as a product of two functions (Fig. 4.1):

1. Normalised air gap permeance, inverse of the air gap length between the smooth pole and the smooth stator and unity over the pole edge and the interpole space.

2. Carter's normalised flux density curve, unity under the pole, diminishing to zero in the middle of the interpole space.

The following assumptions are used:

- the stator and the pole surfaces are smooth

- magnetomotive force (mmf) is a unity square wave, positive at one pole pitch and negative at adjacent ones. This assumption means that the normalised air gap flux density and permeance curves over the pole pitch are identical.

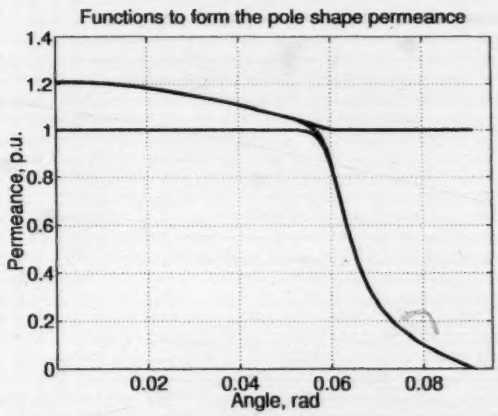

Figure 4.1: Functions to approximate the pole shape permeance.

- flux lines are perpendicular to the pole and the stator surfaces, and can be approximated by arcs between these two surfaces
- end effects in the third dimension are ignored, so that the model is two-dimensional

Magnetic flux density in the interpole space. Carter's model described in *Appendix A* has been used to calculate air gap flux density distribution in the space between adjacent poles. The equations (A.34), (A.35), (A.37), and (A.38) are duplicated here for the reader's convenience:

$$x = \frac{g}{\pi} \ln \left[e^{-X} + \frac{a-b}{2} + \sqrt{(e^{-X}+a)(e^{-X}-b)} \right] - \frac{c}{\pi} \arcsin \left(\frac{2ab}{a+b} e^{X} - \frac{a-b}{a+b} \right) \quad (4.3)$$

where x is the position along the stator bore, g is air gap length between the pole and the stator,

$$B = B_0 \left(\frac{e^{-X}-b}{e^{-X}+a} \right)^{\frac{1}{2}} \quad (4.4)$$

B is air gap magnetic flux density, B_0 is magnetic flux density in the centre of the pole,

$$a = \frac{2c^2}{c^2+g^2} e^{-\frac{\pi}{2}\frac{c}{g}} \quad (4.5)$$

$$b = \frac{2g^2}{c^2+g^2} e^{-\frac{\pi}{2}\frac{c}{g}} \quad (4.6)$$

c is the half a distance between the poles. If the ratio $R = \frac{B}{B_0}$ is the input, X

can be found from (4.4), and the equation (4.3) can be re-written as [20]

$$x = \frac{g}{\pi} \ln \left[\left(\frac{b + R^2 a}{1 - R^2} \right) + \frac{a - b}{2} + \sqrt{\left(\frac{b + R^2 a}{1 - R^2} + a \right) \left(\frac{b + R^2 a}{1 - R^2} - b \right)} \right] - \frac{c}{\pi} \arcsin \left[\left(\frac{2ab}{a + b} \right) \left(\frac{b + R^2 a}{1 - R^2} \right) - \frac{a - b}{a + b} \right] \quad (4.7)$$

Given the value of R, of the normalised magnetic flux density in the interpole space, the point x where this value of R occurs can be calculated from the equation (4.7).

Round pole. Two non-concentric surfaces, one of the stator and the other of the pole, are shown in Fig. 4.2. Suppose that the origin of xy coordinates is located in the centre of a circle with the radius of the pole tip. The radius of the stator inner circumference is located at the distance a below the origin. It is desirable to find length of an arc between the stator and the rotor at an arbitrary angle α, because permeance due to the pole shape is inversely proportional to the arc length.

It can be seen that the arc has a centre in the point Φ. If the radius r and the angle γ of the arc can be determined, then the arc length can be calculated as

$$l_{arc} = 2\gamma r \quad (4.8)$$

The coordinates x, y of the point Φ can be found as

$$x = R_p \sin\alpha - r\cos\alpha \quad (4.9)$$

$$y = R_p \cos\alpha + r\sin\alpha \quad (4.10)$$

or

$$x = R_s \sin\beta - r\cos\beta \quad (4.11)$$

$$y = R_s \cos\beta - a + r\sin\beta \quad (4.12)$$

where R_p is the pole tip radius, R_s is the stator bore raduis, and β is the angle from the point $(0, a)$ corresponding to the point B. As x, y are coordinates of the same point, the following system of equations can be obtained:

$$R_p \sin\alpha - r\cos\alpha = R_s \sin\beta - r\cos\beta \quad (4.13)$$

$$R_p \cos\alpha + r\sin\alpha = R_s \cos\beta - a + r\sin\beta \quad (4.14)$$

Assumming that β is small, so that $\cos\beta \approx 1$ and $\sin\beta \approx \beta$, and solving for r, one can obtain a quadratic equation

$$r^2(1 - \cos\alpha) - r(R_s - R_p)\sin\alpha + R_s(R_s - a - R_p\cos\alpha) = 0 \quad (4.15)$$

Even for a maximum α corresponding to the pole tip end, $(1 - \cos\alpha)$ is by an order smaller than $\sin\alpha$. Therefore, the first term is much smaller than the second term and can be neglected. Then one can obtain

$$r = \frac{R_s(R_s - a - R_p\cos\alpha)}{(R_s - R_p)\sin\alpha} \quad (4.16)$$

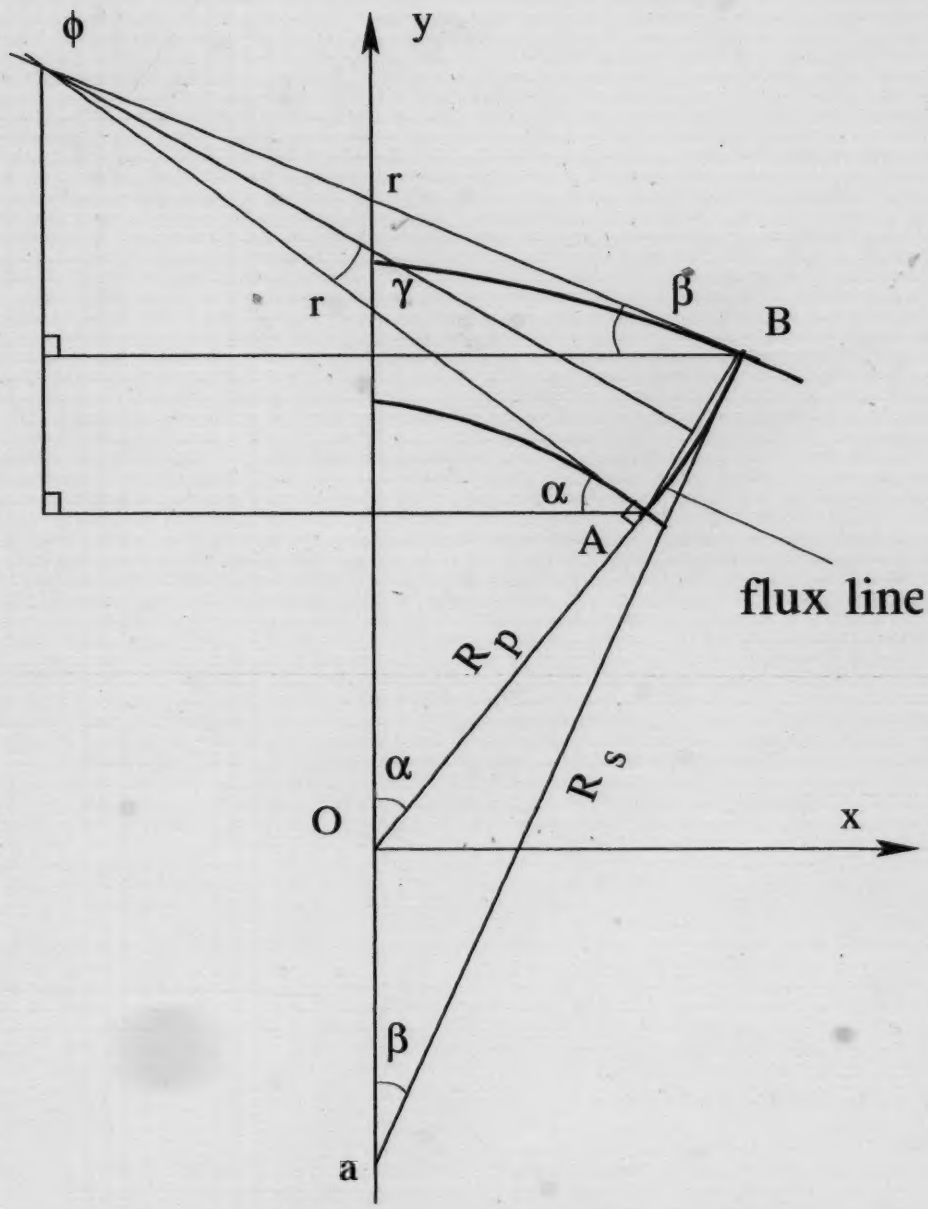

Figure 4.2: Geometry of the pole and the stator.

The length of the segment AB is given by

$$d = \sqrt{(x_A - x_B)^2 - (y_A - y_B)^2} \tag{4.17}$$

and

$$\sin\gamma = \frac{d}{2r} \tag{4.18}$$

The distance between the centres of the pole tip and stator bore circumferences

$$a = R_s - R_p - g_{\min} \tag{4.19}$$

where $g_{\min}$ is the length of the air gap in the centre of the pole.

The air gap permeance due to the pole shape. The normalised air gap permeance due to the pole shape is product of two functions, shown in Fig. 4.1. It can be expanded to Fourier series

$$\bar{P}_{\text{pole}} = \bar{P}_{\text{pole},0} + \sum_{n=1}^{\infty} \bar{P}_n \cos(n\theta + \phi_n - \omega_n t) \tag{4.20}$$

The maximum air gap permeance, in the centre of the pole, is

$$P_{\max} = \frac{\mu_0}{g_{\min}}, \tag{4.21}$$

The air gap permeance due to the pole shape can be obtained by multiplying the normalised curve by the maximum air gap permeance.

A waveform of the air gap per unit flux density is obtained by the manufacturer by means of FEA (Fig. 4.3, right). One can see that it has a similar shape to the normalized permeance curve due to the pole shape calculated analytically. The "dips" under the pole are due to damper slotting.

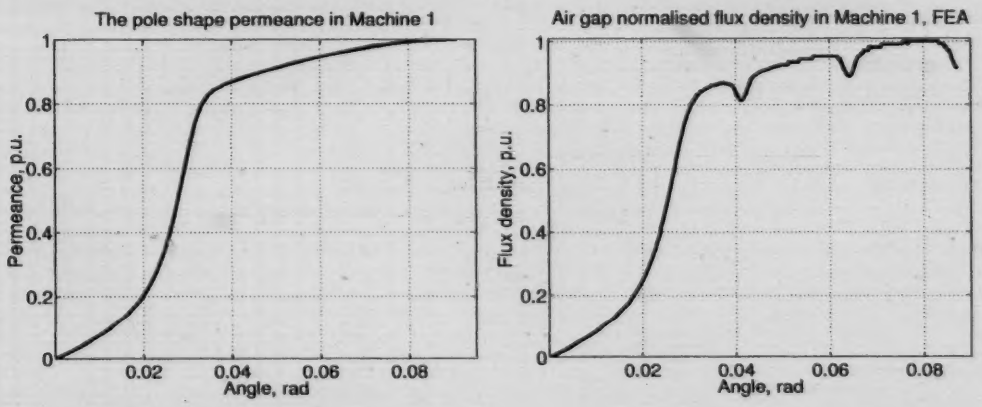
The pole shape permeance in Machine 1
Permeance, p.u.
Angle, rad
Air gap normalised flux density in Machine 1, FEA
Flux density, p.u.
Angle, rad

Figure 4.3: Normalised permeance due to the pole shape, calculated from the model (left) and by FEA (right), on the half a pole pitch.

4.1.2 Air gap permeance due to the damper slotting

FEA analysis provides distribution of air gap flux density over one damper slot in the centre of the pole. If the mmf is constant over the pole pitch, the normalised flux density curve is identical to the normalised permeance curve. The permeance Fourier coefficients due to the damper slotting can be calculated from the magnetic flux density harmonic series of the form

$$f(t) = a_0 + \sum_{n=1}^{\infty} (a_n \cos(n\omega_0 t + \theta_n) + b_n \sin(n\omega_0 t + \theta_n)) \tag{4.22}$$

as

$$a_0 = \frac{1}{T_0} \int_{T_0} f(t)\, dt \tag{4.23}$$

$$a_n = \frac{2}{T_0} \int_{T_0} f(t) \cos(n\omega_0 t)\, dt \tag{4.24}$$

$$b_n = \frac{2}{T_0} \int_{T_0} f(t) \sin(n\omega_0 t)\, dt \tag{4.25}$$

where T is the period of $f(t)$.

However, damper slots are located irregularly on the pole pitch. To obtain the air gap permeance due to damper slotting accurately, the Fourier series should be determined separately at each slot, respectively to the common reference angle. Then sum of the Fouries series over all slots comprises the permeance due to damper slotting on the pole pitch. This algorithm is described below [102].

Assume that the input magnetic flux density over one slot pitch provided by FEA is given by

$$B(\alpha) = B_0 + \sum_n B_n \cos(n\alpha + \phi_n) \tag{4.26}$$

where α is the angle varying over the slot pitch, B_0 and B_n are the average and the n-th harmonic magnitude of flux density, respectively, ϕ_n is the n-th harmonic phase angle. Assume also that the harmonic series (4.26) describes a combination of the unslotted case and the effect of slotting:

$$B(\alpha) = B_{\text{base}} + B_{\text{slot}} \tag{4.27}$$

where B_{base} is the peak value of the air gap flux density in the unslotted case (smooth stator and rotor), in the centre of the pole. The air gap length can be assumed constant over the damper slot in the centre of the pole. Therefore, flux density takes the peak value over the damper slot.

The flux density component due to damper slotting is then given by

$$B_{\text{slot}} = B(\alpha) - B_{\text{base}} = B_0 - B_{\text{base}} + \sum_n B_n \cos(n\alpha + \phi_n) \tag{4.28}$$

The average component is less than the peak value of the unslotted case. That means that average permeance is reduced, when compared with unslotted permeance, due to the effect of slotting.

To obtain the normalised flux density waveform, the expression (4.28) should be scaled by the peak flux density of the unslotted case:

$$\bar{B}_{\text{slot}} = \frac{B_0}{B_{\text{base}}} - 1 + \sum_n \frac{B_n}{B_{\text{base}}} \cos(n\alpha + \phi_n) = \bar{B}_0 - 1 + \sum_n \bar{B}_n \cos(n\alpha + \phi_n) \quad (4.29)$$

where

$$\bar{B}_0 = \frac{B_0}{B_{\text{base}}}, \quad \bar{B}_n = \frac{B_n}{B_{\text{base}}} \quad (4.30)$$

Assume that the centre of the slot is located at the electrical angle β_s from the origin. Assume that α varies from $-\pi$ to π over the slot pitch of λ_s electrical radians (Fig. 4.4). To transfer this coordinate system to a general coordinate system of an electrical angle θ_e, suppose that the centre of the slot is located at the angle β_s with respect to the origin at d-axis of the pole. Then

$$\alpha = \left(\theta_e - \beta_s\right) \frac{2\pi}{\lambda_s} \quad (4.31)$$

To verify this formula, one can pick θ_e at the edges of the slot to check whether

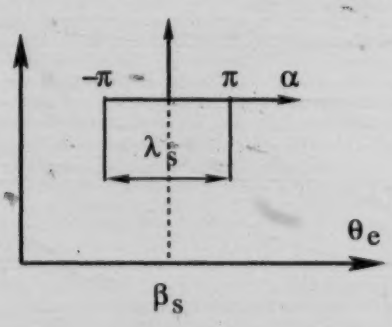

Figure 4.4: A mapping from α to θ_e.

$\alpha = \pm\pi$.

Average permeance due to damper slotting. The average permeance due to slotting is given by the equation (4.23) with the period 2π (Fig. 4.4)

$$\bar{P}_{d,0} = \frac{1}{2\pi} \int_{-\pi}^{\pi} B(\theta_e)\, d\theta_e \quad (4.32)$$

This permeance is negative over slots and zero otherwise, therefore, the integral from $-\pi$ to π can be replaced by a sum of integrals over n_s damper slots:

$$\bar{P}_{d,0} = \frac{1}{2\pi} \sum_{s=1}^{n_s} \int_{\beta_s - \frac{\lambda_s}{2}}^{\beta_s + \frac{\lambda_s}{2}} B(\theta_e)\, d\theta_e \quad (4.33)$$

or

$$\bar{P}_{d,0} = \frac{1}{2\pi} \sum_{s=1}^{n_s} \int_{\beta_s - \frac{\lambda_s}{2}}^{\beta_s + \frac{\lambda_s}{2}} \left(\bar{B}_0 - 1 + \sum_n \bar{B}_n \cos\left(n(\theta_e - \beta_s) \frac{2\pi}{\lambda_s} + \phi_n \right) \right) d\theta_e \tag{4.34}$$

where s is the number of the slot. Further solving the integral gives

$$\bar{P}_{d,0} = \frac{n_s \lambda_s (\bar{B}_0 - 1)}{2\pi} + \sum_{s=1}^{n_s} \sum_n \bar{B}_n \int_{\beta_s - \frac{\lambda_s}{2}}^{\beta_s + \frac{\lambda_s}{2}} \cos\left(n(\theta_e - \beta_s) \frac{2\pi}{\lambda_s} + \phi_n \right) d\theta_e \tag{4.35}$$

It can be shown that the second term equals zero. Now, to express the average permeance versus mechanical angle, recall that

$$\lambda_s = 2p\lambda_{\text{slot}} \tag{4.36}$$

where p is the number of pole pairs, λ_{slot} is the slot pitch in mechanical radians. The average component of the normalised permeance due to damper slotting becomes

$$\bar{P}_{d,0} = \frac{n_s p \ \lambda_{\text{slot}} (\bar{B}_0 - 1)}{\pi} \tag{4.37}$$

Harmonic permeance due to damper slotting. The Fourier coefficient for the k-th harmonic of the permeance can be found from the equation (4.24), assuming that the permeance is nonzero only over the slots. The equation becomes

$$\bar{P}_k \triangleq \frac{1}{2\pi} \sum_{s=1}^{n_s} \int_{\beta_s - \frac{\lambda_s}{2}}^{\beta_s + \frac{\lambda_s}{2}} \left(\bar{B}_0 - 1 + \sum_n \bar{B}_n \cos\left(n(\theta_e - \beta_s) \frac{2\pi}{\lambda_s} + \phi_n \right) \right) \cos(k\theta_e) d\theta_e \tag{4.38}$$

Solving the integral yields

$$\begin{aligned} \bar{P}_k = \frac{2}{\pi} \frac{(\bar{B}_0 - 1)}{k} \sin\frac{k\lambda_s}{2} \sum_{s=1}^{n_s} \cos(k\beta_s) \\ + \frac{1}{\pi} \sum_{s=1}^{n_s} \sum_n \bar{B}_n \left[\frac{1}{\frac{2n\pi}{\lambda_s} + k} \cos(k\beta_s + \phi_n) \sin\left(n\pi + \frac{\lambda_s k}{2} \right) \right. \\ \left. + \frac{1}{\frac{2n\pi}{\lambda_s} - k} \cos(-k\beta_s + \phi_n) \sin\left(n\pi - \frac{\lambda_s k}{2} \right) \right] \end{aligned} \tag{4.39}$$

The electric angles λ_s and β_s should be expressed in mechanical radians. Shifting the origin to q-axis, we obtain

$$\beta_s = \left(\beta_{\text{slot}} + \frac{\pi}{2p} \right) 2p = 2p\beta_{\text{slot}} + \pi \tag{4.40}$$

The expression for the k-th harmonic of the air gap permeance due to damper slotting becomes

$$\bar{P}_k = \frac{2(\bar{B}_0 - 1)}{k\pi} \sin(kp\lambda_{\text{slot}}) \sum_{s=1}^{n_s} \cos(2kp\beta_{\text{slot}} + k\pi)$$
$$+ \frac{1}{\pi} \sum_{s=1}^{n_s} \sum_{n} \bar{B}_n \left[\frac{p\lambda_{\text{slot}}}{n\pi + kp\lambda_{\text{slot}}} \cos(\phi_n + 2kp\beta_{\text{slot}} + k\pi) \sin(n\pi + kp\lambda_{\text{slot}}) \right.$$
$$\left. + \frac{p\lambda_{\text{slot}}}{n\pi - kp\lambda_{\text{slot}}} \cos(\phi_n - 2kp\beta_{\text{slot}} - k\pi) \sin(n\pi - kp\lambda_{\text{slot}}) \right] \quad (4.41)$$

The normalised total air gap permeance due to damper slotting takes form

$$\bar{P}_{\text{d}} = \bar{P}_{d,0} + \sum_{k} \bar{P}_k \cos(2p\, k\, \theta_{mq} + k\pi) \quad (4.42)$$

where

$$\theta_e = \left(\theta_m + \frac{\pi}{2p}\right) 2p = 2p\, \theta_m + \pi \quad (4.43)$$

with respect to the q-axis, θ_m is a mechanical angle.

4.1.3 Air gap permeance due to the pole shape and the damper slotting

The combined normalised permeance due to the pole shape and damper slotting is given by

$$\bar{P}_{\text{pd}} = \bar{P}_{pole,0} + \bar{P}_{d,0} + \sum_{n} \bar{P}_n \cos(n\theta + \phi_n - \omega_n t) + \sum_{k} \bar{P}_k \cos(k\theta + \phi_k - \omega_k t) \quad (4.44)$$

To obtain a physical value of the permeance, the normalised curve should be multiplied by the air gap permeance in the centre of the pole

$$P_{\max} = \frac{\mu_0}{g_{\min}} \quad (4.45)$$

The combined air gap permeance due to the pole shape and damper slotting becomes

$$P_{\text{pd}} = P_0 + \sum_{n} P_n \cos(n\theta + \phi_n - \omega_n t) + \sum_{k} P_k \cos(k\theta + \phi_k - \omega_k t) \quad (4.46)$$

where

$$P_0 = P_{pole,0} + P_{d,0} = (\bar{P}_{pole,0} + \bar{P}_{d,0}) P_{\max} \quad (4.47)$$

A waveform of the air gap permeance with the effect of damper slotting has been computed for Machine 1, shown in Fig. 4.5 (left). The air gap flux density waveform obtained by FEA and shown in Fig. 4.3 (right) has been reproduced in Fig. 4.5 (right). One can see that two waveforms obtained by the two methods have similar shapes.

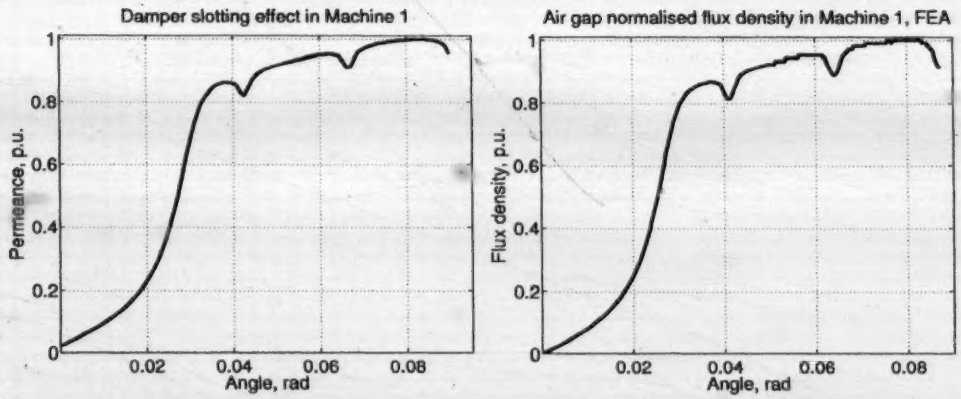
Damper slotting effect in Machine 1
Permeance, p.u.
Angle, rad
Air gap normalised flux density in Machine 1, FEA
Flux density, p.u.
Angle, rad

Figure 4.5: Permeance due to the pole shape and damper slotting, calculated from the model (left), and the normalised permeance obtained by FEA (right), on the half a pole pitch.

4.1.4 Air gap permeance due to the stator slotting

If the stator is slotted, the permeance is less under the slots, as shown in Fig. 4.6.

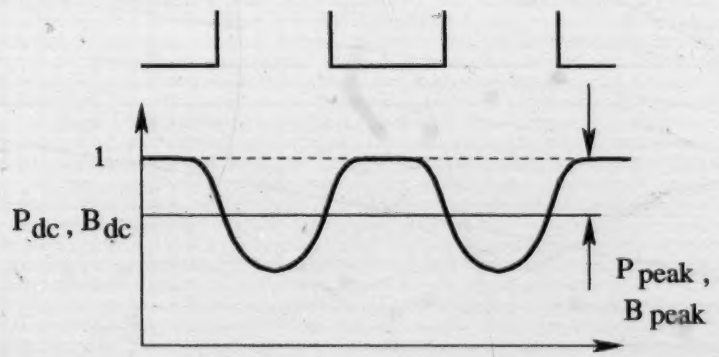

Figure 4.6: The normalized permeance due to stator slotting.

FEA analysis provides distribution of the air gap flux density over one stator slot pitch in the centre of the pole. Due to uniform distribution of the stator slots over the circumference of the air gap, the flux density distribution over the circumference can be assumed to be periodic with the period of the stator slot pitch. The space order of the stator slot flux density harmonic in the machine is calculated as

$$s = pnN_s \tag{4.48}$$

where p is the number of pole pairs, n is space order of the harmonic over the stator slot pitch, N_s is the number of stator slots.

The flux density curve can be normalised to be unity under the slots, as shown in Fig. 4.6. In this case, the base value to normalise the curve should

be chosen as

$$B_{\text{base}} = B_{\text{dc}} + B_{\text{peak}} \tag{4.49}$$

The normalised permeance due to the stator slotting is identical to the normalised flux density waveform and can be expanded to

$$\bar{P}_{\text{stat}} = 1 + \sum_s \bar{P}_s \cos(s\theta + \phi_j + \alpha z - \omega_s t) \tag{4.50}$$

4.1.5 Air gap permeance due to the pole shape, damper slotting, and stator slotting

If the stator is smooth, the permeance due to the stator slotting is unity and the total air gap permeance waveform is one that is due to the pole shape and damper slotting. In case of the slotted stator, the "dips" under the stator slots are present in the combined waveform. One can suggest that a product of two permeances, one due to the stator slotting and other due to the pole shape and damper slotting, gives the total air gap permeance. The combined air gap permeance is thus calculated as

$$P_{\text{air gap}} = P_{\text{pd}} \times \bar{P}_{\text{stat}} \tag{4.51}$$

or

$$\begin{aligned} P_{\text{air gap}} &= P_0 + \sum_n P_n \cos(n\theta + \phi_n - \omega_n t) \\ &+ \sum_k P_k \cos(k\theta + \phi_k - \omega_k t) + P_0 \sum_s \bar{P}_s \cos(s\theta + \phi_s + \alpha z - \omega_s t) \\ &+ \left[\sum_n P_n \cos(n\theta + \phi_n - \omega_n t)\right] \times \left[\sum_s \bar{P}_s \cos(s\theta + \phi_s + \alpha z - \omega_s t)\right] \\ &+ \left[\sum_k P_k \cos(k\theta + \phi_k - \omega_k t)\right] \times \left[\sum_s \bar{P}_s \cos(s\theta + \phi_s + \alpha z - \omega_s t)\right] \end{aligned} \tag{4.52}$$

4.2 Calculation of air gap MMF

The air gap mmf may be considered as sum of mmfs produced by different sources: by the field, or excitation, winding, by the armature winding and by the amortisseur, or damper, winding.

The field mmf can be calculated as in Section 4.2.1; armature mmf harmonic series can be user specified. However, the damper mmf is unknown because damper currents depend on air gap flux density, which is unknown. After the air gap permeance waveform is computed, air gap flux density can be calculated by the equation (4.1), using sum of the field and armature mmfs. The resulting flux density distribution allows one to evaluate damper currents and damper mmf. Assuming that the damper mmf does not affect the field and armature mmfs, the calculation of flux density may be updated [20].

4.2.1 Field mmf

The field mmf is produced by the field winding located on the poles of the synchronous machine, as shown in Fig. 4.7. The figure shows two poles, the stator across the air gap and several paths of magnetic flux in the circuit. Neglecting mmf drops in the iron and leakage fluxes, the mmf can be assumed to have a square waveform, constant over one pole pitch.

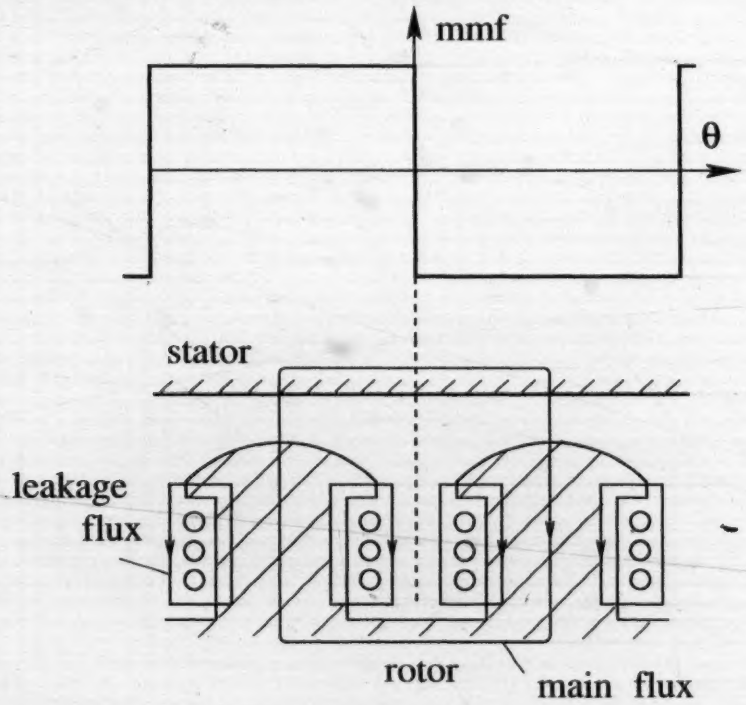

Figure 4.7:

Given the Ampere's Law

$$\oint \mathbf{H}\, d\mathbf{l} = N\mathbf{I} \tag{4.53}$$

where **I** is the field current in one turn, N is the number of turns, and assuming infinite permeability of iron and constant air gap length g, the mmf drop from the pole to the stator in the air gap can be approximately calculated as

$$Hg = \frac{NI}{2} \tag{4.54}$$

where I is amplitude of the field current. Thus the magnitude of the field mmf waveform, shown in Fig. 4.7, is approximately a half a product of the rated field current and the number of turns. However, this estimate is valid only for unsaturated magnetic circuits, such as in the short circuit regime.

In unsaturated magnetic circuits, the air gap flux density linearly depends on the field mmf, as shown by an airgap characteristic in Fig. 4.8. In saturated regimes (for example, in open circuit), the dependence becomes nonlinear. However, the permeance analytical model assumes a linear dependence, as given by the equation (4.1). The mmf value can be reduced in such a way that the value of the air gap flux density on the airgap characteristic equals the value of the saturated curve at the rated current.

Scaling of the field mmf magnitude can be done using FEA. One way to account for saturation is to obtain a linear and a nonlinear BH characteristics of an unskewed machine, assuming non-saturating and saturating steel, respectively (Fig. 4.8). Suppose that F_1 is the rated value of the field current. A difference between values B_1 and B_2 of flux density suggests that the field current must be reduced to correspond to the value B_2 on the air gap curve [103].

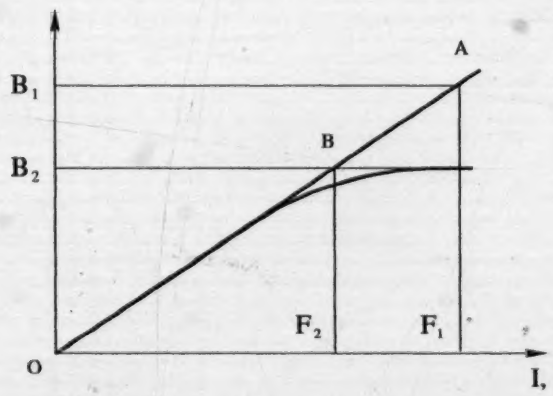

Figure 4.8: BH linear and nonlinear characteristics.

Another way to account for saturation is to exploit only a nonlinear BH curve and the equation (4.1). The mmf magnitude can be calculated as

$$F = \frac{B_{\max}}{P_{\max}} \tag{4.55}$$

where $B_{\max}$ is the peak flux density obtained in the saturated regime, and $P_{\max}$ is given by Equation (4.21).

4.2.2 Armortisseur currents and mmf

The armortisseur mmf is produced by currents induced in short-circuited bars of the armortisseur (damper) winding, located on the pole surface. In a skewed magnetic field, *inter-bar* currents flow in the pole iron. The inter-bar current effect can be incorporated into an existing model of the damper bar current calculation [44]. It is shown that the damper currents calculated in a three-dimensional circuit form an mmf varying in three dimensions.

Currents induced in bars of the armortisseur winding are caused by

- pulsations of the air gap flux due to periodic movement of the stator slots relative to the rotor surface;
- higher-order space harmonics of the rotating armature mmf, formed by currents of the three-phase stator winding. While the armature mmf fundamental harmonic moves with the same speed as the rotor, the higher-order space harmonics rotate forward or backward with respect to the rotor.

Constructing the interbar current model

The phenomenon of *interbar*, or *transverse*, currents has been well explained in [53] and described below. Suppose that two adjacent bars in a skewed machine are partitioned in layers, AC and CE and BD and DF respectively, as shown in Fig. 4.9. The emfs induced in the layers of a bar have different phase shifts due to skewing (see Section 2.4). As a result, emfs in the loop $CABD$ and $ECDF$ do not cancel each other, and a current in branch CD is non-zero.

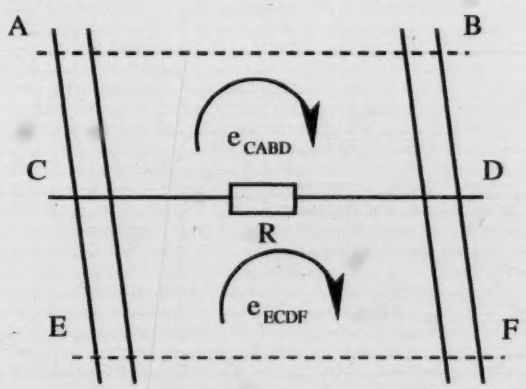

Figure 4.9: Voltages in skewed bars.

Fig. 4.10a shows the most recent way to model the inter-bar current effect [53]. The impedance between two bars consists of the contact resistance R_c on the surface of each bar and the impedance of iron. The iron impedance is much smaller than the contact resistance, so that it can be neglected. The circuit simplifies to one shown in Fig. 4.10b.

In the longutudinal direction, the armortisseur bars can be partitioned in slices. The resulting circuit configuration becomes three-dimensional (Fig. 4.11). In the figure, n is the number of slices, R_{bb} is the contact resistance, z_{bar}, z_{end}, z_{p2p} are the impedances of the bar, the end ring segment between two bars, and of the pole-to-pole connection, respectively. The circuit includes the damper bars on all poles. If the poles are not connected, the connection is assumed to be present with a large value of impedance. To simplify the model, it is assumed that there are no interbar currents between adjacent poles.

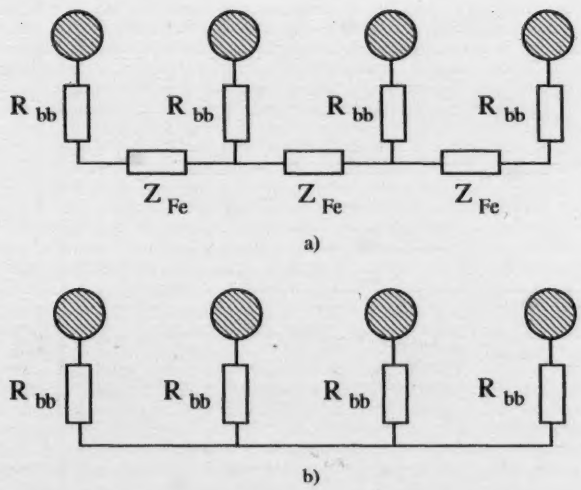

Figure 4.10: Cross-sectional interbar current model.

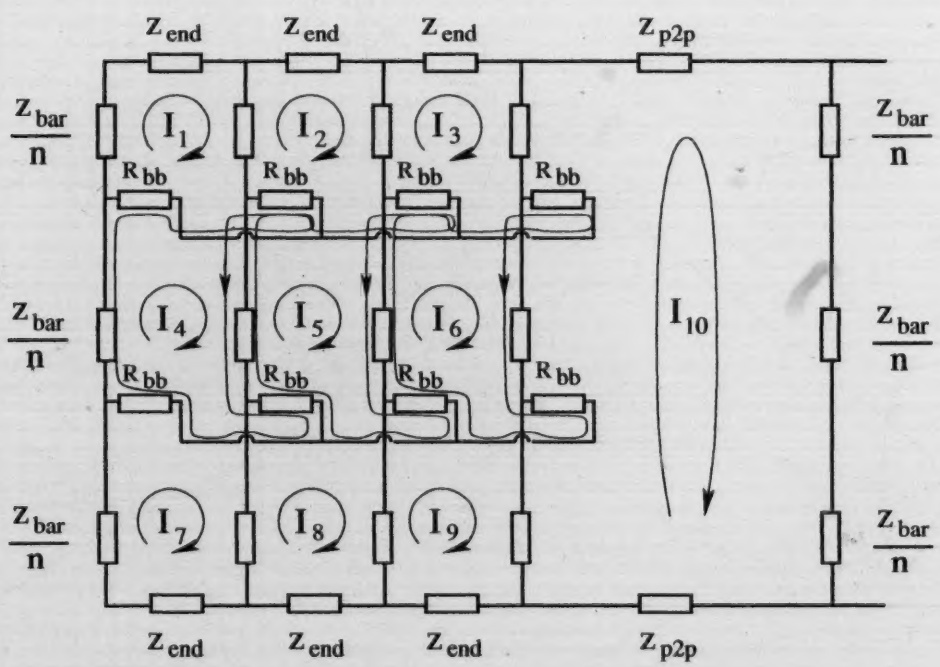

Figure 4.11: A model of the damper winding including interbar currents.

The armortisseur circuit can be represented by a system of linear equations with loop currents as unknowns [44]:

$$j\omega\Psi_{loop} + I_{loop}R + j\omega I_{loop}L = 0 \tag{4.56}$$

where R is the matrix of loop impedances and L is the matrix of self and mutual inductances of the damper network, Ψ_{loop} is the vector of air gap flux linkages, ω is the electrical frequency being considered.

The system of equations can be modified to be of the form

$$Z\ I_{loop} = V_{loop}, \tag{4.57}$$

where Z is the result of superposition of the matrix of loop resistances and the matrix of self and mutual inductances, V_{loop} is a vector of resulting loop voltages, and I_{loop} is a vector of loop currents, where loop currents are enumerated as in Fig. 4.11. Each component of the modified system is described below. The system can be solved for loop currents by any known method, Gaussian elimination and backward substitution being the simplest.

The matrix of loop resistances

Fig. 4.11 shows that two or four loop currents can flow in the interbar R_{bb} branch, depending on whether the interbar branch is adjacent to a loop between the poles. *KVL* equation can be written for each loop. For example, the quantities in the loop 5 are related by

$$I_1R_{bb} - I_2 2R_{bb} + I_3R_{bb} - I_4(z_b + 2R_{bb}) + I_5z_s - I_6(z_b + 2R_{bb}) + I_7R_{bb} - I_8 2R_{bb} + I_9R_{bb} = V_5 \tag{4.58}$$

where $z_b = \frac{z_{\text{bar}}}{n}$, n is number of slices, $z_s = 2z_b + 4R_{bb}$ is self impedance of the loop. After *KVL* equations are written for all loops, they can be combined to form a system of linear equations

$$IR_{\text{loop}} = V_{\text{loop}} \tag{4.59}$$

An example of the loop resistance matrix is shown in Table 4.1. The following notation has been used: $z_e = 2z_b + z_{end} + 2R_{bb}$, $z_s = 2z_b + 4R_{bb}$, $z_c = -(z_b + R_{bb})$ in the first and the last slices and $z_c = -(z_b + 2R_{bb})$ in middle slices, $z_p = 2nz_b + 2z_{p2p}$.

The dimension of a square main block of the loop impedance matrix is the number of loops per pole, $[(N_{\text{bars}} - 1)n + 1]$, where N_{bars} is the number of bars per pole.

The matrix of self and mutual inductances

For each loop, self-inductance and mutual inductances due to magnetic coupling with other loops have to be calculated. It can be noted that self-inductances are equal from pole to pole, therefore, it is enough to calculate

self-inductances on one pole. Moreover, self-inductances do not depend on the axial length, so that calculation of one loop self-inductance between two bars in the first slice provides same value for a subsequent loop between these bars. Mutual inductances should be calculated only within a slice, as there is no magnetic coupling in axial direction: laminations comprising the pole body prevent the flux from going axially. This also means that when constructing the total matrix Z, only main blocks of the loop impedance matrix are covered by the inductance matrix.

Below is the procedure of calculating inductances, as in [44]. A loop produces mmf in the slice over the whole rotor circumference as shown in Fig. 4.12. The amplitude of the mmf produced by the loop may be written as

$$F_{total} = NI = |F_1| + |F_2| \tag{4.60}$$

where $N = 1$ is number of "wire" turns in the loop (one bar is one turn), $I = 1$ is the loop current, F_1 is the mmf magnitude produced inside the loop, and F_2 is the magnitude produced by the loop outside it. In the Fig. 4.12, k and $k+1$ are bar numbers, θ is the angle from the origin to the bar.

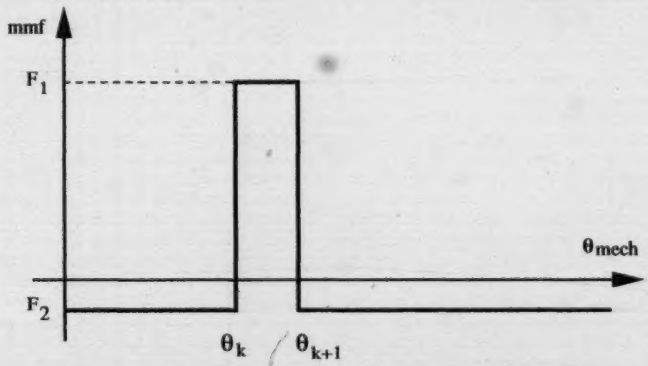

Figure 4.12: Mmf on the total rotor surface produced by one loop.

Due to the continuity principle, the total flux through the surface is zero, so that the flux doing through the loop must equal the flux returning through other loops, or

$$|F_1|P_1 = |F_2|P_2 = \Psi \tag{4.61}$$

Here P_1 and P_2 are permeances of the loop and of the outside of the loop along the air gap circumference. Combining the equations (4.60) and (4.61), one can obtain

$$|F_1| = I\frac{P_2}{P_1 + P_2}, \quad |F_2| = I\frac{P_1}{P_1 + P_2} \tag{4.62}$$

z_e	z_c		$-2R_{bb}$	R_{bb}															$-z_b$
z_c	z_e	z_c	R_{bb}	$-2R_{bb}$	R_{bb}														
	z_c	z_e		R_{bb}	$-2R_{bb}$				$-z_b$										$-z_b$
$-2R_{bb}$	R_{bb}	z_c	z_s	z_c		$-2R_{bb}$	R_{bb}												
R_{bb}	$-2R_{bb}$	R_{bb}	z_c	z_s	z_c	R_{bb}	$-2R_{bb}$	R_{bb}											
	R_{bb}	$-2R_{bb}$		z_c	z_s		R_{bb}	$-2R_{bb}$	$-z_b$										$-z_b$
			$-2R_{bb}$	R_{bb}		z_e	z_c												
			R_{bb}	$-2R_{bb}$	R_{bb}	z_c	z_e	z_c											
				R_{bb}	$-2R_{bb}$		z_c	z_e	$-z_b$										
		$-z_b$			$-z_b$			$-z_b$	z_p	$-z_b$			$-z_b$			$-z_b$			
									$-z_b$	z_e	z_c		$-2R_{bb}$	R_{bb}					
										z_c	z_e	z_c	R_{bb}	$-2R_{bb}$	R_{bb}				
											z_c	z_e		R_{bb}	$-2R_{bb}$				$-z_b$
									$-z_b$	$-2R_{bb}$	R_{bb}		z_s	z_c		$-2R_{bb}$	R_{bb}		
										R_{bb}	$-2R_{bb}$	R_{bb}	z_c	z_s	z_c	R_{bb}	$-2R_{bb}$	R_{bb}	
											R_{bb}	$-2R_{bb}$		z_c	z_s		R_{bb}	$-2R_{bb}$	$-z_b$
									$-z_b$				$-2R_{bb}$	R_{bb}	z_c	z_e	z_c		
													R_{bb}	$-2R_{bb}$	R_{bb}	z_c	z_e	z_c	
														R_{bb}	$-2R_{bb}$		z_c	z_e	$-z_b$
$-z_b$			$-z_b$			$-z_b$						$-z_b$			$-z_b$			$-z_b$	z_p

Table 4.1: Impedance matrix of a damper network for a machine with 2 poles, 4 bars per pole, three slices.

The self-inductance L of the loop can be obtained as

$$L = |F_1|P_1 = \frac{P_1 P_2}{P_1 + P_2} \tag{4.63}$$

and mutual inductance M can be calculated as $|F_2|$ times the permeance of a loop coupled to the current loop.

Loop voltages

Loop voltages exist in open and short circuit due to slotting harmonics of the stator. In open circuit, only the field mmf is present, but the air gap permeance is skewed due to the skewed stator slots, so that the product of the mmf and the permeance waveforms results in the skewed air gap flux density, which permits inter-bar currents to arise. In short circuit, the armature mmf also adds up to the mmf waveform to produce the skewed air gap flux density. A voltage harmonic induced in the loop can be obtained by integrating the air gap flux density harmonic over the surface of the loop and taking the time derivative of the resulting expression.

If the armortisseur bars are partitioned in slices of equal length, all loops between two bars have the same area. In open circuit, the air gap mmf is the "uniform" field mmf, so that the loop voltage respective harmonics have the same magnitudes from slice to slice between two bars. In the presence of both the field and the armature mmf, magnitudes of the loop voltage harmonics are different. Phases of the loop voltage harmonics depend on the axial shift, as shown below, so that the total instantaneous loop voltages cannot be same from slice to slice.

To obtain the n-th harmonic of the loop voltage, the n-th flux density harmonic

$$B_n = \widehat{B}_n \cos(n\theta + \theta_0 + \alpha_n z - \omega_n t) \tag{4.64}$$

should be integrated over a loop from l_1 to l_2 and from θ_1 to θ_2 (Fig. 4.13). Refer to α_n and ω_n as α and ω, respectively. The n-th harmonic of the loop voltage can be determined as

$$V_n = -\frac{\partial \Phi_n}{\partial t} = -\frac{\partial}{\partial t} \int_{l_1}^{l_2} \int_{\theta_1}^{\theta_2} r \widehat{B}_n \cos(n\theta + \theta_0 + \alpha z - \omega t)\, d\theta\, dz \tag{4.65}$$

where r is the pole tip raduis. Integration over θ yields

$$\frac{r}{n} \int_{\theta_1}^{\theta_2} \widehat{B}_n \cos(n\theta + \theta_0 + \alpha z - \omega t)\, d(n\theta) = \widehat{B}_n r K_p \cos\left(\tfrac{n}{2}(\theta_2 + \theta_1) + \theta_0 + \alpha z - \omega t\right) \tag{4.66}$$

where $K_p = \frac{\sin\left(\frac{n}{2}(\theta_2 - \theta_1)\right)}{\frac{n}{2}}$ can be called a pitch factor.

Integrating (4.66) over the length, one can obtain

$$r K_p \int_{l_1}^{l_2} \cos(\alpha z + k)\, dz = r K_p K_s \cos\left(\tfrac{\alpha}{2}(l_2 + l_1) + k\right) \tag{4.67}$$

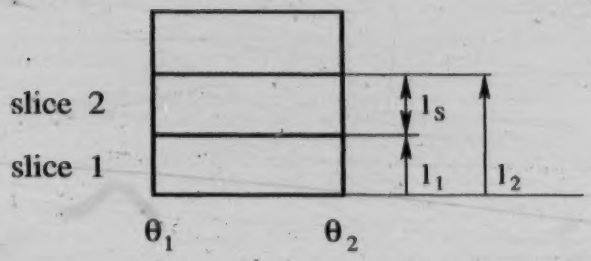

Figure 4.13: Indexing slices in the damper winding.

where $k = \frac{n}{2}(\theta_2 - \theta_1) + \theta_0 - \omega t$, $K_s = \frac{\sin\left(\frac{\alpha}{2}(l_2 - l_1)\right)}{\frac{\alpha}{2}}$ is a skew factor.

Then the loop voltage

$$V_n = -rA_n K_p K_s \frac{\partial}{\partial t} \cos\left(\tfrac{\alpha}{2}(l_2 + l_1) + \tfrac{n}{2}(\theta_2 - \theta_1) + \theta_0 - \omega t\right)$$
$$= rA_n \omega K_p K_s \cos\left(\tfrac{\alpha}{2}(l_2 + l_1) + \tfrac{n}{2}(\theta_2 - \theta_1) + \theta_0 - \omega t + \frac{\pi}{2}\right) \quad (4.68)$$

If the slices are enumerated from the lower end of a damper bar, as shown in Fig. 4.13, then

$$l_2 + l_1 = (2n - 1)l_s \quad (4.69)$$

for the n-th slice. The equation (4.68) can be modified in terms of freqiency, using $\omega = 2\pi f$.

If slices have equal lengths, then $l_2 - l_1 = \text{const}$ and $K_s = \text{const}$ in (4.68). For all loops between two bars, $\theta_2 - \theta_1 = \text{const}$, so that $K_p = \text{const}$ in (4.68). As a result, magnitudes of voltages induced by a single flux density harmonic are same in all loops between two bars, and same between respective bars on all poles. However, phases of the loop voltages differ, as they depend on axial and angular position of the loop.

The inter-bar model is also valid for non-skewed machines. In non-skewed machines, phases of loop voltages do not depend on the axial phase shift $\alpha = 0$, so that loop voltages are identical between adjacent bars.

Bar and interbar currents

Assuming in Fig. 4.11 that bar currents flow down, interbar currents flow from left to right, and loop currents flow clockwise, bar currents are related to loop currents as

$$I_k = I_{loop,\ k} - I_{loop,\ k-1} \quad (4.70)$$

and interbar currents as

$$I_{bb,k} = I_{loop,\ k} - I_{loop,\ k+N_{\text{bars}}-1} \quad (4.71)$$

for the k-th bar.

Damper mmf calculation

An mmf produced by constant current in a loop, formed by two bars connected by end rings, is a rectangular pulse (Fig. 4.14). To determine the loop mmf harmonic contents, Fourier coefficients for the pulse have to be derived. Next, to obtain mmf caused by a time-varying loop current harmonic, the pulse, or the Fourier series, has to be multiplied by the loop current harmonic.

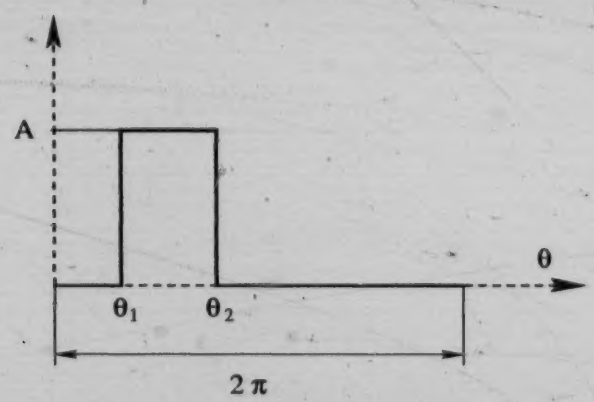

Figure 4.14: Mmf produced by a constant loop current.

Fourier coefficients of a pulse with a constant magnitude. Let the pulse amplitude A be constant, and assume that the pulse exists between angles θ_1 and θ_2, and is zero over the rest of the period of 2π (Fig. 4.14). Then the pulse function can be expanded to Fourier series

$$f(\theta) = a_0 + \sum_{n=1}^{\infty}(a_n \cos(n\theta) + b_n \sin(n\theta)) \tag{4.72}$$

The dc component does not have to be calculated, because a dc component produced by a loop over one pole is cancelled by a dc component produced by a respective loop over the pole of opposite polarity. Ignoring the dc component, the Fourier coefficients can be computed as

$$a_n = \frac{2}{T}\int_T f(\theta)\cos(n\theta)\ d\theta = \frac{1}{\pi}\int_{\theta_1}^{\theta_2} A\cos(n\theta)\ d\theta = \frac{A}{\pi n}(\sin(n\theta_2) - \sin(n\theta_1))$$
$$= \frac{2A}{\pi n}\sin\left[\frac{n}{2}(\theta_2 - \theta_1)\right]\cos\left[\frac{n}{2}(\theta_2 + \theta_1)\right]$$

$$b_n = \frac{2}{T}\int_T f(\theta)\sin(n\theta)\ d\theta = \frac{1}{\pi}\int_{\theta_1}^{\theta_2} A\sin(n\theta)\ d\theta = -\frac{A}{\pi n}(\cos(n\theta_2) - \cos(n\theta_1))$$
$$= \frac{2A}{\pi n}\sin\left[\frac{n}{2}(\theta_2 - \theta_1)\right]\sin\left[\frac{n}{2}(\theta_2 + \theta_1)\right]$$

Then the function is computed as

$$f(\theta) = \sum_{n=1}^{\infty} \frac{2A}{\pi n} \times$$
$$\sin\left[\frac{n}{2}(\theta_2 - \theta_1)\right]\left(\cos\left[\frac{n}{2}(\theta_2 + \theta_1)\right]\cos(n\theta) + \sin\left[\frac{n}{2}(\theta_2 + \theta_1)\right]\sin(n\theta)\right)$$

to become

$$f(\theta) = \frac{2A}{\pi}\sum_{n=1}^{\infty} \frac{\sin\left[\frac{n}{2}(\theta_2 - \theta_1)\right]}{n}\cos n\left[\theta - \frac{\theta_2 + \theta_1}{2}\right] \tag{4.73}$$

MMF as a pulse with time-varying magnitude. Loop current can be represented as a sum of harmonics varying with time:

$$I(t) = \sum_m I_m \cos(\omega_m t + \phi_m) \tag{4.74}$$

For simplicity, refer to quantities of the m-th harmonic as I, ω, ϕ, omitting the subscripts. Multiplying the pulse of unity magnitude $A = 1$ by the loop current harmonic,

$$I_m \times f(\theta) = I\cos(\omega t + \phi)\,\frac{2A}{\pi}\sum_{n=1}^{\infty} \frac{\sin\left[\frac{n}{2}(\theta_2 - \theta_1)\right]}{n}\cos\, n\left(\theta - \frac{\theta_2 + \theta_1}{2}\right) \tag{4.75}$$

one can obtain

$$f(\theta, t) = \frac{I}{\pi}\sum_{n=1}^{\infty} \frac{\sin\left[\frac{n}{2}(\theta_2 - \theta_1)\right]}{n}\left[\cos(\omega t + n\theta + \Phi_1) + \cos(\omega t - n\theta - \Phi_2)\right] \tag{4.76}$$

where

$$\Phi_1 = -\phi + n\frac{\theta_2 + \theta_1}{2}, \qquad \Phi_2 = \phi + n\frac{\theta_2 + \theta_1}{2} \tag{4.77}$$

Variation of damper loop currents and mmf with axial position. Damper loop currents vary with time and axial coordinate. Suppose that the damper network has been partitioned in a number of slices in axial direction. Between two bars, all loops produce loop currents of different magnitudes and phases. A magnitude and a phase allow to represent a loop current by a complex number. Then moving in axial direction from slice to slice, one can obtain a complex-valued function versus axial coordinate.

With a known number of points, an analytical form of the function versus axial position can be obtained using any kind of a polynomial. Dealing with harmonics, it is traditional to use Fourier series, and to represent complex numbers, an exponential form of Fourier series is the most convenient. From a five-slice model, five points are available, and the polynomial to approximate the finction has five terms:

$$I_m(z) = I_0 + I_1 e^{-j\omega z} + I_2 e^{-j2\omega z} + I_3 e^{-j3\omega z} + I_4 e^{-j4\omega z} = \sum_{k=0}^{4} I_k e^{-jk\omega z} \tag{4.78}$$

where $\omega = \frac{2\pi}{T}$, and T is an arbitrarily chosen period of the function. The period should be a fraction or a multiple of the machine length, as the function I_m is considered versus longitudinal position. Also, is is desirable to have the damper loop current as a function of skew. Thus the period can be chosen to yield ω

$$\omega = \frac{2\pi}{T} = 2\pi\frac{\alpha}{l_s} \tag{4.79}$$

where α is skew in slot pitches, l_s is the length of the stator stack.

The coefficients I_0, I_1, ..., I_4 of the function I_m can be found by solving a system of equations

$$I_0 + I_1 e^{-j\omega z_1} + I_2 e^{-j2\omega z_2} + I_3 e^{-j3\omega z_3} + I_4 e^{-j4\omega z_4} = I_{m,1} \tag{4.80}$$
$$I_0 + I_1 e^{-j\omega z_1} + I_2 e^{-j2\omega z_2} + I_3 e^{-j3\omega z_3} + I_4 e^{-j4\omega z_4} = I_{m,2} \tag{4.81}$$
$$I_0 + I_1 e^{-j\omega z_1} + I_2 e^{-j2\omega z_2} + I_3 e^{-j3\omega z_3} + I_4 e^{-j4\omega z_4} = I_{m,3} \tag{4.82}$$
$$I_0 + I_1 e^{-j\omega z_1} + I_2 e^{-j2\omega z_2} + I_3 e^{-j3\omega z_3} + I_4 e^{-j4\omega z_4} = I_{m,4} \tag{4.83}$$
$$I_0 + I_1 e^{-j\omega z_1} + I_2 e^{-j2\omega z_2} + I_3 e^{-j3\omega z_3} + I_4 e^{-j4\omega z_4} = I_{m,5} \tag{4.84}$$

where $I_{m,i}$ is a complex number representing the damper loop current m-th harmonic in the i-th slice.

The final expression for a harmonic of the damper mmf is product of (4.73) and (4.78):

$$f(\theta, t, \alpha) = f(\theta) \sum_{k=0}^{4} I_k e^{-jk\omega z} \tag{4.85}$$

Collecting all harmonics of the damper loop current, the expression becomes

$$f(\theta, t, \alpha) = f(\theta) \sum_{m} \sum_{k=0}^{4} I_k e^{-jk\omega z} \tag{4.86}$$

Chapter 5

Prediction of losses that depend on skew

The varying skewed magnetic field in the air gap affects losses in iron of the machine and in bars of the armortisseur winding. As a result, one needs to consider iron loss of the stator, the pole face loss, the loss caused by inter-bar currents in the pole iron, and also the joule loss in the armortisseur bars.

It is shown below that while eddy current loss depends on the flux density harmonic magnitude squared, hysteresis and excess loss depend on the peak value of the flux density instantaneous curve. In each lamination, the instantaneous curve is different due to harmonic axial phase shifts, so that iron losses obtained in a skewed machine differ from those of an unskewed machine.

Losses due to conductor currents induced in the skewed magnetic field may be computed by Ohm's Law. The damper ohmic loss is obtained as

$$P_d = I^2 R_{\text{ac}} \tag{5.1}$$

where I is the magnitude of the current harmonic in the conductor, R_{ac} is the ac resistance of the conductor at the harmonic frequency. Interbar iron loss can be calculated as

$$P_{\text{ib}} = I_{\text{ib}}^2 R_{\text{c}} \tag{5.2}$$

where R_c is the contact resistance.

5.1 Magnetic field in iron of the stator

The air gap flux density distribution can be used to obtain the flux density distribution in iron of the stator, namely, in the teeth and the back of the stator. Then the iron losses in the stator can be evaluated.

5.1.1 Magnetic flux density in the stator tooth

The stator tooth and the flux lines entering the tooth from the air gap are shown in Fig. 5.1. The figure can be described by the following assumptions:

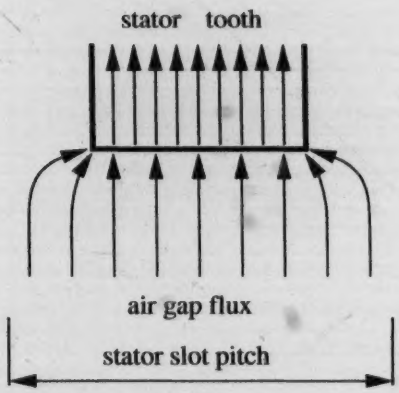

Figure 5.1: Flux lines outside and inside the tooth.

1. All flux lines over the stator slot pitch go to the tooth. By this assumption, because the tooth cross-sectional area is less than the one of the slot pitch, the number of flux lines remains the same, but their density is higher in the tooth.
2. All flux lines enter the tooth near the tooth tip.
3. Flux density has zero tangential component in the tooth.
4. The harmonic flux is uniform in the tooth at one depth, in the sense that each point at same depth of the tooth "sees" the same magnitude of flux.

If the period of the space harmonic of the air gap flux density is less than width of the tooth tip, one can assume that presence of tooth edges does not affect the harmonic. When entering the iron, the harmonic magnitude is unchanged. Magnitudes of the space harmonics with periods larger than the tooth tip must increase in iron in the manner

$$B_{m,\text{tooth}} S_{\text{tooth tip}} = B_{m,\text{gap}} S_{\text{slot pitch}} \tag{5.3}$$

$$B_{m,\text{tooth}} = \frac{S_{\text{slot pitch}}}{S_{\text{tooth tip}}} B_{m,\text{gap}} \tag{5.4}$$

where B_m is flux density magnitude, S is cross-sectional area.

In the axial direction, magnetic field is also non-uniform. Stator laminations of large synchronous machines are arranged in packets with spaces (ducts) between them. All flux lines over the "packet pitch" are assumed to go into iron of the stator packet, as shown in Fig. 5.2, and magnetic flux density in the packets increases.

Carter's equivalent model of a slotted surface against a smooth one can be used to account for the increase in magnetic flux density due to ducting [104].

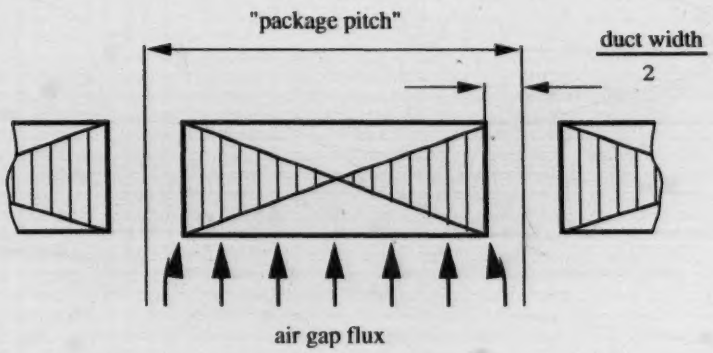

Figure 5.2: Flux lines entering a stator packet.

A packet and a duct of the total length λ can be replaced by an equivalent iron packet of smaller length, calculated as

$$\lambda' = \lambda - \sigma w, \tag{5.5}$$

where w is width occupied by air over the slot pitch, and σ is calculated as

$$\sigma = \frac{2}{\pi}\left[\tan^{-1}\left(\frac{w}{2g}\right) - \frac{g}{w}\ln\left(1+\left(\frac{w}{2g}\right)^2\right)\right]. \tag{5.6}$$

Carter's coefficient

$$K_c = \frac{\lambda}{\lambda'} \tag{5.7}$$

can also be used to scale the air gap magnetic flux density harmonic, when it enters the tooth.

While the flux travels down the tooth, its magnitude decays with depth. A *penetration depth*, which is the depth where the wave magnitude decays to e^{-1} of its value on the surface, can be calculated as [23]

$$\Delta = \frac{d}{2p}, \tag{5.8}$$

where d is diameter, in this case of the stator bore, and $2p = 2n$ is the number of poles of the n-th space harmonic counted at the period of the fundamental harmonic. It is convenient to partition the stator tooth in a number of layers, as shown in Fig. 5.3. For each flux density harmonic, its penetration depth can be computed and compared with the depth of the i-th layer h_i. If the penetration depth is greater than the depth of the layer, the harmonic can be assumed to exist in the layer and to cause iron losses.

The phase shift of the n-th harmonic of the flux density in the k-th tooth of one lamination can be computed as (Fig. 5.4)

$$\xi_{\Phi_n} = n\theta + \xi_{B_n} + \frac{\alpha_n}{l}z, \tag{5.9}$$

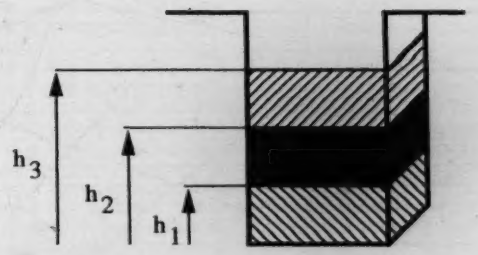

Figure 5.3: A stator tooth partitioned in layers.

where z is axial coordinate of the lamination, $\theta = \theta_0 + (k-1)\gamma$ is angular position of the k-th tooth, $\theta_0 = \beta\frac{z}{l}$ is the initial angular phase delay, β is skew in mechanical radians, l is the stator length, $\gamma = \frac{2\pi}{N_s}$ is the stator slot pitch angle, N_s is the number of stator slots, ξ_{B_n} is phase shift of the magnetic flux density harmonic, α_n is axial shift of the n-th harmonic of the magnetic flux density.

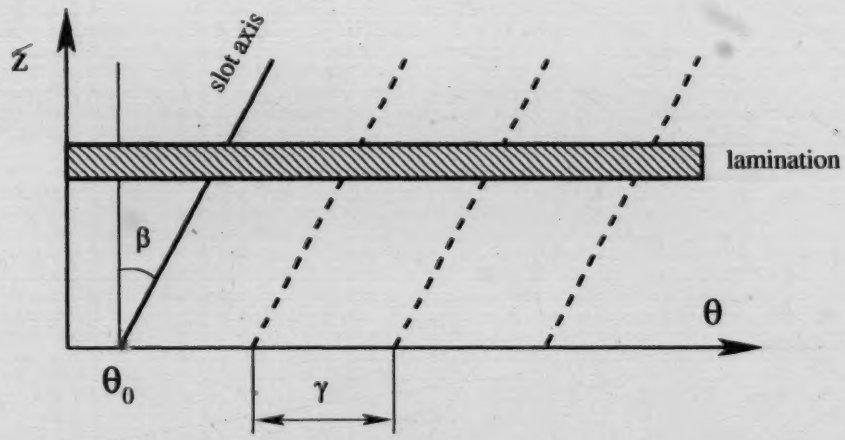

Figure 5.4: To the calculation of the tooth flux phase.

The most accurate picture of losses could be obtained, if the flux density distribution in the teeth of the stator was evaluated in each lamination. However, this considerably slows down computations. As a compromise between accuracy and computational speed, the flux density distribution can be obtained in a middle lamination of each stator packet, and can be considered approximately constant along the packet.

5.1.2 Stator back fluxes in open circuit

The magnitude of the flux harmonic entering the yoke of the stator can be calculated as product of the flux density harmonic magnitude in the deepest layer of the tooth and the cross-sectional area of the layer. The phase shift of

the flux harmonic is the same as of the corresponding flux density harmonic. When magnetic fluxes leaving the stator teeth are known, fluxes flowing in the stator yoke can be estimated. Consider magnetic circuit shown in Fig. 5.5, where x_i is a flux in the i-th segment of the stator back between adjacent teeth, and Φ_i is a flux coming from the i-th tooth. The following observations can be made:

- The stator back flux that leaves the last segment is the same as the flux that enters the first segment.
- According to magnetic flux continuity principle, the sum of tooth fluxes should be equal to zero.
- According to the same principle, the sum of back segment fluxes should be equal to zero.

It is assumed that the magnetic flux harmonic in the yoke does not decay with depth, which is a good approximation for a synchronous machine in open circuit [83].

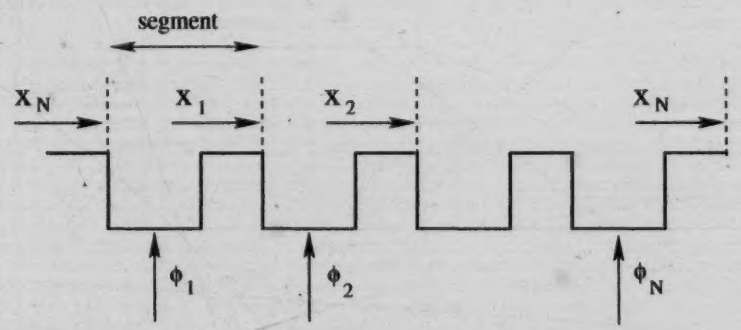

Figure 5.5: Fluxes outside and inside the stator yoke.

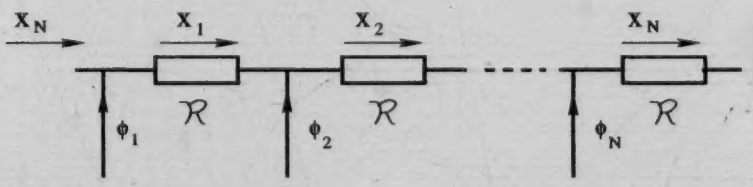

Figure 5.6: The magnetic circuit for stator flux calculation.

From Fig. 5.6, the first Kirchoff's law for each node can be written as

$$x_1 = x_n + \Phi_1 \tag{5.10}$$
$$x_2 = x_1 + \Phi_2 \tag{5.11}$$
$$\vdots \tag{5.12}$$
$$x_n = x_{n-1} + \Phi_n \tag{5.13}$$

and the equations organized in the matrix form. For simplicity of illlustration, assume that the machine has six slots:

$$\begin{bmatrix} 1 & 0 & 0 & 0 & 0 & -1 \\ -1 & 1 & 0 & 0 & 0 & 0 \\ 0 & -1 & 1 & 0 & 0 & 0 \\ 0 & 0 & -1 & 1 & 0 & 0 \\ 0 & 0 & 0 & -1 & 1 & 0 \\ 0 & 0 & 0 & 0 & -1 & 1 \end{bmatrix} \begin{bmatrix} x_1 \\ x_2 \\ x_3 \\ x_4 \\ x_5 \\ x_6 \end{bmatrix} = \begin{bmatrix} \Phi_1 \\ \Phi_2 \\ \Phi_3 \\ \Phi_4 \\ \Phi_5 \\ \Phi_6 \end{bmatrix} \tag{5.14}$$

Solving the system by Gaussian elimination and back substitution yields

$$\begin{bmatrix} 1 & 0 & 0 & 0 & 0 & -1 \\ 0 & 1 & 0 & 0 & 0 & -1 \\ 0 & 0 & 1 & 0 & 0 & -1 \\ 0 & 0 & 0 & 1 & 0 & -1 \\ 0 & 0 & 0 & 0 & 1 & -1 \\ 0 & 0 & 0 & 0 & 0 & 0 \end{bmatrix} \begin{bmatrix} x_1 \\ x_2 \\ x_3 \\ x_4 \\ x_5 \\ x_6 \end{bmatrix} = \begin{bmatrix} \Phi_1 \\ \Phi_1 + \Phi_2 \\ \Phi_1 + \Phi_2 + \Phi_3 \\ \Phi_1 + \Phi_2 + \Phi_3 + \Phi_4 \\ \Phi_1 + \Phi_2 + \Phi_3 + \Phi_4 + \Phi_5 \\ \Phi_1 + \Phi_2 + \Phi_3 + \Phi_4 + \Phi_5 + \Phi_6 \end{bmatrix} \tag{5.15}$$

The last row confirms the second observation, but the matrix is singular, so that the system does not have a unique solution! One needs either to define one unknown, to make one variable less in the system, or to add another equation.

The third observation can be used to complete the system of equations,

$$x_6 = -(x_1 + x_2 + ... + x_5). \tag{5.16}$$

To make the matrix smaller (and solution faster), the equation (5.16) can be used to reduce the original number of unknowns in the system by one, and solve for the last unknown x_n separately afterwards. If the equation (5.16) holds, then instead of the equation (5.10) for $n = 6$ one can write

$$2x_1 + x_2 + x_3 + x_4 + x_5 = \Phi_1, \tag{5.17}$$

and the reduced system becomes

$$\begin{bmatrix} 2 & 1 & 1 & 1 & 1 \\ -1 & 1 & 0 & 0 & 0 \\ 0 & -1 & 1 & 0 & 0 \\ 0 & 0 & -1 & 1 & 0 \\ 0 & 0 & 0 & -1 & 1 \end{bmatrix} \begin{bmatrix} x_1 \\ x_2 \\ x_3 \\ x_4 \\ x_5 \end{bmatrix} = \begin{bmatrix} \Phi_1 \\ \Phi_2 \\ \Phi_3 \\ \Phi_4 \\ \Phi_5 \end{bmatrix} \tag{5.18}$$

It can be shown that this system of equations can be quickly solved using "incomplete" Gaussian elimination. The system can be rearranged as

$$\begin{bmatrix} 2 & 1 & 1 & 1 & 1 \\ 0 & 3 & 1 & 1 & 1 \\ 0 & 0 & 4 & 1 & 1 \\ 0 & 0 & 0 & 5 & 1 \\ 0 & 0 & 0 & 0 & 6 \end{bmatrix} \begin{bmatrix} x_1 \\ x_2 \\ x_3 \\ x_4 \\ x_5 \end{bmatrix} = \begin{bmatrix} \Phi_1 \\ \Phi_1 + 2\Phi_2 \\ \Phi_1 + 2\Phi_2 + 3\Phi_3 \\ \Phi_1 + 2\Phi_2 + 3\Phi_3 + 4\Phi_4 \\ \Phi_1 + 2\Phi_2 + 3\Phi_3 + 4\Phi_4 + 5\Phi_5 \end{bmatrix} \tag{5.19}$$

Denote $S_w = \Phi_1 + 2\Phi_2 + 3\Phi_3 + 4\Phi_4 + 5\Phi_5$. The last unknown in the system is found as

$$x_5 = \tfrac{1}{6} S_w. \tag{5.20}$$

Then

$$\begin{aligned} 5x_4 + x_5 &= 5x_4 + \tfrac{1}{6} S_w = S_w - 5\Phi_5 && (5.21)\\ 5x_4 &= \tfrac{5}{6} S_w - 5\Phi_5 && (5.22)\\ x_4 &= \tfrac{1}{6} S_w - \Phi_5 = x_5 - \Phi_5, && (5.23) \end{aligned}$$

For the next unknown, from row 3 in (5.19) we have

$$\begin{aligned} 4x_3 + x_4 + x_5 &= S_w - 5\Phi_5 - 4\Phi_4 && (5.24)\\ 4x_3 &= S_w - 5\Phi_5 - 4\Phi_4 - x_4 - x_5 && (5.25) \end{aligned}$$

From row 4 in (5.19), we have $5x_4 = S_w - 5\Phi_5 - x_5$, so that

$$\begin{aligned} 4x_3 &= 5x_4 - 4\Phi_4 - x_4 = 4x_4 - 4\Phi_4 && (5.26)\\ x_3 &= x_4 - \Phi_4 && (5.27) \end{aligned}$$

Similarly, it can be shown that for each unknown x_i in the system, except the last, x_{n-1},

$$x_i = x_{i+1} - \Phi_{i+1}. \tag{5.28}$$

The n-th element in the system of equations is calculated as

$$x_n = \frac{1}{n} \sum_{k=1}^{n-1} \Phi_k \tag{5.29}$$

and the last element in the original system of equations is calculated according to the continuity principle,

$$x_{n+1} = -\sum_{k=1}^{n} x_k. \tag{5.30}$$

The magnitude of a magnetic flux density harmonic in a segment can be determined as the ratio of the flux harmonic magnitude and the cross-sectional area of the stator back traversed by the flux.

5.2 Formulae for iron loss evaluation

Iron losses are traditionally classified as *eddy current* losses and *hysteresis* losses. Eddy current loss can be further divided in traditional eddy current loss, produced by eddy currents in iron, and *excess* loss, due to eddy currents flowing on the moving domain walls [80].

5.2.1 Traditional eddy current loss

Alternatively to eddy current loss density per unit mass [23, 80], eddy current per unit volume loss density can be calculated as

$$P_e = \frac{\sigma d^2}{12}\frac{1}{T}\int_T \left(\frac{dB}{dt}\right)^2 dt \tag{5.31}$$

where σ is the material conductivity, d is the lamination thickness, T is the period of the fundamental frequency, B is flux density.

The integral in this expression can be obtained in the closed form for each harmonic of flux density, as shown in Appendix B. The total volumetric eddy current loss density becomes

$$P_e = \frac{\sigma d^2}{24}\left((\hat{B}_1\,\omega_1)^2 + (\hat{B}_2\,\omega_2)^2 + \cdots + (\hat{B}_n\,\omega_n)^2\right) = \frac{\sigma d^2}{24}\sum_{i=1}^{n}(\hat{B}_i\,\omega_i)^2, \tag{5.32}$$

where $\hat{B}_i$ is the magnitude of the flux density harmonic, ω_i is the harmonic frequency.

5.2.2 Excess loss

The excess eddy current loss per unit mass can be evaluated as [80]

$$P_{ex} = \frac{K_e}{T}\int_T \left|\frac{dB}{dt}\right|^{1.5} dt \tag{5.33}$$

where K_e is a constant found experimentally, T is the period of the fundamental frequency.

The instantaneous, or time-domain, magnetic flux density waveform has to be re-constructed from the flux density harmonic series to calculate the excess loss. If the instantaneous flux density is known over the period with the step Δt, the expression (5.33) can be approximated as

$$P_{ex} = \frac{K_e}{T}\sum_T \left|\frac{\Delta B}{\Delta t}\right|^{1.5}\Delta t = \frac{K_e}{T\sqrt{\Delta t}}\left|\Delta B_1 + \Delta B_2 + \cdots + \Delta B_n\right|^{1.5} \tag{5.34}$$

or

$$P_{ex} = \frac{K_e f_1}{\sqrt{\Delta t}}\left|\Delta B_1 + \Delta B_2 + \cdots + \Delta B_n\right|^{1.5} \tag{5.35}$$

where $T = \frac{1}{f_1}$, f_1 is fundamental frequency.

5.2.3 Hysteresis loss

The hysteresis phenomenon is better described not just by one hysteresis loop, but by the loop with the boundary distorted to form minor loops, as flux density "randomly" reverses during magnetisation due to higher-order harmonics.

These minor loops produce additional losses that can be evaluated as shown below. The hysteresis loss density per unit mass, with an account of the minor loop (or higher harmonic) losses, can be calculated as in [23, 80], using the fundamental frequency of the flux density:

$$P_h = K_n f_1 B_p^{\alpha} K, \tag{5.36}$$

where K_h and α are constants determined experimentally, B_p is the peak value of the flux density. K is given by [84]

$$K = 1 + \frac{k}{B_p} \sum_{i=1}^{n} |\Delta B_i| \tag{5.37}$$

where k is a constant between 0.6 and 0.7, ΔB_i is magnitude of the i-th "dip", as shown in Fig. 5.7, on the positive half-cycle of magnetic flux density instantaneous curve over the period T.

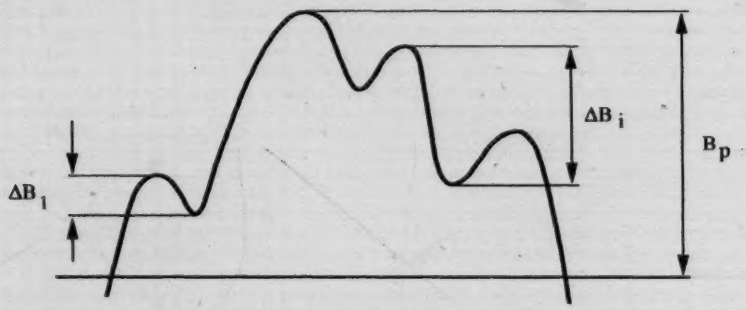

Figure 5.7: Magnetic flux density curve.

To calculate the hysteresis loss, the instantaneous waveform of the flux density has to be calculated from the flux density harmonic series.

5.3 Pole face loss

This section describes computation of the pole face loss in laminated poles of a skewed machine [105].

5.3.1 Computation of magnetic field in a lamination

To facilitate the problem of computing magnetic field in iron, the following assumptions are adopted:

1. Magnetic flux does not travel in the axial direction.
2. The radius of the pole is large, so that the problem can be considered in Cartesian coordinates.

3. A harmonic of field intensity has axial phase shift α negligible across one lamination.

4. End effects are ignored.

5. Hysteresis losses are negligible.

Let the coordinate system be located as shown in Fig. 5.8. In the pole iron, the following magnetostatic equations must be valid:

$$\nabla \cdot \mathbf{H} = 0 \tag{5.38}$$

$$\nabla \times \mathbf{H} = \mathbf{J} \tag{5.39}$$

where $\mathbf{H} = [H_x \; H_y \; H_z]$ is magnetic field intensity and $\mathbf{J} = [J_x \; J_y \; J_z]$ is eddy current density in the iron.

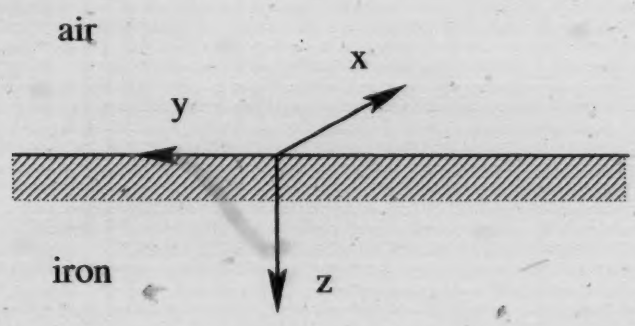

Figure 5.8: Cartesian coordinates for computation of magnetic field in the pole.

Taking curl of both sides of (5.39) and using equations

$$\mathbf{J} = \sigma \mathbf{E} \tag{5.40}$$

$$\nabla \times \mathbf{E} = -\frac{\partial \mathbf{B}}{\partial t} \tag{5.41}$$

$$\mathbf{B} = \mu \mathbf{H} \tag{5.42}$$

$$\nabla \times \nabla \times A = \nabla(\nabla \cdot A) - \nabla^2 A \tag{5.43}$$

and (5.38), one can obtain the Helmholz equation

$$\nabla^2 \mathbf{H} = j\sigma\mu\omega\mathbf{H} \tag{5.44}$$

for a sinusoidal function $\mathbf{H}$ of angular frequency ω. A general solution for this equation can be written as

$$\mathbf{H} = \mathbf{h}e^{-\gamma z}e^{j(\omega t - ky - \alpha x)} = [H_x \; H_y \; H_z] \tag{5.45}$$

where $\mathbf{h} = [h_x\ h_y\ h_z]$, γ and k are constants, $\alpha = 0$ is axial phase shift of magnetic field intensity. The components of the field intensity harmonic can be written as

$$H_x = h_x e^{-\gamma z} e^{j(\omega t - ky)} \tag{5.46}$$
$$H_y = h_y e^{-\gamma z} e^{j(\omega t - ky)} \tag{5.47}$$
$$H_z = h_z e^{-\gamma z} e^{j(\omega t - ky)} \tag{5.48}$$

To compute pole face loss, the magnetic field intensity components have to be found. By Assumption 1, $H_x = 0$. Consider the component H_z. By (5.44),

$$\frac{\partial^2 H_z}{\partial x^2} + \frac{\partial^2 H_z}{\partial y^2} + \frac{\partial^2 H_z}{\partial z^2} = j\sigma\mu\omega H_z \tag{5.49}$$

so that

$$\frac{\partial^2 H_z}{\partial x^2} = g^2 H_z \tag{5.50}$$

where

$$g^2 = j\sigma\mu\omega + k^2 - \gamma^2 \tag{5.51}$$

A standard solution for the wave equation (5.50) is

$$H_z = \mathbf{Re}\{(H_1 e^{gx} + H_2 e^{-gx}) e^{-\gamma x} e^{j(\omega t - ky)}\} \tag{5.52}$$

In the middle of the packet, H_z is homogeneous over the lamination, so that

$$H_z\left(\tfrac{h}{2}, y, z, t\right) = H_z\left(-\tfrac{h}{2}, y, z, t\right) \tag{5.53}$$
$$H_1 = H_2 \tag{5.54}$$

Now the constants k and γ should be found. Using (5.38), one can obtain

$$\frac{\partial H_y}{\partial y} + \frac{\partial H_z}{\partial z} = 0 \tag{5.55}$$
$$-jk\,h_y - \gamma h_z = 0 \tag{5.56}$$

Using (5.39) and Assumption 1, $J_x = 0$, one can obtain

$$\frac{\partial H_y}{\partial z} + \frac{\partial H_z}{\partial y} = 0 \tag{5.57}$$
$$-\gamma h_y + jk\,h_z = 0 \tag{5.58}$$

For nonzero h_y, h_z equations (5.56) and (5.58) can hold only if

$$k = \gamma \tag{5.59}$$

In cylindrical coordinates,

$$y = R\theta \tag{5.60}$$
$$m\theta = \frac{m}{R} y = ky \tag{5.61}$$
$$k = \frac{m}{R} \tag{5.62}$$

where m is order of the space harmonic, R is the radius of the pole face, measured from the centre of the shaft.

The magnetic field intensity components are related by (5.56), which gives

$$h_y = j\, h_z \tag{5.63}$$

and the magnetic field intensity becomes

$$\mathbf{H} = \begin{bmatrix} H_x \\ H_y \\ H_z \end{bmatrix} = \begin{bmatrix} 0 \\ jH_1(e^{gx} + e^{-gx})e^{-\gamma z}e^{j(\omega t - ky)} \\ H_1(e^{gx} + e^{-gx})e^{-\gamma z}e^{j(\omega t - ky)} \end{bmatrix} \tag{5.64}$$

where

$$g^2 = j\sigma\mu\omega \tag{5.65}$$

To determine H_1, a normal flux density boundary condition on the pole surface can be used (Fig. 5.9):

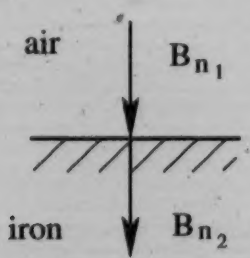

Figure 5.9: Equality of normal components of magnetic field density.

$$B_{\mathrm{n,\,air}} = B_{\mathrm{n,iron}} = \mu H_z \tag{5.66}$$

The magnetic flux density harmonic in air can be expressed as

$$B_{\mathrm{n,\,air}} = \widehat{B}e^{j(\omega t - ky - \alpha_B x)} \tag{5.67}$$

where α_B is magnetic flux density axial phase shift. Integration over the lamination width along x-axis, where $y = 0$, $z = 0$, and $t = 0$ for the air gap field stationary with respect to the rotor surface

$$\int_{-\frac{h}{2}}^{\frac{h}{2}} \mu H_z\, dx = \int_{-\frac{h}{2}}^{\frac{h}{2}} \widehat{B}\cos(\alpha_B x)\, dx \tag{5.68}$$

where h is the lamination width, gives

$$H_1 = \frac{g\, h\widehat{B}}{4\mu \sinh\left(\frac{h}{2}g\right)} \tag{5.69}$$

Using an identity

$$(Ae^{i\phi})^2 = A^2 e^{i2\phi} \tag{5.70}$$

the equation (5.65) can be expressed as

$$g^2 = \sigma\mu\omega e^{j\frac{\pi}{2}} \tag{5.71}$$

$$g = \frac{1+i}{\sqrt{\frac{2}{\sigma\mu\omega}}} = \frac{1+i}{\Gamma} \tag{5.72}$$

where $\Gamma = \sqrt{\frac{2}{\sigma\mu\omega}}$ is classical penetration (skin) depth.

5.3.2 Eddy current density in a lamination

The eddy current density is found from (5.39), using $H_x = 0$, $H_y = jH_z$, $J_x = 0$:

$$\mathbf{J} = \begin{bmatrix} J_x \\ J_y \\ J_z \end{bmatrix} = \begin{bmatrix} \frac{\partial H_z}{\partial y} - \frac{\partial H_z}{\partial x} \\ \frac{\partial H_x}{\partial z} - \frac{\partial H_z}{\partial x} \\ \frac{\partial H_y}{\partial x} - \frac{\partial H_x}{\partial y} \end{bmatrix} = \begin{bmatrix} 0 \\ -\frac{\partial H_z}{\partial x} \\ j\frac{\partial H_z}{\partial x} \end{bmatrix} = \begin{bmatrix} 0 \\ -J_0 \\ jJ_0 \end{bmatrix} \tag{5.73}$$

where

$$J_0 = \frac{j\omega\sigma h\widehat{B}}{4\mu \sinh\left(\frac{gh}{2}\right)}(e^{gx} + e^{-gx})e^{-\gamma z}e^{j(\omega t - ky)} \tag{5.74}$$

5.3.3 Computation of the pole face loss

The volumetric power loss density may be defined as

$$W = \frac{1}{2\sigma}\mathbf{J}\cdot\mathbf{J}^* = \frac{1}{2\sigma}(J_y J_y^* + J_z J_z^*) = \frac{1}{\sigma}J_0 J_0^* \tag{5.75}$$

Using equations (5.72) and (5.74), the loss density can be expressed as

$$W = \frac{\omega^2\sigma h^2\widehat{B}^2 e^{-2kz}}{8\left(\sinh^2\frac{h}{2\Gamma} + \sin^2\frac{h}{2\Gamma}\right)}\left(\cosh\tfrac{2x}{\Gamma} - \cos\tfrac{2x}{\Gamma}\right) \tag{5.76}$$

The eddy current loss in one lamination due to one harmonic may be found as

$$P = \int_{y_0}^{y_1}\int_0^{\infty}\int_{-\frac{h}{2}}^{\frac{h}{2}} W\,dx\,dy\,dz \tag{5.77}$$

where y_0 and y_1 are coordinates of the ends of the pole.

Chapter 6

Validation of the analytical model

In Chapters 4 and 5, the analytical model predicting magnetic fields and losses in a salient-pole skewed synchronous machine has been developed. An important part of the work is validation of the model by comparison of the obtained results with test or with another model. The manufacturer's data, used to validate the model, include measurements of voltage harmonic spectrum in open circuit in five large machines, open circuit and short circuit loss data in these machines, measurements of air gap flux density in one machine, voltage harmonic spectrum for the five machines obtained by nonlinear magnetostatic FEA of an unskewed machine. Ratings of the machines are shown in Table 6.1.

	Rated power,kVA	Rated voltage, V	Skew	Type of winding
Machine 1	14089	13800	1	integral
Machine 2	17889	13800	0	fractional-slot
Machine 3	7000	4160	1	integral
Machine 4	8667	13800	0	fractional-slot
Machine 5	1278	2400	1	integral

Table 6.1: Machine data.

6.1 Prediction of magnetic flux density

To evaluate losses accurately, it is necessary to accurately predict magnetic flux density in the machine. In machines of a smaller size, flux density can be measured to check a model. For large machines, this measurement is not included into routine testing; it takes time, and a manufacturer cannot generally afford time delays. The measurement of air gap flux density in Machine 5 is provided for comparison with simulation results.

The measurement of flux density is performed by placing a test coil around one tooth of each packet and measuring voltage induced in the coil. The

flux density can be calculated from the measured voltage. In this way, the flux density in steel of the tooth tip is measured, rather than in the air gap. Therefore, the resulting flux density is expected to be higher than the air gap flux density. The tooth in each packet has been skewed, as opposed to measurement taken at one point in the space, which causes slight inaccuracy.

The test and the simulation results are shown in Figs. 6.1-6.4.

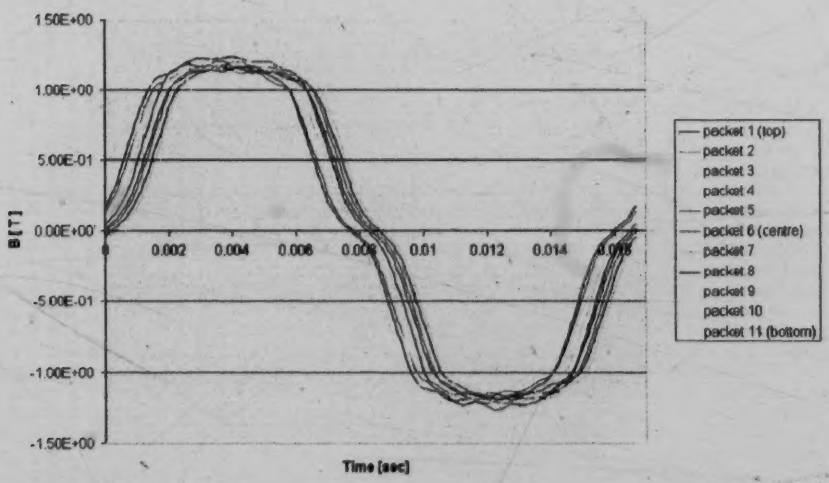

Figure 6.1: Air gap flux density in Machine 5, obtained by test.

It is shown in Fig. 6.1 that the magnitude of measured magnetic flux density varies between 1.15 and 1.3 T. The magnitude of the simulated air gap flux density waveform (Fig. 6.2) is close to 0.99 T, a value also obtained by FEA. As expected, it is somewhat less than the measured value. The magnetic field has been simulated at the rated field current. Magnetic flux density slightly varies in magnitude (Figs. 6.1, 6.3 and 6.4), depending on length of the magnetic path; for example, a "tooth-against-tooth" path in one instant of time provides the shortest magnetic path, and the flux magnitude is the highest in this instant.

A ripple on the top of the flux density waveform is caused by slotting of the stator and the pole. Measurement exhibits the smaller magnitude of the ripple, compared with the calculated ripple (Figs. 6.1 and 6.2). The smaller magnitude of the ripple can be explained by averaging the magnetic flux density over the slot pitch. The measured flux density is determined as the voltage in the test coil integrated over the area of the skewed tooth along the stator packet and scaled by the area of the tooth. The method causes averaging of the "peak and dip" information over the slot pitch.

The air gap flux density magnitude depends on the bar-to-iron contact resistance of the armortisseur winding. It is shown below that the open circuit voltage, induced by the air gap magnetic field, and losses depend on the

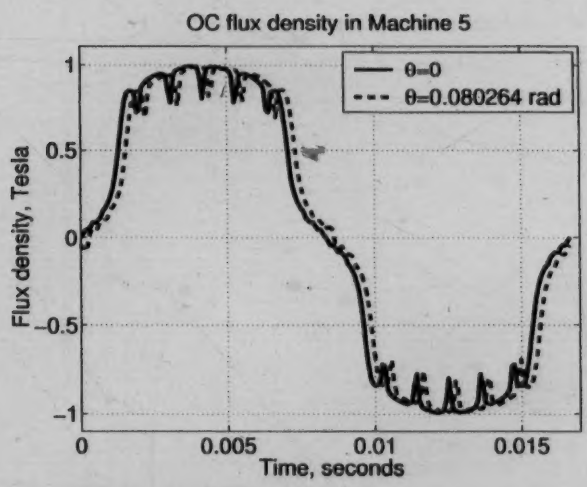

Figure 6.2: Air gap flux density in Machine 5, obtained by the model.

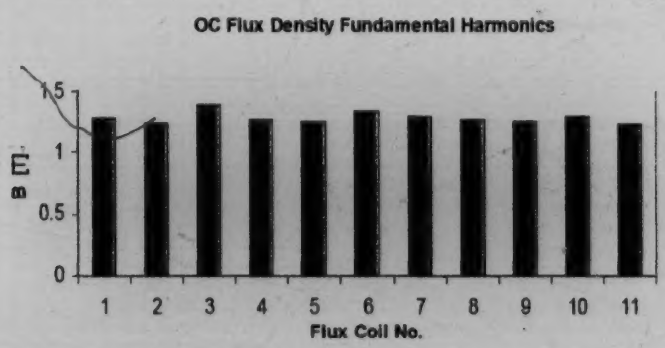

Figure 6.3: Measured variation in the magnitude of magnetic flux density fundamental with axial position for Machine 5.

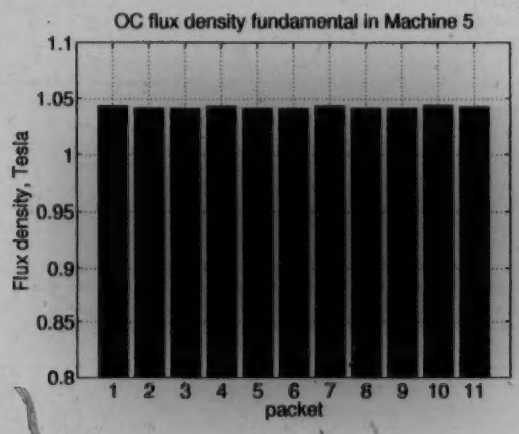

Figure 6.4: Simulated variation in the magnitude of magnetic flux density fundamental with axial position for Machine 5.

contact resistance of the armortisseur bars. The flux density waveform shown in Fig. 6.2 is obtained for the contact resistance $R_c = 0.01$ Ohm-m. The bar-to-iron resistance has been unknown in the tested machine.

6.2 Prediction of open circuit voltage

Open circuit voltage measurements are routinely done in generators. If the calculated open circuit voltage waveform is consistent with test, one may suggest that the air gap flux density has also been accurately predicted. All five machines are simulated, and the results are compared with available test and FEA results.

Table 6.2 provides data for the fundamental harmonic of the open circuit voltage. Results for the next most significant harmonics are shown in Figs. 6.5-6.9.

	Test, V	Model, V	FEA, V	Model vs. Test	FEA vs. Test
Machine 1	7911.8629	8135.9	7834.85	1.028	0.9903
Machine 2	7882.4	8005.8	7924.43	1.0157	1.0053
Machine 3	2417.536	2378.9	2428.02	0.9840	1.0043
Machine 4	7967.1	8197.3	7906.93	0.9924	0.9924
Machine 5	1352.5377	1337.0	1406.88	0.9885	1.0402

Table 6.2: RMS value of the phase voltage fundamental harmonic of the stator winding in the open circuit condition.

The developed analytical model predicts the open circuit voltage fundamental harmonic within 3 % in Machine 1, within 1.6 % in Machines 2, 3 and 5, and within 1 % in Machine 4. FEA results are within 1 % in Machines 1 and 4, within 0.5 % in Machines 2 and 3, and 4 % in Machine 5. Predictions of higher harmonics vary; while in general the results obtained from the model are close to test, the harmonics 9, 11 and 13 may differ from test data significantly, sometimes more than results obtained by FEA.

Magnitudes of certain voltage harmonics in skewed machines were found to depend on the contact bar-to-iron resistance of the armortisseur winding. Plots of the most significantly varying harmonics, such as 9th, 11-th, 13th, versus contact resistance in open circuit are shown in Fig. 6.10. One can see that the 11-th voltage harmonic varies from 40 to 580 volts in Machine 1, from 5 to 125 volts in Machine 5. The voltage harmonic data shown in Figs. 6.5-6.9 are obtained at the contact resistance $R_c = 0.01$ Ωm. The difference between the results obtained by test and simulation may be explained by the difference in contact resistance, which has been unknown in tested machines.

A numerical issue has been found to affect magnitudes of voltage harmonics obtained from the model. The designer defines minimum values to define the least magnitudes of harmonics to be used in the permeance model. However, the harmonic series only approximates a physical picture. When a

tolerance factor is very small, nonexistent higher-order harmonics, obtained through multiplication and summation, can accumulate, which may result in high magnitudes of non-existent high-frequency voltage harmonics.

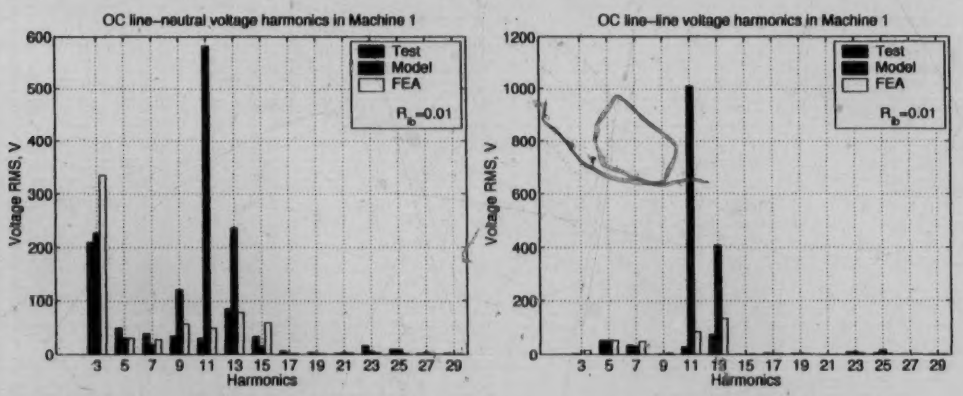

Figure 6.5: Comparison of test, the model, and FEA results in Machine 1.

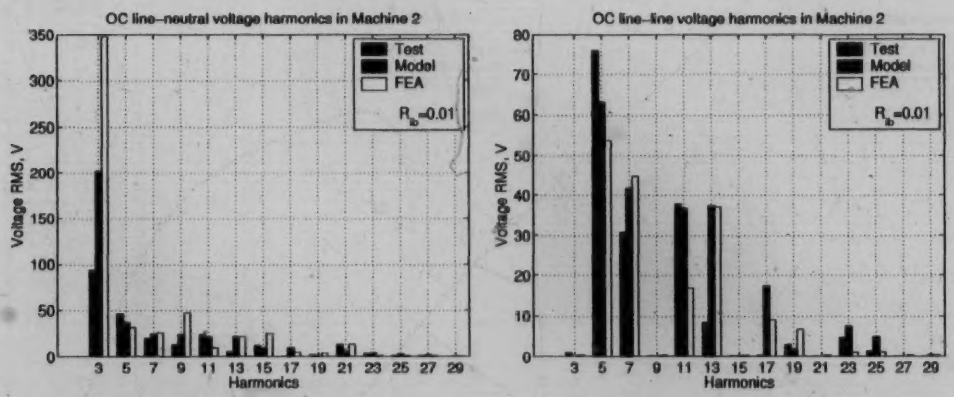

Figure 6.6: Comparison of test, the model, and FEA results in Machine 2.

6.3 Prediction of losses

Manufacturers of generators are required to supply loss data in open circuit and short circuit regimes. To verify the loss model, the calculated total loss in open and short circuit has been compared with measurements. The industrial sponsor provided open circuit and short circuit loss data, obtained by an electric input method and a separate drive method, for five machines with ratings shown in Table 6.1. The methods allow one to obtain sum of the stator core loss and the stray-load loss, if the armature (stator) copper loss is known [13]. The measured open circuit core loss is given in Table 6.3. The short

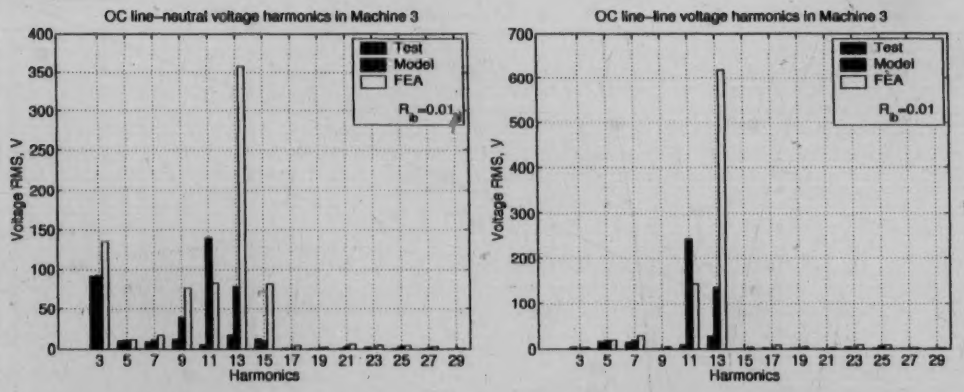

Figure 6.7: Comparison of test, the model, and FEA results in Machine 3.

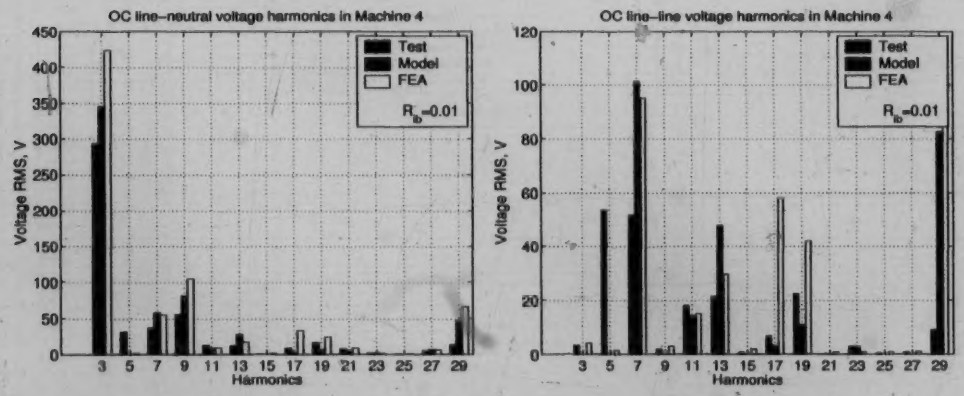

Figure 6.8: Comparison of test, the model, and FEA results in Machine 4.

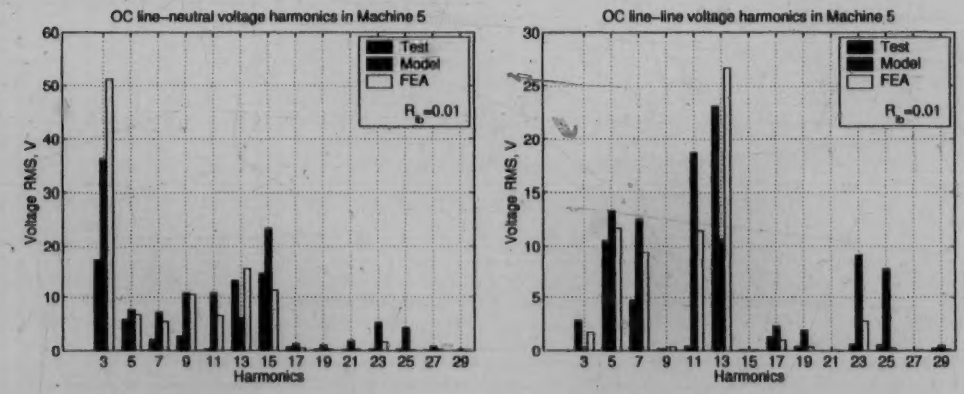

Figure 6.9: Comparison of test, the model, and FEA results in Machine 5.

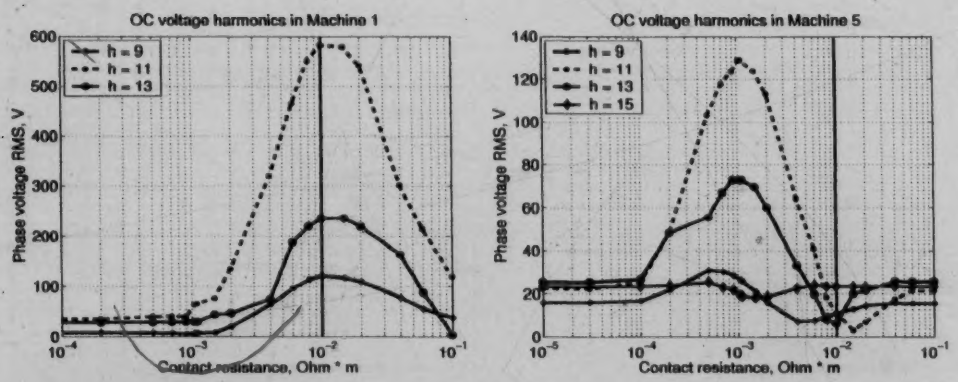

Figure 6.10: Phase voltage harmonics versus bar-to-iron resistance in Machine 1 and Machine 5 for the open circuit condition.

circuit core loss data as the difference of the measured short circuit loss and the estimated eddy current loss in the stator winding is given in Table 6.4.

The calculated total loss consists of the stator core loss as sum of eddy current, hysteresis and excess losses, the pole face loss, the ohmic loss in the bars of the damper winding, and the loss in the rotor iron due to inter-bar currents. The total loss does not include losses due to imperfections of the construction. The total loss is essentially sum of the stator core loss and the stray-load loss.

In skewed machines, the air gap flux density depends on the damper mmf formed by currents induced in bars of the armortisseur winding, so that losses should vary depending on the bar-to-iron resistance. Three skewed machines are simulated over a range of the bar-to-iron resistances. The losses in unskewed machines are found to not depend on the contact resistance, as is expected.

6.3.1 Open circuit losses

In open circuit, magnetic material saturates, and the relative permeability (the slope of the *B-H* curve of the material) decreases. The industrial sponsor provided a characteristic of variation of relative permeability with magnetic flux density in the rotor steel, as shown in Fig. 6.11 (left). The pole face loss heavily depends on the value of relative permeability; one can see from Fig. 6.11 (right) that in a range of the relative permeability from 50 to 1000, the pole loss increases by a factor of three.

The flux density in the rotor iron should normally be about 1.5-1.6 T. For comparison with test data, the rotor has been assumed more saturated, with a value $\mu_r = 50$ and flux density about 1.7 T.

Computations of losses in iron of the stator do not directly include permeability of the magnetic material (see Section 4.2.1). Physical constants to simulate the stator steel are chosen the same as the constants of steel used to

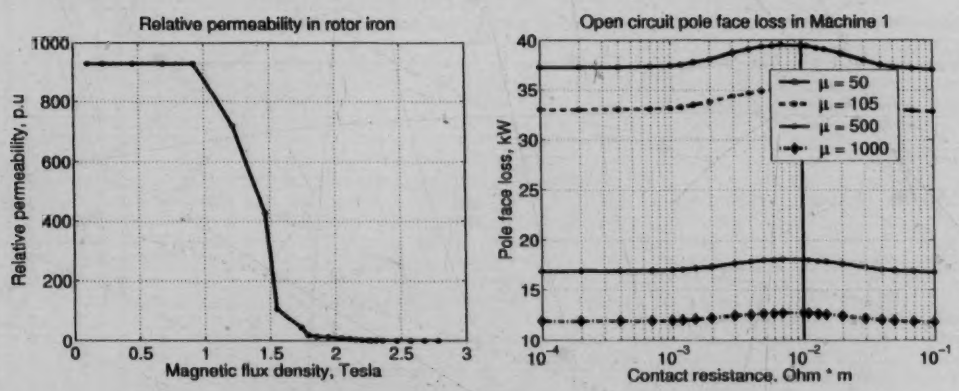
Relative permeability in rotor iron
Relative permeability, p.u
Magnetic flux density, Tesla
Open circuit pole face loss in Machine 1
Pole face loss, kW
Contact resistance, Ohm * m
μ = 50
μ = 105
μ = 500
μ = 1000

Figure 6.11: Relative permeability in rotor iron and pole face losses.

manufacture stators of Machines 1-5.

The calculated open circuit core losses for Machines 1-5 are shown in Table 6.3 and Figs. 6.12-6.13. It can be seen that the calculated losses are less than the test data. Reasons for the significant discrepancy may be variation of magnetic properties due to construction of the stator and rotor (gaps between adjacent segments in the stator, corrupted edges of laminations due to punching and burring) and existence of leakage fluxes (through holes in the pole body, air ducts in the stator, etc.), as not all leakage fluxes are accounted for by the model. The additional losses caused by constructional imperfections comprise from 40 % to 60 % of the fundamental core loss (loss at $f = 60$ Hz) in salient-pole synchronous machines [18].

	Skew	Model, kW	Test, kW
Machine 1	1	57 - 70	79.77
Machine 2	0	56.30	75.94/74.45
Machine 3	1	33.8 - 40.8	55.99
Machine 4	0	45.68	51.49
Machine 5	1	8.7 - 11.3	16.31

Table 6.3: Calculated and measured open circuit losses.

A vertical line at the contact resistance $R_c = 0.01\,\Omega$m in Figs. 6.12-6.13 intersects the loss curves. The point of intersection shows the loss corresponding to the open circuit voltage data shown in Table 6.2 and Figs. 6.5, 6.7 and 6.9 for respective machines.

6.3.2 Short circuit losses

In short circuit, there is no magnetic saturation, because the stator winding currents produce magnetic field opposing the main field, and the remainder of the flux does not saturate steel. The pole face loss has been simulated at a relative magnetic permeability of approximately 2000.

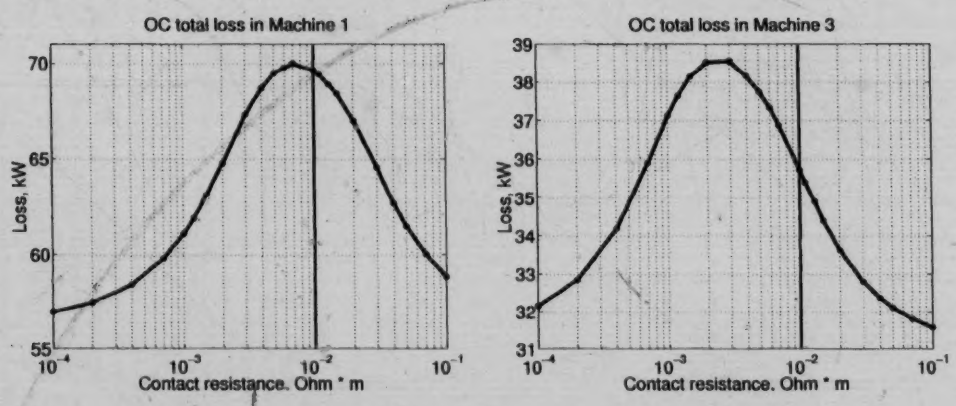

Figure 6.12: Open circuit total loss in Machines 1 and 3.

The calculated short circuit core losses for Machines 1-5 are shown in Table 6.4 and Figs. 6.14-6.15. The results of measurements are higher or within the range of the calculated losses. Assuming that additional losses due to constructional imperfections exist, they may be lower in the short circuit regime, because the magnitude of magnetic flux density in iron is lower. The relative permeability of the rotor steel in short circuit has been estimated; the obtained pole face loss may be different from the pole face loss in the real machines.

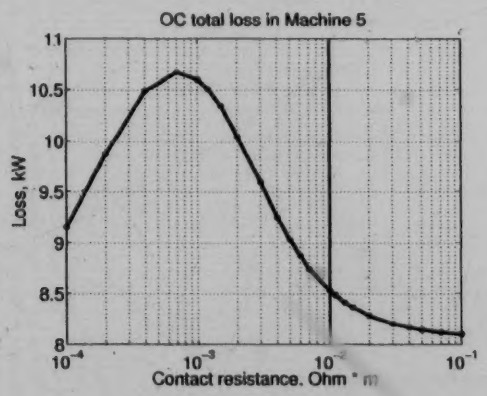

Figure 6.13: Open circuit total loss in Machine 5.

	Skew	Model, kW	Test, kW
Machine 1	1	16.5 - 24.5	34.98
Machine 2	0	20.2	21.51/19.72
Machine 3	1	14.7 - 20.7	22.23
Machine 4	0	10.03	16.35
Machine 5	1	2.8 - 4.05	3.52

Table 6.4: Calculated and measured short circuit losses.

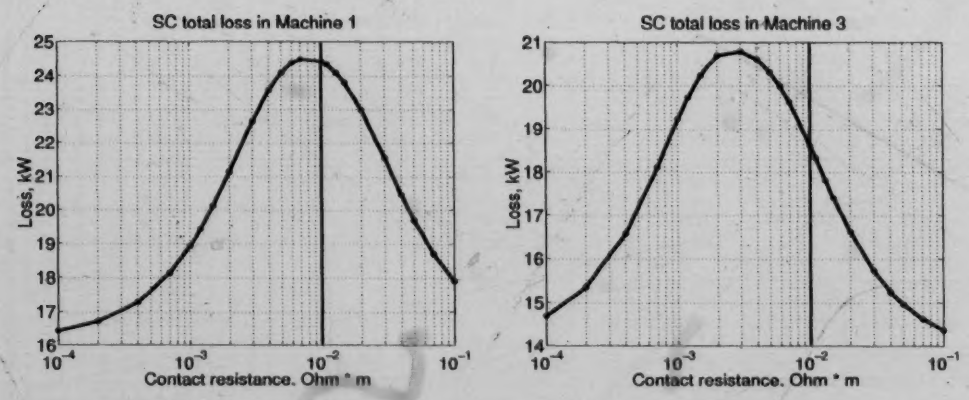

Figure 6.14: Short circuit total loss in Machines 1 and 3.

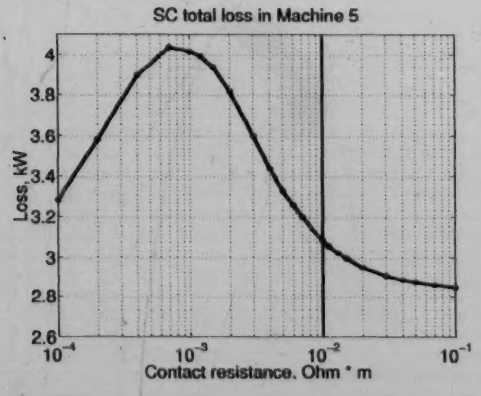

Figure 6.15: Short circuit total loss in Machine 5.

Chapter 7

Design studies

The previous chapter shows that skew and the contact resistance of the damper bars affect performance of a synchronous machine. In this chapter, power losses and damper bar currents are considered versus the two parameters. The contribution of each loss component to the total loss is quantified. The distribution of damper currents over the pole is obtained and discussed.

7.1 Losses

Investigations how skew and the interbar contact resistance affect losses are conducted in this chapter. Only losses that depend on skew are considered: loss in bars of the armortisseur winding, inter-bar loss, pole face loss and stator loss as sum of eddy current, hysteresis and excess losses. The total loss is defined as sum of these components; it does not include joule losses in the stator winding.

Machines 1, 3 and 5 (Table 6.1) are simulated for a range of contact resistances. Skew s is varied from zero to two slot pitches. The relative magnetic permeability of the pole iron is assumed $\mu_r = 105$ in open circuit, and $\mu_r \approx 2000$ in short circuit. Each of the four loss components and the total loss has been plotted. The losses in open circuit are shown in Figs. 7.1-7.9, in short circuit in Figs. 7.10-7.18.

Generally, losses are higher in open circuit than in short circuit. This is expected, because the magnetic flux can be high in open circuit, while it should be kept low to provide rated currents in the short-circuited winding. Losses depend of the magnetic flux or its time rate of change, so the loss magnitudes vary with variation of the flux. The qualitative behaviour of each loss component is discussed below.

In a range of low bar-to-iron resistances, the bar joule loss of the damper winding is little affected in either regime. This phenomenon occurs, because the loop currents are induced in the network at relatively high frequencies of several hundred hertz, so that the reactances of the network are much greater than the contact resistance. As the contact resistance increases and becomes

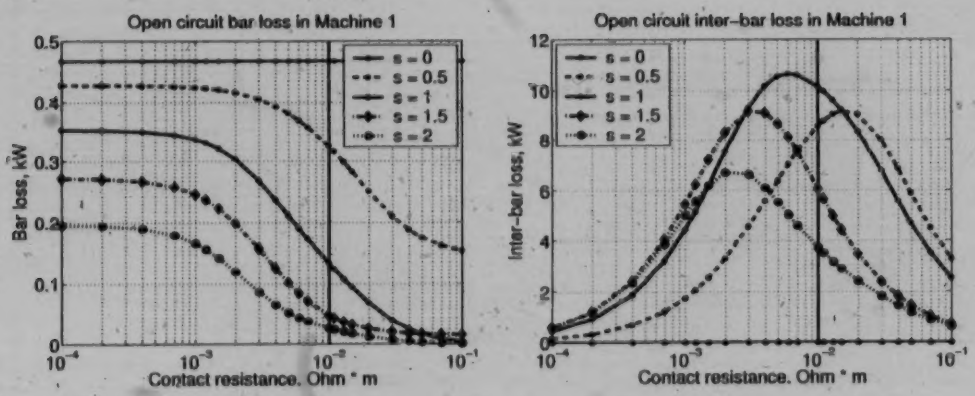
Open circuit bar loss in Machine 1
Bar loss, kW
Contact resistance. Ohm * m
s = 0
s = 0.5
s = 1
s = 1.5
s = 2
Open circuit inter–bar loss in Machine 1
Inter–bar loss, kW
Contact resistance. Ohm * m

Figure 7.1: OC bar-and inter-bar losses in Machine 1.

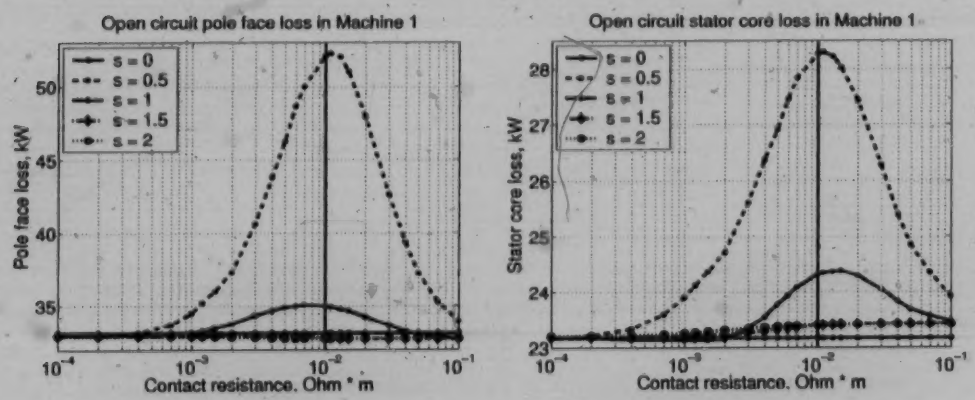
Open circuit pole face loss in Machine 1
Pole face loss, kW
Contact resistance. Ohm * m
s = 0
s = 0.5
s = 1
s = 1.5
s = 2
Open circuit stator core loss in Machine 1
Stator core loss, kW
Contact resistance. Ohm * m

Figure 7.2: OC pole face and stator losses in Machine 1.

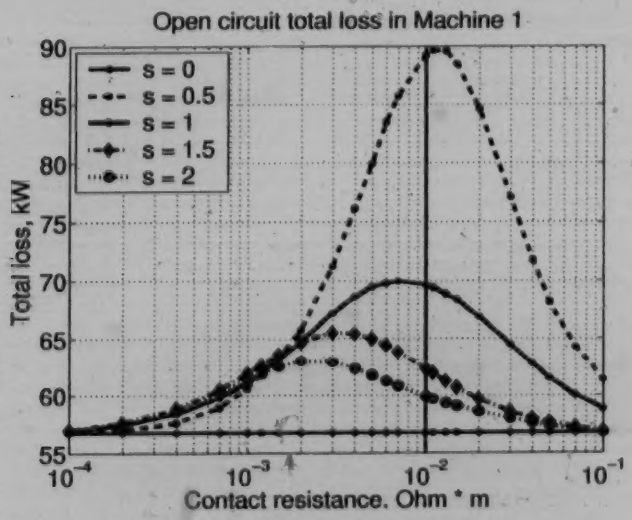

Figure 7.3: OC total loss in Machine 1.

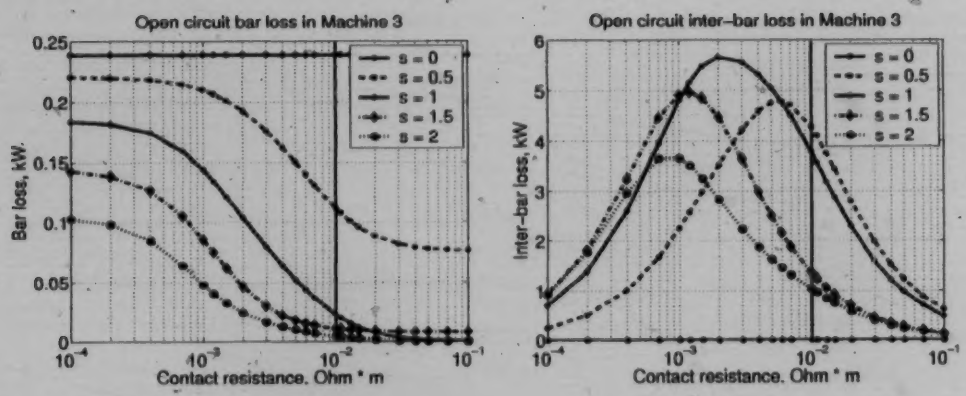
Open circuit bar loss in Machine 3
Bar loss, kW.
Contact resistance. Ohm * m
s = 0
s = 0.5
s = 1
s = 1.5
s = 2
Open circuit inter–bar loss in Machine 3
Inter–bar loss, kW
Contact resistance. Ohm * m

Figure 7.4: OC bar and inter-bar losses in Machine 3.

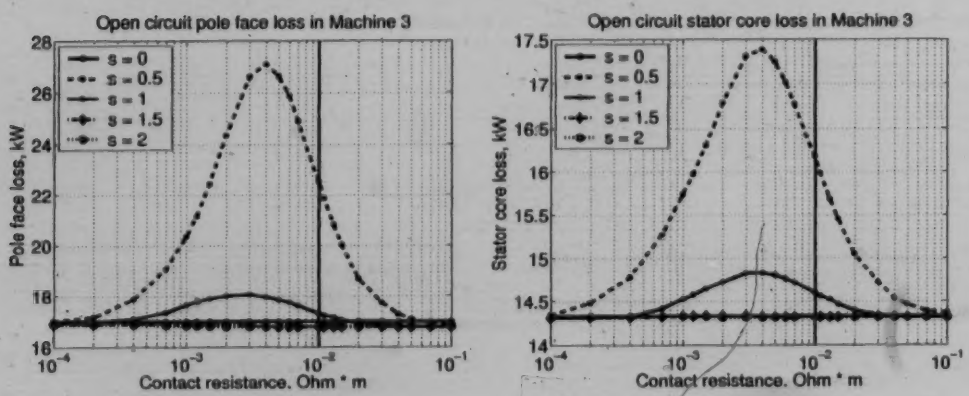
Open circuit pole face loss in Machine 3
Pole face loss, kW
Contact resistance. Ohm * m
s = 0
s = 0.5
s = 1
s = 1.5
s = 2
Open circuit stator core loss in Machine 3
Stator core loss, kW
Contact resistance. Ohm * m

Figure 7.5: OC pole face and stator losses in Machine 3.

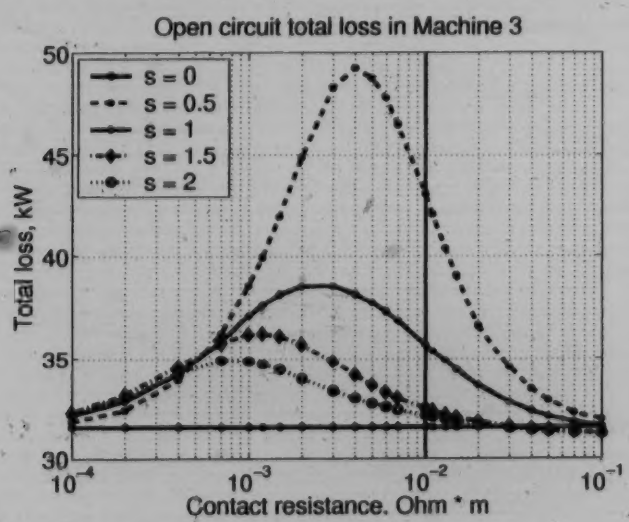

Figure 7.6: OC total loss in Machine 3.

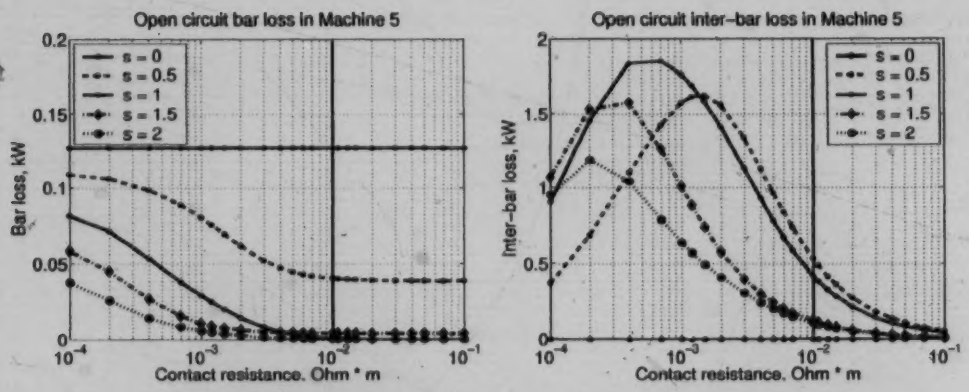
Open circuit bar loss in Machine 5
Bar loss, kW
Contact resistance. Ohm * m
s = 0
s = 0.5
s = 1
s = 1.5
s = 2
Open circuit inter−bar loss in Machine 5
Inter−bar loss, kW
Contact resistance. Ohm * m

Figure 7.7: OC bar and inter-bar losses in Machine 5.

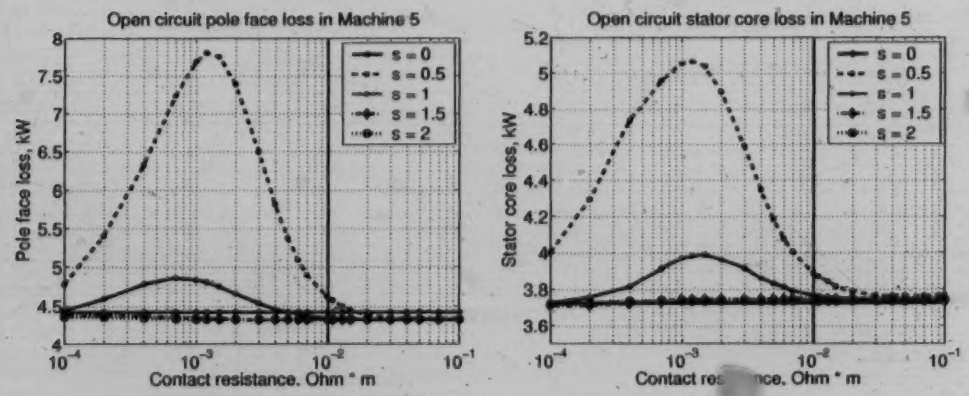
Open circuit pole face loss in Machine 5
Pole face loss, kW
Contact resistance. Ohm * m
s = 0
s = 0.5
s = 1
s = 1.5
s = 2
Open circuit stator core loss in Machine 5
Stator core loss, kW
Contact resistance. Ohm * m

Figure 7.8: OC pole face and stator losses in Machine 5.

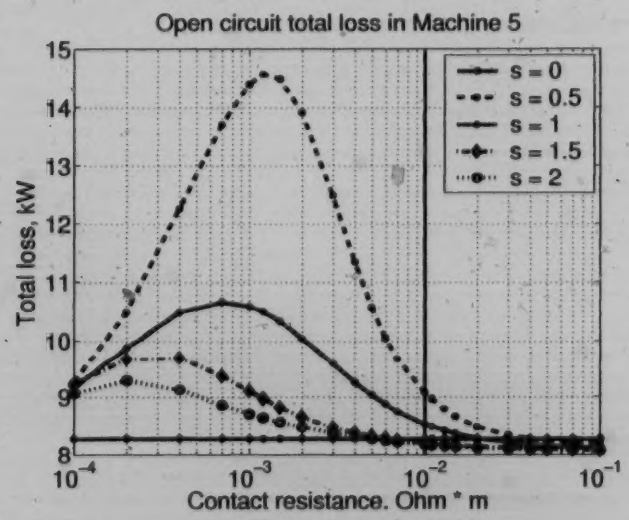

Figure 7.9: OC total loss in Machine 5.

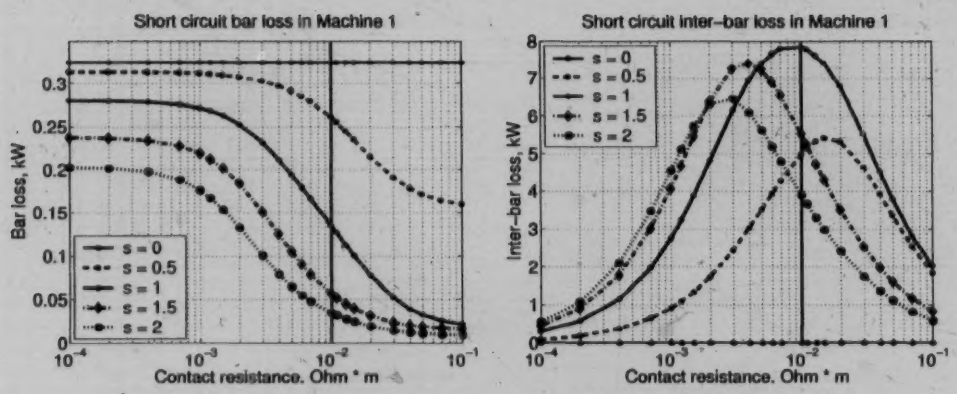
Short circuit bar loss in Machine 1
Bar loss, kW
Contact resistance, Ohm * m
s = 0
s = 0.5
s = 1
s = 1.5
s = 2
Short circuit inter-bar loss in Machine 1
Inter-bar loss, kW
Contact resistance, Ohm * m

Figure 7.10: SC bar and inter-bar losses in Machine 1.

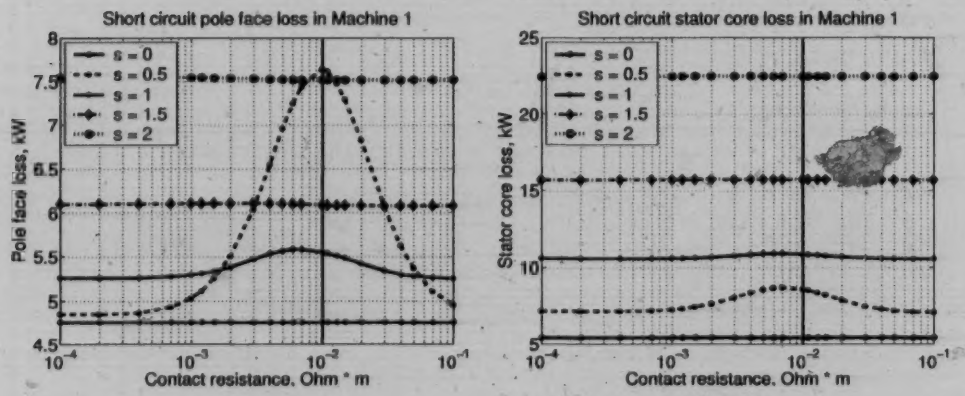
Short circuit pole face loss in Machine 1
Pole face loss, kW
Contact resistance, Ohm * m
s = 0
s = 0.5
s = 1
s = 1.5
s = 2
Short circuit stator core loss in Machine 1
Stator core loss, kW
Contact resistance, Ohm * m

Figure 7.11: SC pole face and stator losses in Machine 1.

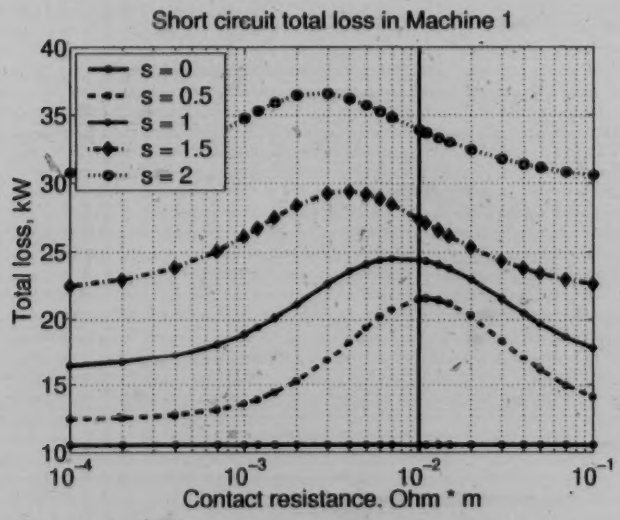

Figure 7.12: SC total loss in Machine 1.

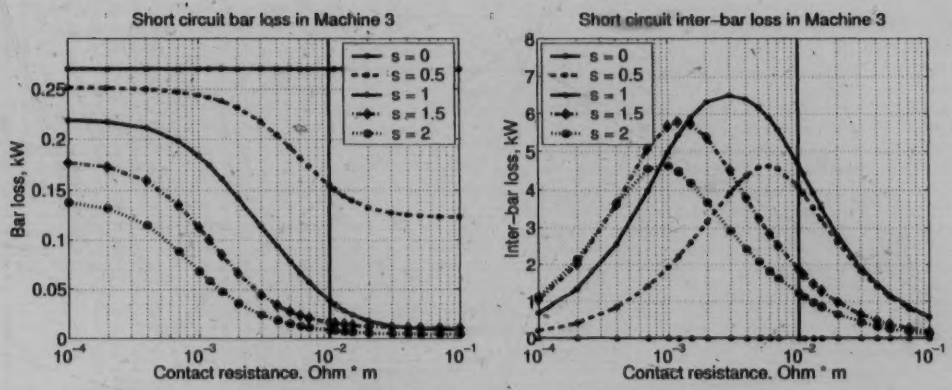
Short circuit bar loss in Machine 3
Bar loss, kW
Contact resistance. Ohm * m
s = 0
s = 0.5
s = 1
s = 1.5
s = 2
Short circuit inter–bar loss in Machine 3
Inter–bar loss, kW
Contact resistance. Ohm * m

Figure 7.13: SC bar and inter-bar losses in Machine 3.

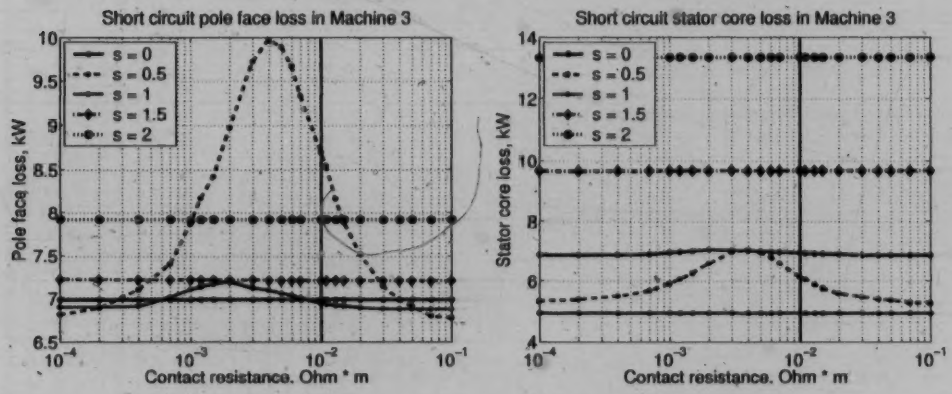
Short circuit pole face loss in Machine 3
Pole face loss, kW
Contact resistance. Ohm * m
s = 0
s = 0.5
s = 1
s = 1.5
s = 2
Short circuit stator core loss in Machine 3
Stator core loss, kW
Contact resistance. Ohm * m

Figure 7.14: SC pole face and stator losses in Machine 3.

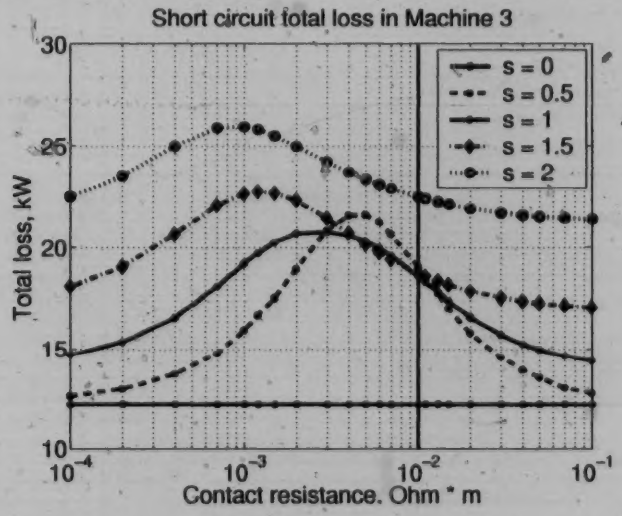

Figure 7.15: SC total loss in Machine 3.

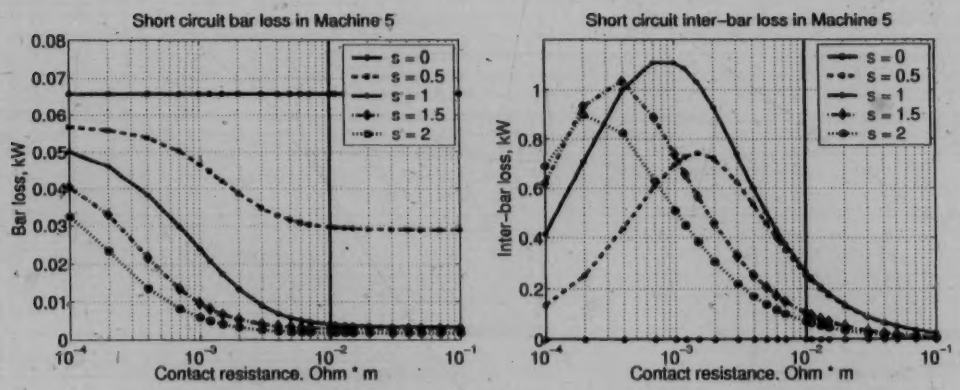
Short circuit bar loss in Machine 5
Bar loss, kW
Contact resistance. Ohm * m
s = 0
s = 0.5
s = 1
s = 1.5
s = 2
Short circuit inter–bar loss in Machine 5
Inter–bar loss, kW
Contact resistance. Ohm * m

Figure 7.16: SC bar and inter-bar losses in Machine 5.

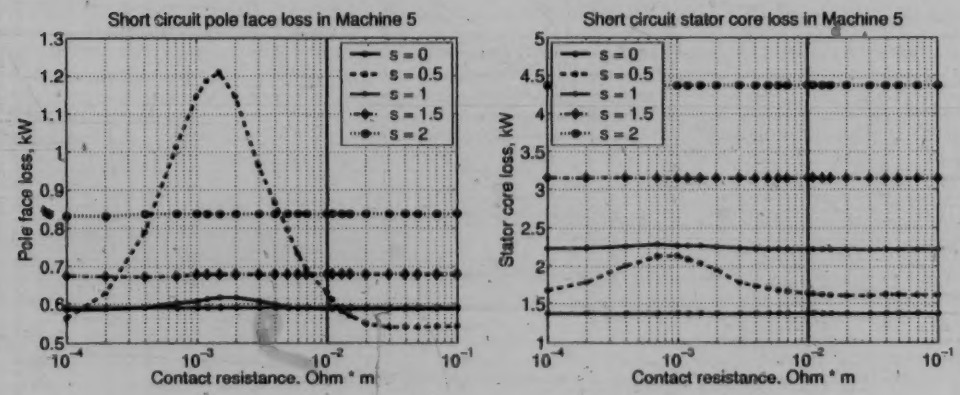
Short circuit pole face loss in Machine 5
Pole face loss, kW
Contact resistance. Ohm * m
s = 0
s = 0.5
s = 1
s = 1.5
s = 2
Short circuit stator core loss in Machine 5
Stator core loss, kW
Contact resistance. Ohm * m

Figure 7.17: SC pole face and stator losses in Machine 5.

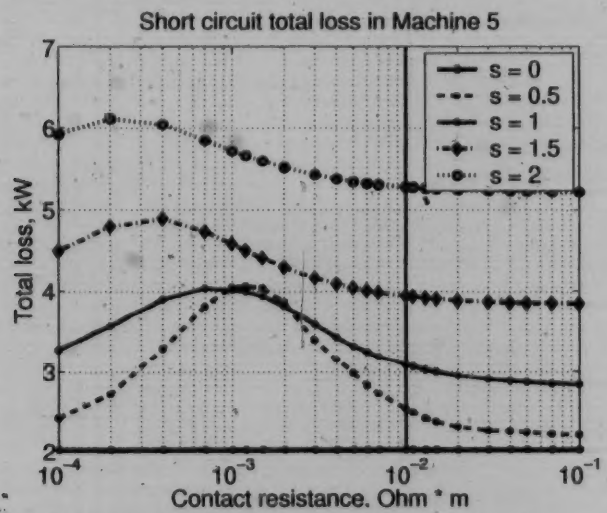

Figure 7.18: SC total loss in Machine 5.

comparable with the reactances, the loop currents and the ohmic loss in bars begin to fall. The ohmic loss component is small, compared to other loss components.

The interbar loss greatly depends on the contact resistance and contributes significantly to the total loss. Each interbar loss curve starts from zero at small values of the contact resistance, has a global maximum, and goes to zero at large values of the contact resistance, similarly to theoretical description of the interbar loss in squirrel-cage induction machines [10]. For the zero skew, the inter-bar loss is negligibly small. This is expected, as there are no inter-bar currents in unskewed machines (see Section 4.2.2; the loop emfs have the same phase shifts in the case of zero skew, so that they cancel each other over the interbar path).

The pole face loss and the stator core loss curves exhibit similar behaviour in either regime. The lowest, constant, curve corresponds to zero skew. The greatest variation of the losses occurs at a skew of a half slot pitch ($s = 0.5$), and a smaller variation occurs at the unity skew ($s = 1$). The losses corresponding to higher skew values are practically constant; they are grouped close to the zero skew curve in open circuit and spread more widely in short circuit. In open circuit, the pole face loss has been observed to be a dominant component of the total loss. The stator core loss is the largest component in short circuit.

Depending on the skew value, the global maximum of the total loss curve may be shifted over a range of contact resistance values. In open circuit, the global maximum appears to be lower, as skew increases. In short circuit, the global maximum generally increases with the increase of skew. The lowest total loss almost always corresponds to zero skew. The "next best" curve corresponds to $s = 2$ in open circuit and to $s = 0.5$ in short circuit.

7.2 Damper bar currents

In this section, distribution of current in the bars of the armortisseur winding on one pole is investigated. Each damper bar is partitioned in five slices. Current is calculated in the middle of each slice and assumed to be constant in the slice; skin effect is accounted for by an appropriate subroutine. Plots given in this section show surfaces, obtained by interpolation between calculated values of current. These surfaces might indicate trends, but they cannot be considered as showing accurate distribution of current.

It is clear from the damper circuit shown in Fig. 4.11 that current should be non-uniform along a bar. The distribution of current has been considered in open circuit and short circuit.

7.2.1 Bar currents in open circuit

In open circuit, the only source of the induced damper bar currents is slotting of the stator. A formula (2.5) gives orders of the slotting harmonics; it is repeated here for the reader's convenience:

$$n_s = k\frac{Ns}{p} \pm 1 = 2mq \pm 1 \tag{7.1}$$

The "plus" sign indicates that the harmonic rotates forward with respect to the rotor, and the "minus" sign indicates the backward rotation with respect to the rotor. For Machines 1, 3 and 5 the formula produces orders 11, 13, 23, 25 of slotting harmonics. Higher orders have not been considered due to lower bound constraint on the magnitude in the simulation tool.

Adding the speed of the slotting harmonic, calculated as $n_s \times 60$ Hz, to the rotor speed of 60 Hz, respecting the rotation in the same or opposite direction of the rotor's rotation, one can obtain temporal frequencies of 720 Hz (by the 11th and 13th harmonics) and 1440 Hz (by the 23rd and 25th harmonics). Thus in open circuit, current in the damper bars is induced at these two frequencies. Plots of the bar currents versus contact resistance are obtained for Machines 1 and 3 (Figs. 7.19-7.22).

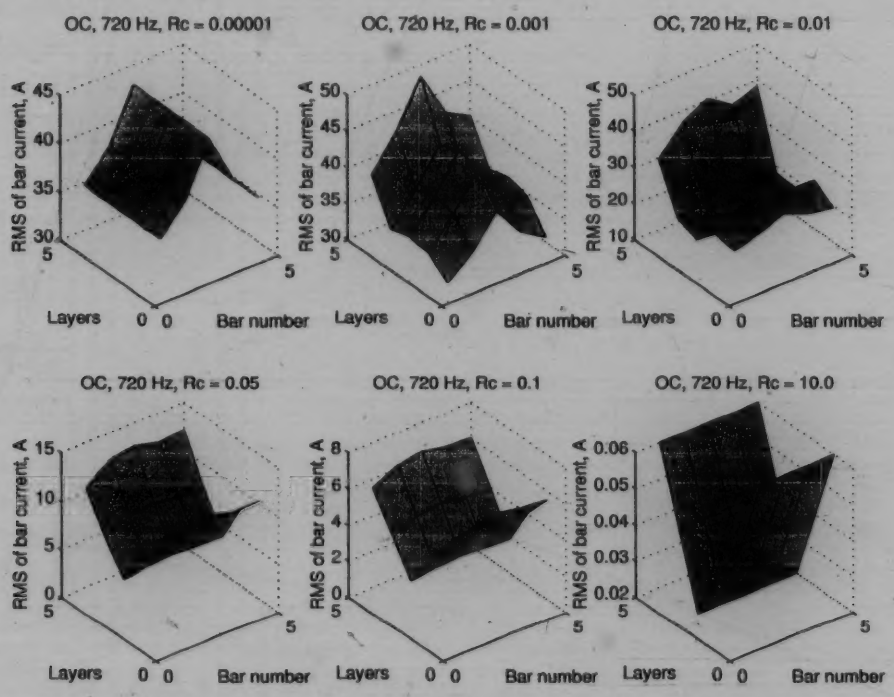
OC, 720 Hz, Rc = 0.00001
OC, 720 Hz, Rc = 0.001
OC, 720 Hz, Rc = 0.01
OC, 720 Hz, Rc = 0.05
OC, 720 Hz, Rc = 0.1
OC, 720 Hz, Rc = 10.0
RMS of bar current, A
Layers
Bar number

Figure 7.19: OC bar currents, 720 Hz, in Machine 1.

One can see that at low resistance values, the bar current distribution is almost symmetrical with respect to the pole axis. This is expected due to

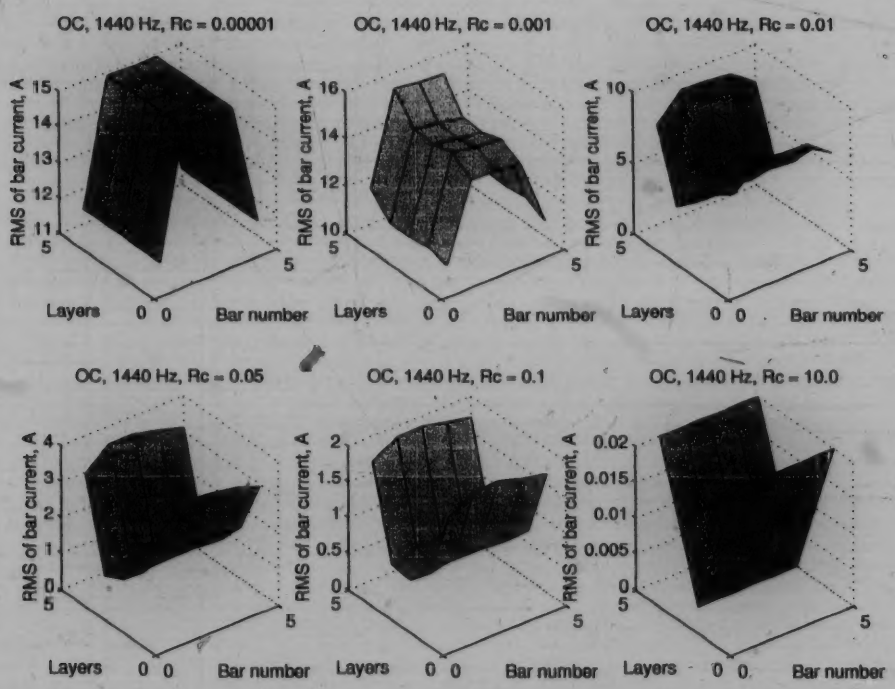
OC, 1440 Hz, Rc = 0.00001
OC, 1440 Hz, Rc = 0.001
OC, 1440 Hz, Rc = 0.01
OC, 1440 Hz, Rc = 0.05
OC, 1440 Hz, Rc = 0.1
OC, 1440 Hz, Rc = 10.0
RMS of bar current, A
Layers
Bar number

Figure 7.20: OC bar currents, 1440 Hz, in Machine 1.

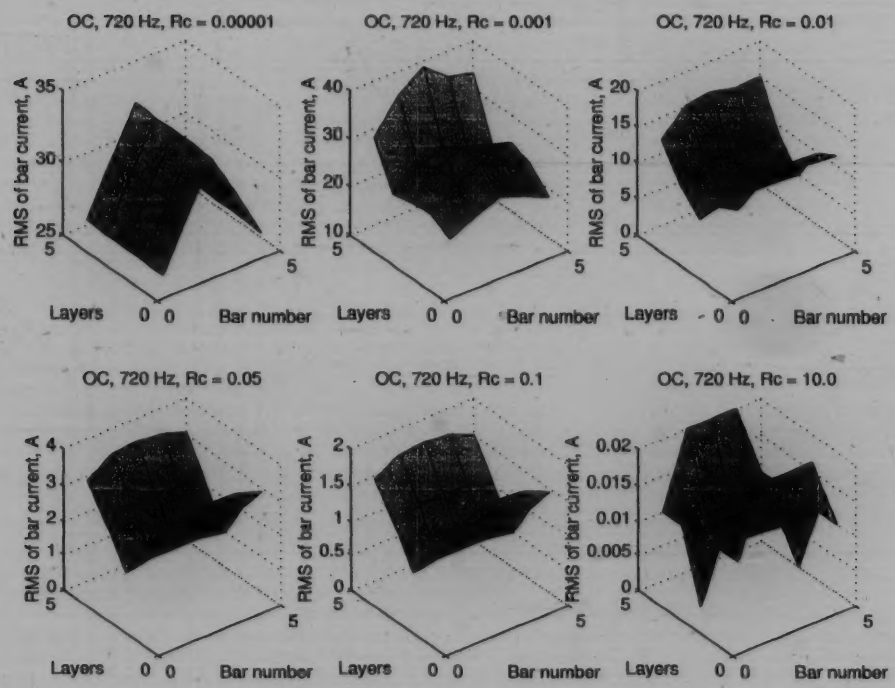
OC, 720 Hz, Rc = 0.00001
OC, 720 Hz, Rc = 0.001
OC, 720 Hz, Rc = 0.01
OC, 720 Hz, Rc = 0.05
OC, 720 Hz, Rc = 0.1
OC, 720 Hz, Rc = 10.0
RMS of bar current, A
Layers
Bar number

Figure 7.21: OC bar currents, 720 Hz, in Machine 3.

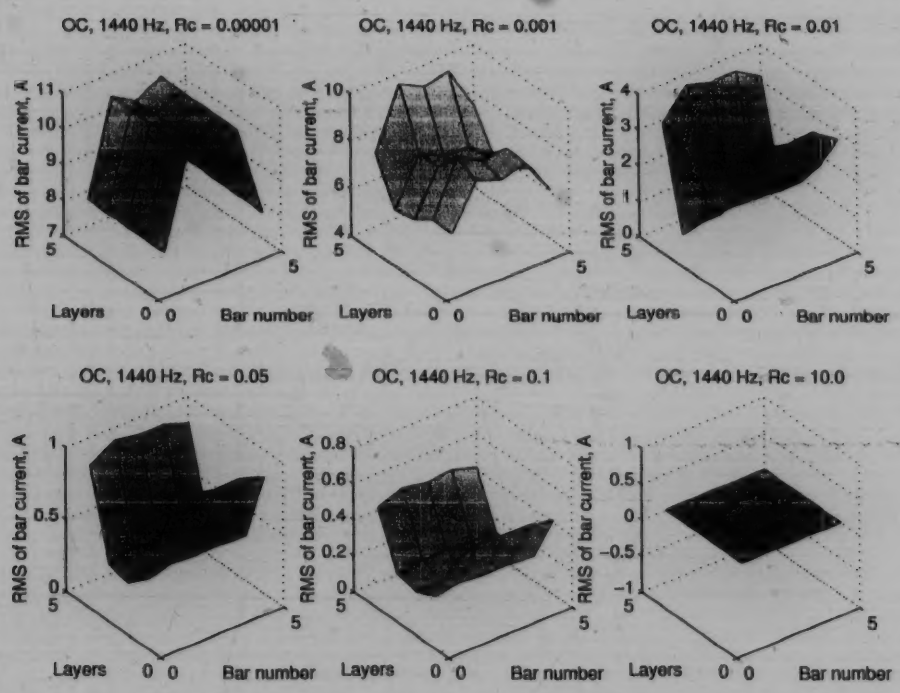
OC, 1440 Hz, Rc = 0.00001
OC, 1440 Hz, Rc = 0.001
OC, 1440 Hz, Rc = 0.01
OC, 1440 Hz, Rc = 0.05
OC, 1440 Hz, Rc = 0.1
OC, 1440 Hz, Rc = 10.0
RMS of bar current, A
Layers
Bar number

Figure 7.22: OC bar currents, 1440 Hz, in Machine 3.

the symmetrical pole shape and uniform field mmf. The current in the bars closer to the centre of the pole is higher, because the smaller air gap provides greater flux density. The bar current in the centre of the pole may be higher or lower than in adjacent bars, depending on whether the central bar faces the stator tooth or stator slot, which affects the air gap length. As the contact resistance increases, the axis of symmetry can rotate, as shown in Fig. 7.19 for $R_c = 0.01\,\Omega$m: it can be seen that similar current is induced at bar 1, slice 5, and bar 5, slice 1.

The bar current is determined as difference of ajacent loop currents, calculated from loop voltages and loop impedances. Loop voltage phase shift is affected by location of the loop in a skewed field. As a result, phase shifts of loop currents and the bar current between the loops are affected by skew. Depending on the phase shift, the bar current may be less or greater along the bar.

The plots at a low contact resistance of $0.0001\,\Omega$m show that the current is practically uniform along each bar. Consulting with Fig. 4.11 shows that if the bar-to-iron resistances are small, then the slices are not interconnected. The circuit becomes two-dimensional. Same loop voltage magnitudes, induced in the uniform skewed field produced by the field mmf and skewed air gap permeance, and similar loop impedance values (up to the end ring impedance) yield similar loop currents, so that the bar current has very close values in all slices.

The plots at high contact resistances, such as 10 Ωm, show that the bar current essentially becomes zero. This is also expected. Each loop contains two or four contact resistance components. If they are high, loop currents become zero and produce zero bar current.

It can be seen from the plots that a large contact resistance practically eliminates the bar current harmonics in open circuit.

7.2.2 Bar currents in short circuit

In short circuit, a rotating wave of the armature mmf is formed by currents of the three-phase armature winding. Space order harmonics of the armature mmf can be calculated by a formula

$$\nu = 2mc \pm 1 = 6c \pm 1 \tag{7.2}$$

where $m = 3$ is the number of phases of the armature winding, c is a non-negative integer. The "plus" sign indicates forward rotation with respect to the rotor, and the negative sign indicates backward rotation. The formula produces 1, 5, 7, 11, 13 space orders; higher-order harmonics are not considered. The armature mmf space harmonics produce the damper bar currents at frequencies 360, 720, 1080 and 1440 Hz.

Added to the field mmf in the short circuit regime, the armature mmf creates armature reaction. The resulting mmf and the magnetic field are low at one end of the pole and high at the other. The non-uniform distribution of the magnetic field causes large variation of current in the damper bars, as shown in Figs. 7.23-7.30. The plots are obtained at each frequency in Machines 1 and 3.

It can be seen that similarly to open circuit, the damper bar currents may increase by the fifth slice. The dependence of the bar current phase shift on skew can be further clarified for the short circuit regime. Because the field mmf and the armature mmf tend to cancel each other, the phase shift between them at one end of the machine is assumed to be 180°. For Machines 1 and 3 with six stator slots per pole pitch, a skew of one slot pitch provides a shift by 30° . That gives a phase shift of 150° between the field and armature mmf at the other end of the machine. The phasor summation of the mmf components at the other end of the machine is likely to produce a greater voltage in the fifth slice.

One can see that as the contact resistance increases, the bar current harmonics at 360 and 720 Hz diminish, but do not become zero at a large bar-to-iron resistance. The harmonics at 1080 and 1440 Hz decrease to zero.

7.2.3 Bar currents versus skew value

The magnitude of current in bars of the damper winding may depend on the skew value. Machines 1, 3 and 5 are simulated at the contact resistance 0.01 Ω

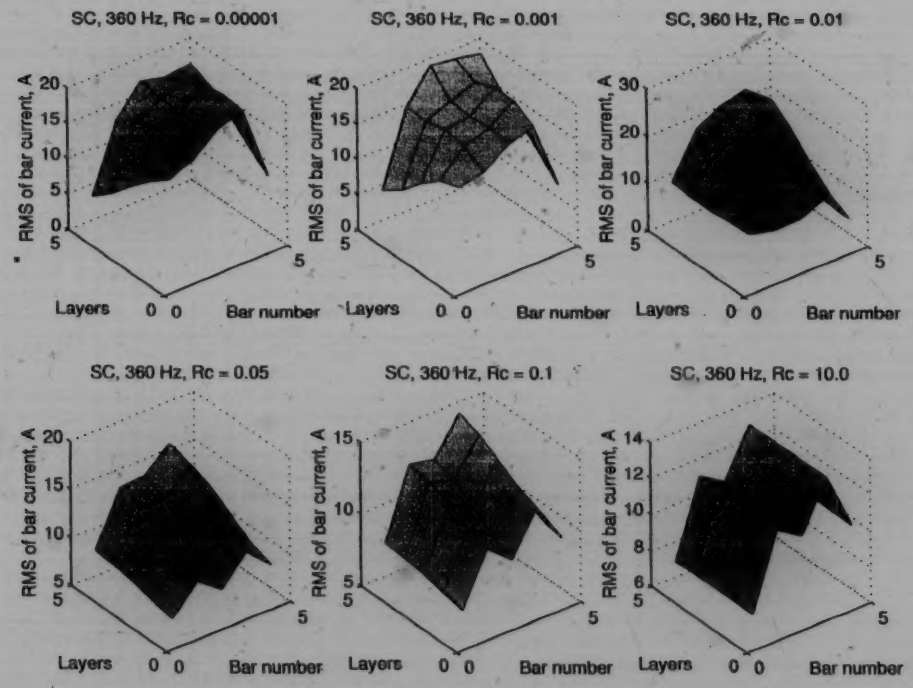
SC, 360 Hz, Rc = 0.00001
SC, 360 Hz, Rc = 0.001
SC, 360 Hz, Rc = 0.01
SC, 360 Hz, Rc = 0.05
SC, 360 Hz, Rc = 0.1
SC, 360 Hz, Rc = 10.0
RMS of bar current, A
Layers
Bar number

Figure 7.23: SC bar currents, 360 Hz, in Machine 1.

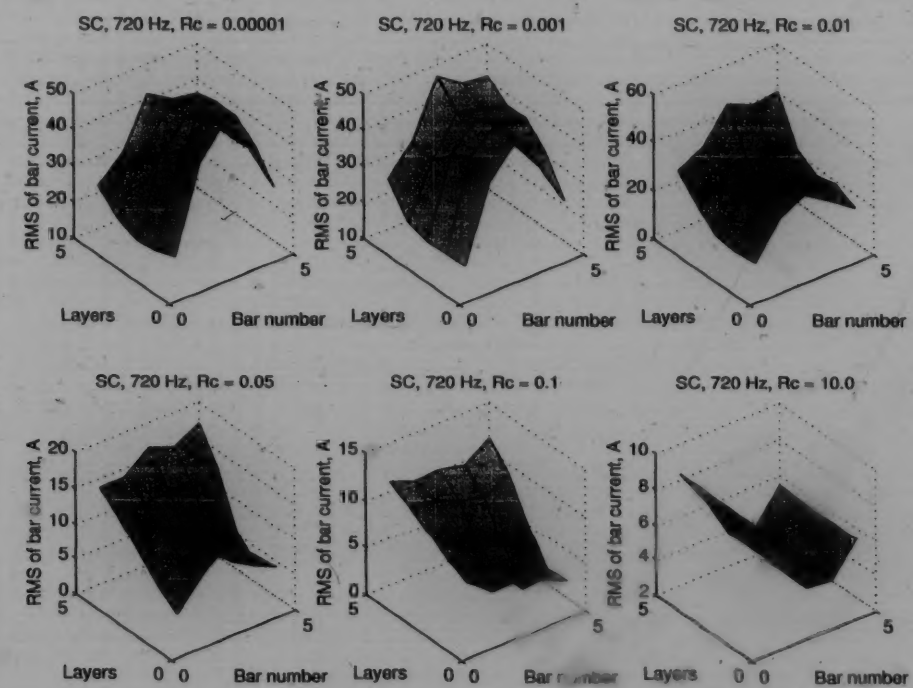
SC, 720 Hz, Rc = 0.00001
SC, 720 Hz, Rc = 0.001
SC, 720 Hz, Rc = 0.01
SC, 720 Hz, Rc = 0.05
SC, 720 Hz, Rc = 0.1
SC, 720 Hz, Rc = 10.0
RMS of bar current, A
Layers
Bar number

Figure 7.24: SC bar currents, 720 Hz in Machine 1.

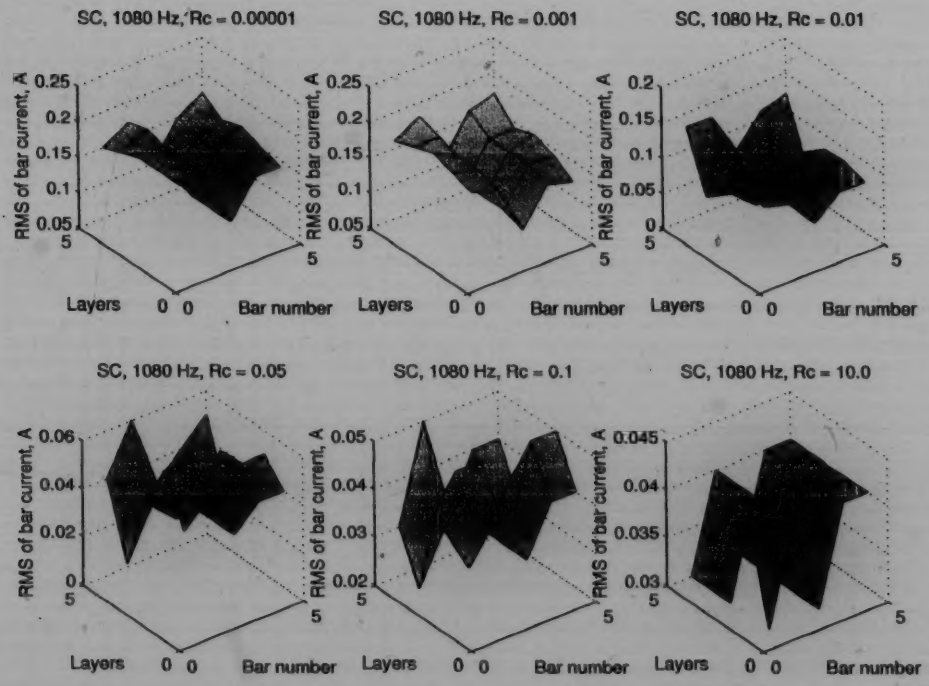
SC, 1080 Hz, Rc = 0.00001
SC, 1080 Hz, Rc = 0.001
SC, 1080 Hz, Rc = 0.01
SC, 1080 Hz, Rc = 0.05
SC, 1080 Hz, Rc = 0.1
SC, 1080 Hz, Rc = 10.0
RMS of bar current, A
Layers
Bar number

Figure 7.25: SC bar currents, 1080 Hz, in Machine 1.

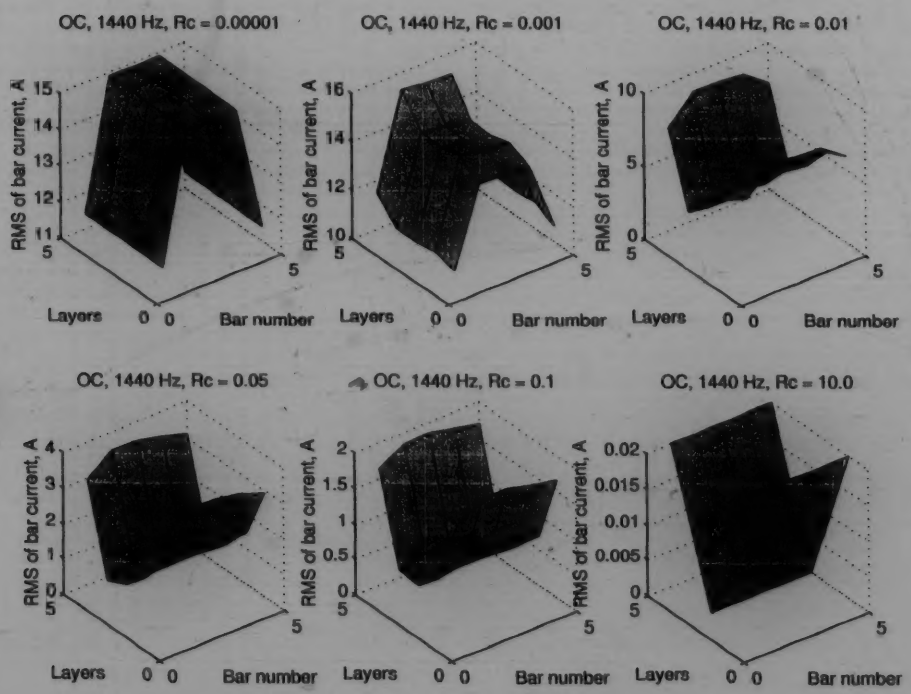
OC, 1440 Hz, Rc = 0.00001
OC, 1440 Hz, Rc = 0.001
OC, 1440 Hz, Rc = 0.01
OC, 1440 Hz, Rc = 0.05
OC, 1440 Hz, Rc = 0.1
OC, 1440 Hz, Rc = 10.0
RMS of bar current, A
Layers
Bar number

Figure 7.26: SC bar currents, 1440 Hz, in Machine 1.

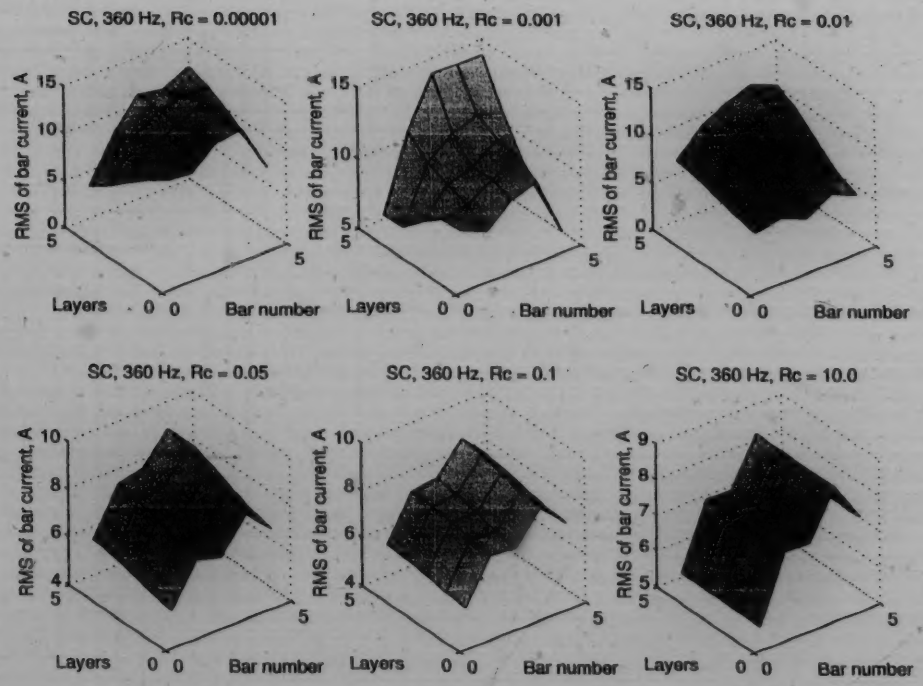
SC, 360 Hz, Rc = 0.00001
SC, 360 Hz, Rc = 0.001
SC, 360 Hz, Rc = 0.01
SC, 360 Hz, Rc = 0.05
SC, 360 Hz, Rc = 0.1
SC, 360 Hz, Rc = 10.0
RMS of bar current, A
Layers
Bar number

Figure 7.27: SC bar currents, 360 Hz, in Machine 3.

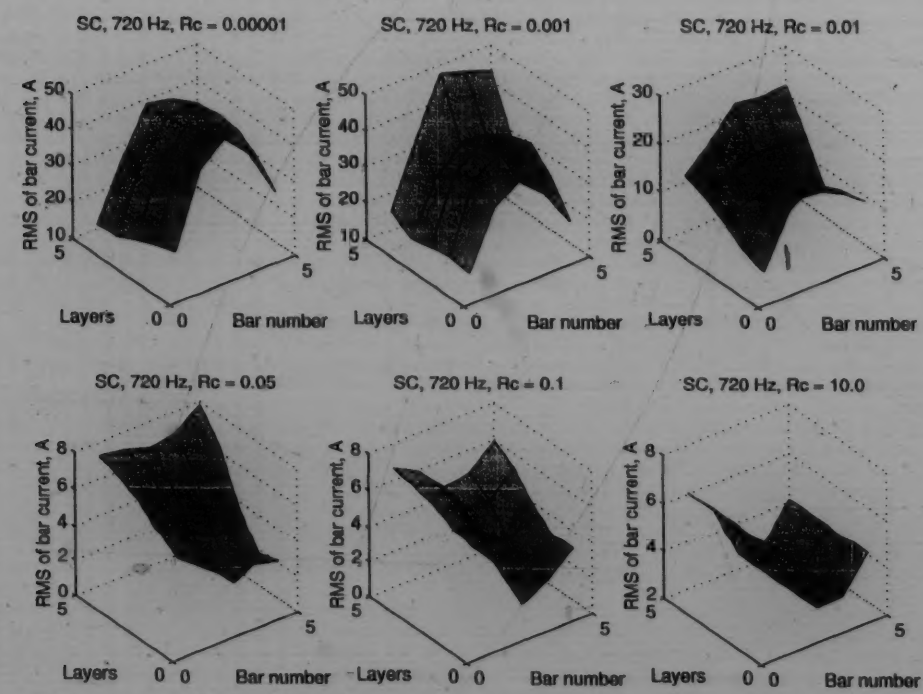
SC, 720 Hz, Rc = 0.00001
SC, 720 Hz, Rc = 0.001
SC, 720 Hz, Rc = 0.01
SC, 720 Hz, Rc = 0.05
SC, 720 Hz, Rc = 0.1
SC, 720 Hz, Rc = 10.0
RMS of bar current, A
Layers
Bar number

Figure 7.28: SC bar currents, 720 Hz, in Machine 3.

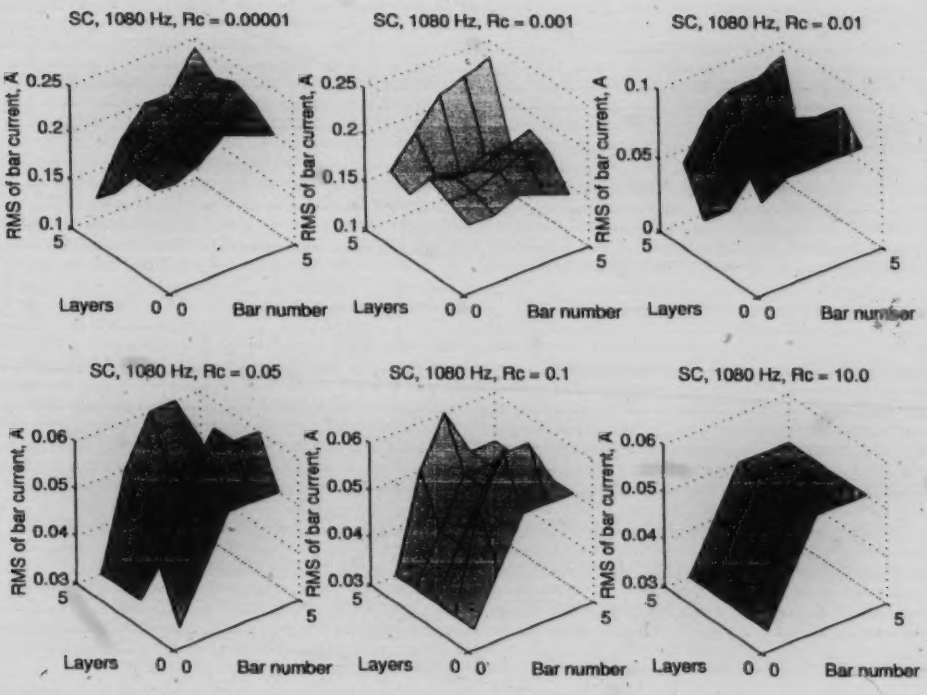
SC, 1080 Hz, Rc = 0.00001
SC, 1080 Hz, Rc = 0.001
SC, 1080 Hz, Rc = 0.01
SC, 1080 Hz, Rc = 0.05
SC, 1080 Hz, Rc = 0.1
SC, 1080 Hz, Rc = 10.0
RMS of bar current, A
Layers
Bar number

Figure 7.29: SC bar currents, 1080 Hz, in Machine 3.

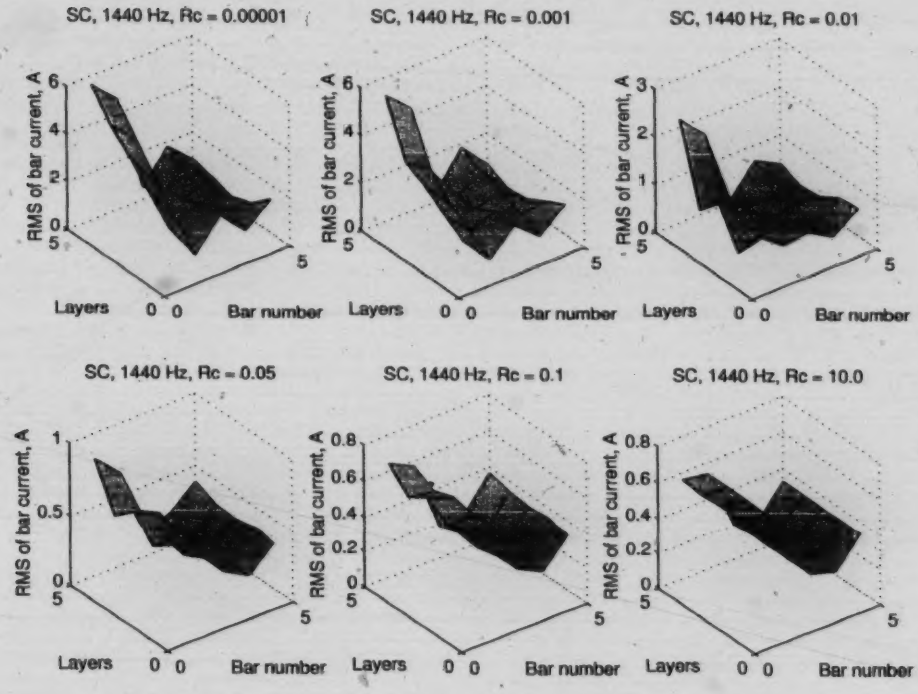
SC, 1440 Hz, Rc = 0.00001
SC, 1440 Hz, Rc = 0.001
SC, 1440 Hz, Rc = 0.01
SC, 1440 Hz, Rc = 0.05
SC, 1440 Hz, Rc = 0.1
SC, 1440 Hz, Rc = 10.0
RMS of bar current, A
Layers
Bar number

Figure 7.30: SC bar currents, 1440 Hz, in Machine 3.

m to obtain the bar current distribution. The most representative plots of the bar current versus skew in open and short circuit in Machines 1, 3 and 5 are shown in Figs. 7.31-7.35.

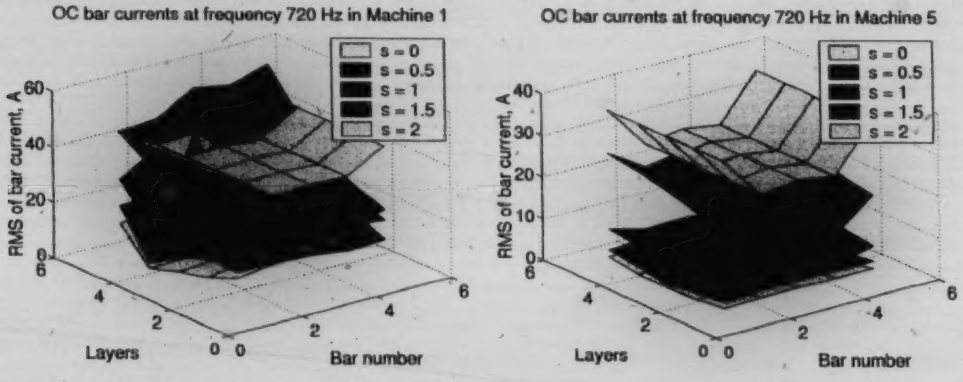

Figure 7.31: OC bar currents, 720 Hz, in Machine 1 and 5.

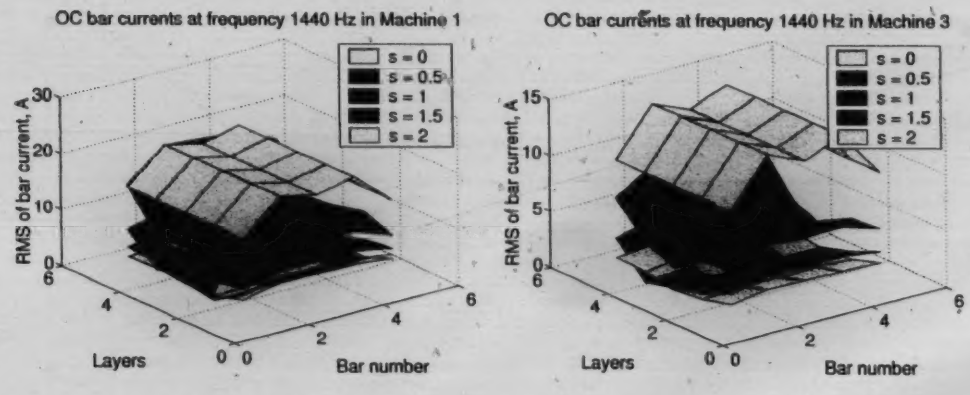

Figure 7.32: OC bar currents, 1440 Hz, in Machine 1 and 3.

One can see that in a non-skewed machine, the current has the same magnitude along the bar (no inter-bar currents), which is generally the highest, compared to currents at other skew values. When the skew is a half slot pitch ($s = 0.5$), the bar current in the fifth slice may be higher than in a non-skewed machine. As the skew increases, the bar current tends to be lower. The dependence exhibits the behaviour similar to the bar loss trend shown in Section 7.1.

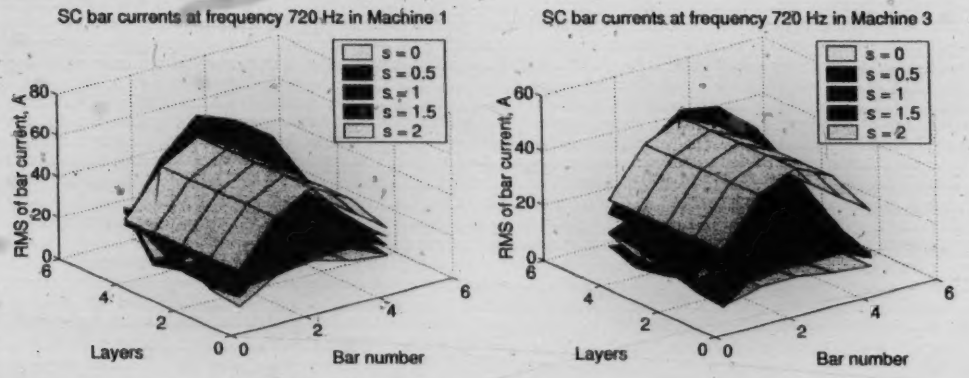
SC bar currents at frequency 720 Hz in Machine 1
SC bar currents at frequency 720 Hz in Machine 3
s = 0
s = 0.5
s = 1
s = 1.5
s = 2
RMS of bar current, A
Layers
Bar number

Figure 7.33: SC bar currents, 720 Hz, in Machine 1 and 3.

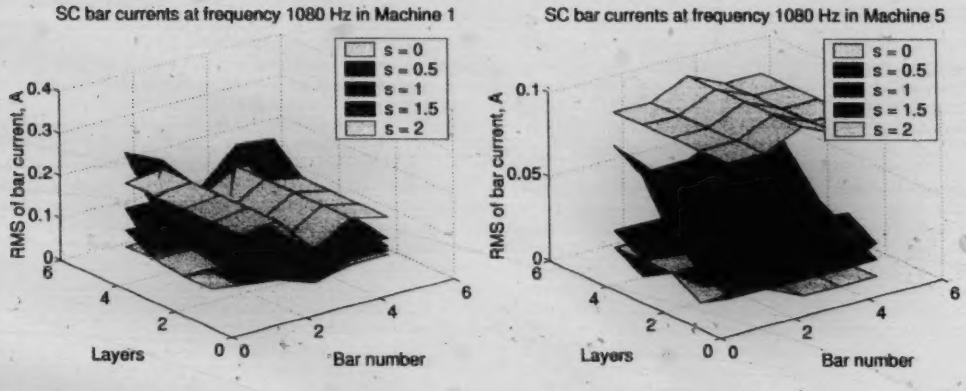
SC bar currents at frequency 1080 Hz in Machine 1
SC bar currents at frequency 1080 Hz in Machine 5
s = 0
s = 0.5
s = 1
s = 1.5
s = 2
RMS of bar current, A
Layers
Bar number

Figure 7.34: SC bar currents, 1080 Hz, in Machine 1 and 5.

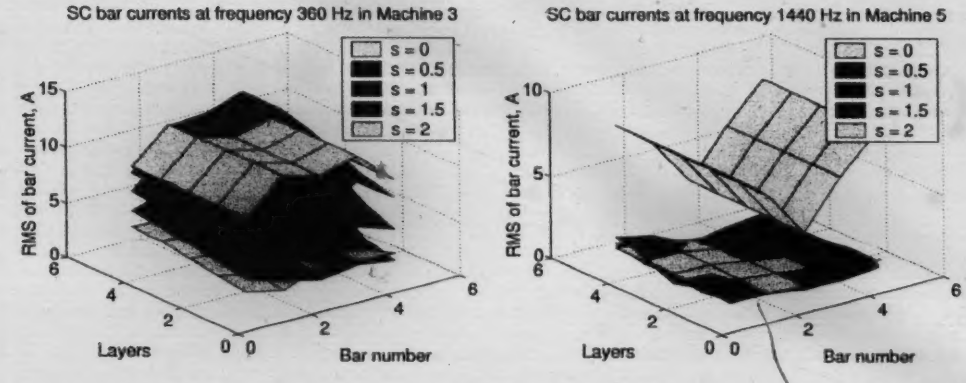
SC bar currents at frequency 360 Hz in Machine 3
SC bar currents at frequency 1440 Hz in Machine 5
s = 0
s = 0.5
s = 1
s = 1.5
s = 2
RMS of bar current, A
Layers
Bar number

Figure 7.35: SC bar currents, 360 and 1440 Hz, in Machine 3 and 5.

Chapter 8

Conclusion and recommendations for future work

Large synchronous machines have been a vital part of the electricity market. However, not much research has been done to study factors that impact performance of large synchronous machines with skewed stators. A multi-slice FEA that has a capability to analyze magnetostatic fields in these machines is excessively time-consuming, and so infeasible at the design stage.

This work is devoted to analytical modeling of magnetic fields and losses in a synchronous salient-pole machine with a skewed stator. Each loss component of interest is quantified, and this is the most significant result of the work. This result and other obtained results are discussed below.

A developed analytical model uses the permeance model and input information obtained by FEA of an unskewed synchronous machine to evaluate magnetic flux density in the air gap; it also employs a recent inter-bar current model to analyze inter-bar currents in the poles of a skewed synchronous machine. A simulation tool is developed on the basis of the analytical model. When possible, the model and the tool are verified by provided measurements.

The analytical model is used to investigate impact of skew and of the inter-bar resistance on the stator voltage in the open circuit condition and losses in the cases of open circuit and short circuit. Magnitudes of the voltage harmonics induced in the stator winding are found to depend on the contact resistance. Losses are also found to vary as the contact resistance varies; they decrease with the increase of skew in open circuit and increase with the increase of skew in short circuit. The open circuit losses appear to be much higher than the short circuit losses. With this information, a designer can make an optimal choice on the value of skew to minimize losses.

It is stressed that variation of the contact resistance makes the losses vary in a wide range. It is recommended that the contact resistance of the bars of the armortisseur winding is measured before the loss calculation. The bars can also be manufactured to be either very little or well insulated, to avoid a

range of the peak total loss.

It is also found that the pole face loss, a major loss component in the case of open circuit, varies in a wide range versus relative permeability of the pole. In calculations, the relative permeability of the pole is estimated for the open circuit and short circuit regimes. It is recommended that the material used to manufacture poles is studied to yield a possibly correct value of the relative permeability, to provide a better estimate of the pole face loss.

The analytical model is used to investigate distribution of currents in bars of the armortisseur winding over a pole versus contact resistance in open circuit and short circuit. It is found that the currents may increase from one end of the bar to the other, and that the increase of the contact resistance reduces the bar currents in magnitude. This data are not feasible for verification by measurements.

The following improvements are suggested to refine the analytical model. The bar-to-iron contact resistance is assumed constant along the damper bar and from bar to bar. It would be helpful to incorporate variation of the contact resistance along the bar length, and also from bar to bar. While leakage fluxes can be estimated empirically in an unskewed machine, they may be different in a skewed machine. Work in this area would improve evaluation of losses. Assumptions on flux fringing can be revisited to include leakage fluxes into calculation.

The developed simulation tool calculates magnetic fields and losses for a set of input data within several minutes. The stator voltage spectrum, obtained with the tool, is as accurate as FEA of a non-skewed machine or better. It can be concluded that the developed software is fast, accurate, and allows a design engineer to choose a suitable design at an early stage.

Bibliography

[1] Statistics Canada. Report on Energy Supply-demand in Canada: Table 1-1: Primary and secondary energy, natural units – Canada, July 9 2007. Available at: http://www.statcan.ca/english/freepub/57-003-XIE/2005000/tablesectionlist.htm.

[2] Statistics Canada. Report on Energy Supply-demand in Canada: Table 9: Primary electricity generation, July 9 2007. Available at: http://www.statcan.ca/english/freepub/57-003-XIE/2005000/tablesectionlist.htm.

[3] Energy Information Administration: Official Energy Statistics from the US Government. Table 6.3: World Net Electricity Generation by Type (Billion Kilowatthours), 2003. Available at: http://www.eia.doe.gov/emeu/iea/elec.html.

[4] WikipediA: The Free Encyclopedia. Available at: http://en.wikipedia.org/wiki/.

[5] REN21. Renewables Global Status Report 2006 Update. Paris: REN21 Secretariat and Washington, DC: Worldwatch Institute, 2006. Available at: http://www.ren21.net.

[6] Vincent Deltoro. *Basic electric machines.* Prentice-Hall, Inc., New Jersey, 1990.

[7] IEEE recommended practices and requirements for harmonic control in electrical power systems. The Institute of Electrical and Electronics Engineers, Inc. IEEE Std 519-1992.

[8] J.H. Walker. *Large synchronous machines: design, manufacture, and operation.* Oxford University Press, 1981.

[9] F.W. Carter. Magnetic noise in dynamo-electric machines. *Engineering*, pages 548–580, November 1932.

[10] A.M Odok. Stray-load losses and stray torques in induction machines. *Transactions AIEE, Part II*, 77:43–53, April 1958.

[11] A.V. Ivanov-Smolenskii. *Electricheskie mashiny.* Energia, Moskva, 1980.

[12] C.N. Glew. Stray load losses in induction motors: a challenge to academia. *Power Engineering Journal*, 12(1):27–32, February 1998.

[13] IEEE guide: Test procedures for synchronous machines. The Institute of Electrical and Electronics Engineers, Inc. IEEE Std 115-1995.

[14] R.R. Lawrence and H.E. Richards. *Principles of alternating-current machinery.* McGraw-Hill Book Company, Inc., New York, 4 edition, 1953.

[15] S.J. Chapman. *Electric machinery fundamentals.* The McGraw-Hill Companies, NY, 3rd edition, 1999.

[16] B.K Bose. *Modern power electronics and AC drives.* Prentice Hall, NJ, 2002.

[17] A.I. Voldek. *Electricheskie mashiny.* Energiya, Leningrad, 3rd edition, 1978.

[18] T.A. Lipo. *Introduction to AC machine design*, volume 1. Wisconsin Power Electronics Research Center, University of Wisconsin, 1996.

[19] B. Heller and V. Hamata. *Harmonic field effects in induction machines.* Elsevier Scientific Publishing Company, NY, 1977.

[20] A.M. Knight, H. Karmaker, and K. Weeber. Use of a permeance model to predict force harmonic components and damper winding effects in salient pole synchronous machines. *IEEE Transactions on Energy Conversion*, 17(4):478–484, December 2002.

[21] Quentin Graham. The m.m.f. wave of polyphase windings with special reference to sub-synchronous harmonics. *Winter Convention of A.I.E.E., NY*, pages 19–28, February 7-11 1927.

[22] N. Christofides. Origins of load losses in induction motors with cast aluminium rotors. *IEE Proceedings*, 112(12):2317–2332, December 1965.

[23] C.I. McClay. *Efficiency improvement of cage induction motors.* PhD thesis, University of Cambridge, 1996.

[24] S. Williamson and C.I. McClay. The effect of axial variations in saturation due to skew on induction motor equivalent-circuit parameters. *IEEE Transactions on Industry Applications*, 35(6):1323–1331, November/December 1999.

[25] S. Williamson and A.C. Smith. Equivalent circuits for cage induction motors with inter-bar currents. *IEE Proceedings - Electric Power Applications*, 149(3):173–183, May 2002.

[26] S. Williamson and A.C. Smith. Influence of interbar currents on the harmonic losses and skew in cage induction machines. *Power Electronics, Machines and Drives Conference*, (487):369–374, April 2002.

[27] S. Williamson and M.J. Robinson. Calculation of cage induction motor equivalent circuit parameters using finite elements. *IEE Proceedings, Part B*, 138(5):264–276, September 1991.

[28] D.G. Dorrell, T.J.E. Miller, and C.B. Rasmussen. Inter-bar currents in induction machines. *IEEE Trans. on Industry Applications*, 39(3):677–684, May/June 2003.

[29] S. Williamson, L.H. Lim, and A.C. Smith. Transient analysis of cage-induction motors using finite-elements. *IEEE Transactions on Magnetics*, 26(2):941–944, March 1990.

[30] A.M. Knight. *Analysis of line-start single-phase permanent magnet motors.* PhD thesis, University of Cambridge, 1998.

[31] S. Williamson and A.M. Knight. Performance of skewed single-phase line-start permenent magnet motors. *IEEE Transactions on Industry Applications*, 35(3):577–582, May/June 1999.

[32] A.M. Knight. A comparison of time-stepped finite element modelling methods for induction motor analysis. *Power Electronics, Machines and Drives Conference*, (487):375–380, 16–18 April 2002.

[33] A. Arkkio. *Analysis of induction motors based on the numerical solution of the magnetic field and circuit equations.* PhD thesis, Helsinki University of Technology, Helsinki, Finland, 1987.

[34] F. Piriou and A. Razek. Coupling of saturated electromagnetic systems to non-linear power electronic devices. *IEEE Transactions on Magnetics*, 24(1):274–277, January 1988.

[35] F. Piriou and A. Razek. A model for coupled magnetic-electric circuits in electric machines with skewed slots. *IEEE Transactions on Magnetics*, 26(2):1096–1100, March 1990.

[36] S.L. Ho, H.L. Li, and W.N. Fu. Inclusion of interbar currents in a network-field coupled time-stepping finite-element model of skewed-rotor induction motors. *IEEE Transactions on Magnetics*, 35(5):4218–4225, September 1999.

[37] A. Tenhunen and A. Arkkio. Modeling of induction machines with skewed rotor slots. *IEE Proceedings on Electric Power Applications*, 148(1):45–50, January 2001.

[38] C.I. McClay and S. Williamson. Influence of rotor skew on cage motor losses. *IEE Proceedings on Electric Power Applications*, 145(5):414–422, November/December 1998.

[39] C.I. McClay and S. Williamson. The variation of cage motor losses with skew. *IEEE Transactions on Industry Applications*, 36(6):1563–1570, November/December 2000.

[40] S. Williamson, T.J. Flack, and A. Volschenk. Representation of skew in time-stepped two-dimensional finite-element models of electrical machines. *IEEE Transactions on Industry Applications*, 31(5):1009–1015, September/October 1995.

[41] N. Stranges, R.D. Findlay, and J.H. Dymond. A comparison of two finite element methods for determining flux density polarization in induction motor cores. In *Proc. 1996 Canadian Conf. on Electrical and Computer Eng.*,, pages 943–946, Calgary, Alberta, Canada, May 26–29 1996.

[42] S. Toader. Combined analytical and finite element approach to the field harmonics and magnetic forces in synchronous machines. *Proceedings of the 11th International Conference Electrical Machines, Paris, France*, pages 583–588, 1994.

[43] F. Takase, T. Matsumura, and Y. Ueda. Use of permeance-based air-gap flux density analysis in the development of a synchronous generator model. *Electrical Engineering in Japan*, 113(4):101–111, 1993.

[44] A.M. Knight, H. Karmaker, and K. Weeber. Prediction of damper current windings and force harmonic components in large synchronous machines. *International Conference on Electrical Machines, Bruges, Belgium*, August 2002.

[45] J. Matsuki, T. Katagi, and T. Okada. Slot ripples in the damper windings of a salient-pole synchronous generator. *IEEE Transactions on Energy Conversion*, (1):126–132, March 1994.

[46] K. Nakamura, S. Fujio, and O. Ichinokura. A method for calculating iron loss of an sr motor based on reluctance network analysis and comparison of symmetric and asymmetric excitation. *IEEE Transactions on Magnetics*, 42(10):3440–3442, October 2006.

[47] A. Fonseca, Ch. Chillet, E. Atienza, A-L. Bui-Van, and J Bigeon. New modeling methodology for different pm motors for electricand hybrid vehicles. *IEEE International Electric Machines and Drives Conference*, 2001.

[48] H. Polinder, J.G. Slootweg, J.C. Compter, and M.J. Hoeijmakers. Modelling a linear pm motor including magnetic saturation. *International*

Conference on Power Electronics, Machines and Drives, pages 632–637, June 2002.

[49] C.B. Rasmussen and E. Ritchie. A magnetic equivalent circuit approach for predicting pm motor performance. *Industry Applications Conference, 32nd IAS Annual Meeting*, 1:10–17, October 1997.

[50] W. Shuting, L. Heming, L. Yonggang, and X. Zhaofeng. Reluctance network model of turbo-generator and its application – part 1: model. *Proceedings of the 8th International Conference on Electrical MAchines and Systems*, pages 1988–1993, September 2005.

[51] D. Petrichenko, M. Hecquet, P. Brochet, V. Kuznetsov, and D. Laloy. Design and simulation of turbo-alternators using a coupled permeance network model. *IEEE Transactions on Magnetics*, 42(4):1259–1262, April 2006.

[52] A.I Inkin. *Elektromagnitnye polya i parametry elektricheskih mashin.* Izdatelstvo YUKEA, Novosibirsk, 2002.

[53] L. Serrano-Iribarnegaray and J. MArtinez-Roman. Critical review of the analytical approaches accounting for interbar currents and experimental study of ageing in two-speed asynchronous motors for elevator drives. *IEE Proc. on Electric Power Applications*, 152(1), January 2005.

[54] N. Christofides. Determination of iron losses and torques in squirrel-cage induction motors. *IEE Proceedings*, 113(12):1995–2005, 1966.

[55] K. Oberretl. Eddy current losses in solid pole shoes of synchronous machines at no-load and on load. *IEEE Transactions on Power Apparatus and Systems*, PAS-91:152–159, 1972.

[56] H. Bondi and K.C. Mukherji. An analysis of tooth-ripple phenomena in smooth laminated pole-shoes. In *IEE Proceedings*, volume 104–105c, pages 349–356, 1957.

[57] W.J. Gibbs. *Conformal transformations in electrical engineering.* Chapman and Hall Ltd, London, 1958.

[58] F.W Carter. Note on air-gap and interpolar induction. *Journal of IEE*, XXIX:925–933, 1900.

[59] R.T. Coe and H.W. Taylor. Some problems in electrical machine design involving elliptic functions. *Phil.Mag.*, 6, 1928.

[60] Paul F. Byrd and Morris D. Friedman. *Handbook of elliptic integrals for engineers and scientists.* Springer-Verlag, New York, 2nd, revised edition, 1971.

[61] S. Williamson and Y.N. Feng. On the calculation of harmonic air-gap fields in machines with single-sided slotting. 2005.

[62] M. Markovic, M. Jufer, and Y. Perriard. An exact formula for "tooth-to-tooth" permeance. *IEEE Transactions on Magnetics*, 41(7):2295–2299, July 2005.

[63] Bernard Adkins and Ronald G. Harley. *The general theory of alternating current machines: Application to practical problems.* Chapman and Hall Ltd., London, 1975.

[64] M.A. Abdel-Halim and C.D. Manning. Modelling saturation of laminated salient-pole synchronous machines. *IEE Proceedings Part B*, 134(4):215–223, July 1987.

[65] A.M. El-Serafi and A.S. Abdallah. Saturated synchronous reactances of synchronous machines. *IEEE Transactions on Energy Conversion*, 7(3):570–579, September 1992.

[66] A.M. El-Serafi and J. Wu. Determination of the parameters representing the cross-magnetizing effect in saturated synchronous machines. *IEEE Transactions on Energy Conversion*, 1993.

[67] S.H. Minnich, R.P. Schultz, D.H. Baker, R.G. Farmer, D.K. Sharma, and J.H. Fish. Saturation functions for synchronous generators from finite elements. *IEEE Transactions on Energy Conversion*, EC-2(4):680–687, December 1987.

[68] S.J. Salon. *Finite element analysis of electrical machines.* The Kluwer International Series in Engineering and Computer Science. Kluwer Academic Publishers, Boston/London/Dordrecht, 3rd edition, 2000.

[69] O. Drubel and R. Stoll. Tooth ripple losses in salient pole synchronous machines. *International Conference IEMD'99*, pages 649–652, 9–12 May 1999.

[70] O. Drubel and R. Stoll. Comparison between analytical and numerical methods of calculating tooth ripple losses in salient pole synchronous machines. *IEEE Transactions on Energy Conversion*, 16(1):61–67, March 2001.

[71] M.V.K Chari. *Numerical methods in electromagnetism.* Academic Press, San Diego, 2000.

[72] S.R.H. Hoole. *Computer aided analysis and design of electromagnetic devices.* Elsevier, New York, 1989.

[73] R.D. Findlay, N. Stranges, and D.K. MacKay. Losses due to rotational flux in three phase induction motors. *IEEE Transactions on Energy Conversion*, 9(3):543–548, September 1994.

[74] P. Dular, J. Gyselinck, C. Geuzaine, N. Sadowski, and J.P.A. Bastos. A 3-d magnetic vector potential formulation taking eddy currents in lamination stacks into account. *IEEE Transactions on Magnetics*, 39(3):1424–1427, May 2003.

[75] Y. Liu, A. Bondeson, R. Bergstrom, M.G. Larson, and K. Samuelsson. Edge element computations of eddy currents in laminated materials. *IEEE Transactions on Magnetics*, 39(3):1758–1765, May 2003.

[76] S.L. Ho, W.N. Fu, and H.C Wong. Generation and rotation of 3-d finite element mesh for skewed rotor induction motors using extrusion technique. *IEEE Transactions on Magnetics*, 35(3):1266–1268, May 1999.

[77] S.L. Ho, W.N. Fu, and H.C Wong. Solution of a 3-d complex finite element model of skewed rotor induction motors using an iterative method. *IEEE Transactions on Energy Conversion*, 14(4):1247–1252, December 1999.

[78] Langru Li and Youqing Xiang. Finite element computation of 3-d nonlinear magnetic field in claw-pole electric machine using two scalar potentials, hybrid elements and automatic mesh generation. *IEEE Transactions on Magnetics*, 26(2):371–374, March 1990.

[79] Gordon R. Slemon. *Electrical machines and drives.* Addison-Wesley Series in Electrical Engineering. Addison-Wesley Publishing Company, Inc., NY, 1992.

[80] K Atallah, Z.Q. Zhu, and D Howe. The prediction of iron losses in brushless permanent magnet dc motors. In *International Conference Electrical Machines*, pages 814–818, UMIST(UK), 1992.

[81] M.A. Mueller, S. Williamson, T.J. Flack, K. Atallah, B. Baholo, D. Howe, and P.H. Mellor. Calculation of iron losses from time-stepped finite-element models of cage induction machines. *IEE Electrical Machines and Drives Conference*, (412):88–92, 11–13 September 1995.

[82] J. Gyselinck, L. Vandelvelde, J. Melkebeek, P. Dular, F. Henrotte, and W. Legros. Calculation of eddy currents and associated losses in electrical steel laminations. *IEEE Transactions on Magnetics*, 35(3):1191–1194, May 1999.

[83] C. Mi, G.R. Slemon, and R. Bonert. Modeling of iron losses of permanent-magnet synchronous motors. *IEEE Transactions on Industry Applications*, 39(3):734–742, May/June 2003.

[84] J. D. Lavers, P.P. Biringer, and H Hollitscher. A simple method of estimating the minor loop hysteresis loss in thin laminations. *IEEE Transactions on Magnetics*, Mag-14(5):386–388, September 1978.

[85] Gordon R. Slemon and Xian Liu. Core losses in permanent magnet motors. *IEEE Transactions on Magnetics*, 26(5):1653–1655, September 1990.

[86] S. McKee and A. Simpson. Ferroresonance and Preisach theory. In *Warning! Ferroresonance can damage your plant.* IEE Colloquium, November 12 1997. Digest No:1997/349.

[87] L.R. Dupre, R. Van Keer, and J.A.A. Melkebeek. Modelling and identification of iron losses in nonoriented steel laminations using preisach theory. *IEE Proceedings – Electric Power Applications*, 144(4):227–234, July 1997.

[88] S.Y.R. Hui and J. Zhu. Numerical modeling and simulation of hysteresis effects in magnetic cores using transmission-line modelling and the preisach theory. *IEE Proceeedings - Electric Power Applications*, 142(1):57–62, January 1995.

[89] Luc R. Dupre, Roger Van Keer, and Jan A.A. Melkebeek. An iron loss model for electrical machines using the preisach theory. *IEEE Transactions on Magnetics*, 1997.

[90] L.R. Dupre, G. Bertotti, and J.A.A. Melkebeek. Dynamic Preisach model and energy dissipation in soft magnetic materials. *IEEE Transactions on Magnetics*, 34(4):1168–1170, July 1998. Part 1.

[91] N. Stranges and R.D. Findlay. Measurement of rotational iron losses in electrical sheet. *IEEE Transactions on Magnetics*, 36(5):3457–3459, September 2000.

[92] N. Stranges and R.D. Findlay. Methods for predicting rotational iron losses in three phase induction motor stators. *IEEE Transactions on Magnetics*, 36(5):3112–3114, September 2000.

[93] G. Bertotti, A. Boglietti, M. Chiampi, D. Chiarabaglio, F. Fiorillo, and M. Lazzari. An improved estimation of iron losses in rotating electrical machines. *IEEE Transactions on Magnetics*, 27(6):5007–5009, November 1991.

[94] S.G. Troitskaia. Optimization of induction motor powered by variable speed drive. Master's thesis, University of Illinois at Urbana-Champaign, August 1999.

[95] H.C. Karmaker. Practical design applications of time-stepping finite element analysis to salient-pole synchronous machines. In *Proceedings IEEE PES Winter meeting*, pages 344–347, 2000.

[96] H.C. Karmaker. Time-stepping finite element analysis of starting performance of large salient-pole synchronous machines. *IEEE International Electric Machines and Drives Conference*, 3:1565–1570, June 2003.

[97] V. Subba Rao and O.I. Butler. Stray losses of polyphase cage-induction motors with particular reference to the condition of imperfect rotor-bar-iron insulation. *Proceedings of IEE*, 116(5):737–751, 1969.

[98] R. Weppler. Ein beitrag zur berechnung von asynchronmotoren mit nichtisoliertem lauferkafig. *Archiv fur electrotechnik*, 1966.

[99] R. Carlson, C.A. da Silva, N. Sadowski, Y. Lefevre, and M. Lajoie-Mazenc. The effect of the stator-slot opening on the interbar currents of skewed cage induction motor. *IEEE Transactions on Magnetics*, 38(2):1285–1288, March 2002.

[100] P.J Holik, D.G. Dorrell, P. Lombard, H.-J. Thougaard, and F. Jensen. A multi-sliced finite element model for induction machines incorporating inter-bar current. *IEEE*, 2006.

[101] S. Williamson, C.Y. Poh, and A.C. Smith. Estimation of the inter-bar resistance of a cast-cage rotor. *Electric Machines and Drives Conference*, 2:1286–1291, 1–4 June 2003.

[102] A.M. Knight. Calculation of permeance harmonics from flux density Fourier series when the permeance periodicity differs from flux density periodicity. Unpublished notes, September 2006.

[103] S.G. Troitskaia, A.M. Knight, A. Merkhouf, and N. Stranges. Prediction of flux density and open circuit voltage in large skewed synchronous machines. *Industry Applications Conference, 40th Annual Meeting*, 4:2296–2301, October 2005.

[104] S. Williamson and T.J. Flack. Effect of radial rotor ventilation ducts on cage motor equivalent circuit parameters. *IEE Proceedings - Electric Power Applications*, 141(3):155–162, May 1994.

[105] A.M. Knight. Pole face loss in synchronous machines with skewed stators. May 2003.

Appendix A

Conformal transformations

Conformal transformations is a method that allows one to analytically represent a field within an arbitrary boundary. The method has been shown to predict field almost as accurately as FEA [61]. An example [57] is reviewed to illustrate the method and to give some insight into a model used in this work. The latter model is then considered in possible detail [58].

A.1 The idea of the method

An area inside a polygon can be mapped to an upper half plane of a so-called *w-plane*, with the polygon boundary stretched on the real axis (Fig. A.1). An equation called *Schwatrz-Christoffel transformation* governs this transformation:

$$\frac{dz}{dw} = A(w-a)^{\frac{\alpha}{\pi}-1}(w-b)^{\frac{\beta}{\pi}-1}...(w-e)^{\frac{\theta}{\pi}-1} \qquad \text{(A.1)}$$

where A is a constant, a, b, ..., e are coordinates of the polygon vertices on the real axis of the w-plane, and α, β, ..., θ are angles of the polygon in the xy-plane, else called z-plane. Integration of the equation with respect to w gives a coordinate z versus w, and constants of integration can be determined from boundary conditions.

This transformation might or might not be sufficient to analytically represent field in the original plane. Sometimes another, easily visualised, or "regular" field picture can be mapped to w-plane. Then w can be expressed from an equation of the regular field to be substituted into an equation of an arbitrary polygon. Thus w is eliminated, and one obtains dependence of an unknown field versus known. Thus desirable quantities such as electric scalar potential or magnetic flux density distribution can be obtained in the area of interest.

The boundary of the polygon has to be "cut" at some point, and the ends at the point of the "cut" become the ends of the real axis on the w-plane. The point of the cut is not included in the equation of transformation. A polygon may have discontinuity in a "vertex" or to be degenerated (to have

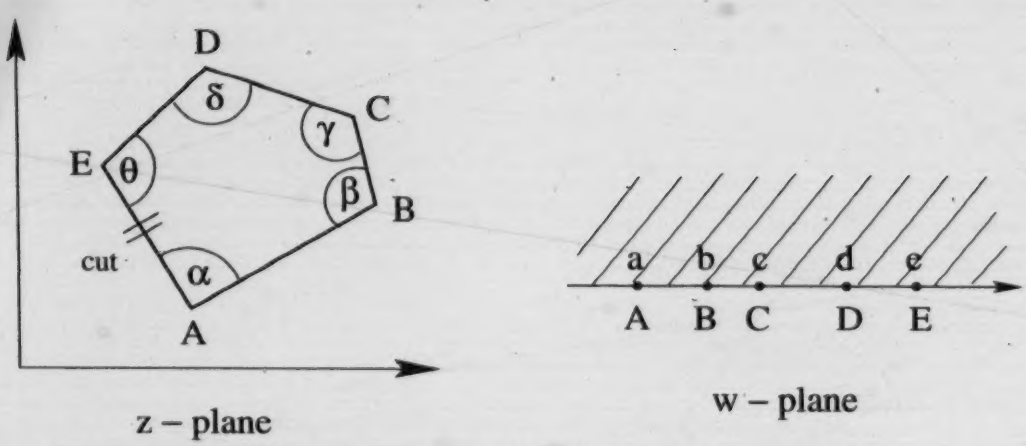

Figure A.1: Mapping from the z-plane to the w-plane.

zero internal area), when all surrounding space is the area of interest [57]. A point of discontinuity is most convenient to serve as the origin in the w-plane.

A.2 A symmetrical problem of the rectangular pole across the smooth armature

A problem of magnetic field in the air gap between an isolated rectangular pole and smooth armature surface has been first solved by F. W. Carter [57].

Transformation of a regular field to the w-plane. A rectangular capacitor with infinitely stretched plates of opposite polarity serves as a two-dimensional regular model (Fig. A.2). Assuming one end to be the origin in the w-plane, the other end can be "opened" to $w = -\infty$ and $w = +\infty$. The angle at the only corner of the polygon is zero. The transformation equation from this t-plane to the w-plane becomes

$$\frac{dt}{dw} = \frac{A}{w} \tag{A.2}$$

The integration by dw gives

$$t = A \ln w + B \tag{A.3}$$

At this step, B can be assumed to be zero. To have unity distance between the plates, A can be found from

$$j1 = A \ln(-1) = A\, j\pi \tag{A.4}$$

to be $A = \frac{1}{\pi}$. Then

$$t = \frac{1}{\pi} \ln w \tag{A.5}$$

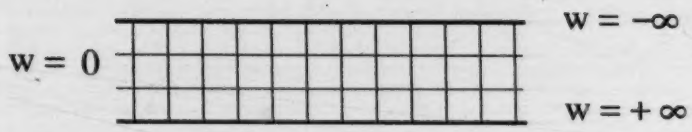

Figure A.2: A rectangular capacitor with infinitely stretched plates.

and

$$w = e^{\pi t} \tag{A.6}$$

The t-plane is often called *χ-plane.*

Configuration with one right angle. If the pole and the armature have the same length (Fig. A.3), use of symmetry can be made to simplify the problem. An x-axis can be put in the middle of the air gap; it is also an equipotential (Fig. A.4). Let the pole and the armature have unity potential of opposite polarity, then the x-axis will be at zero potential.

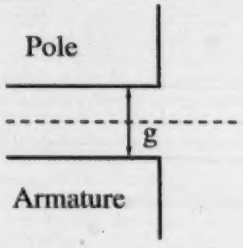

Figure A.3: The pole and the armature of the same length.

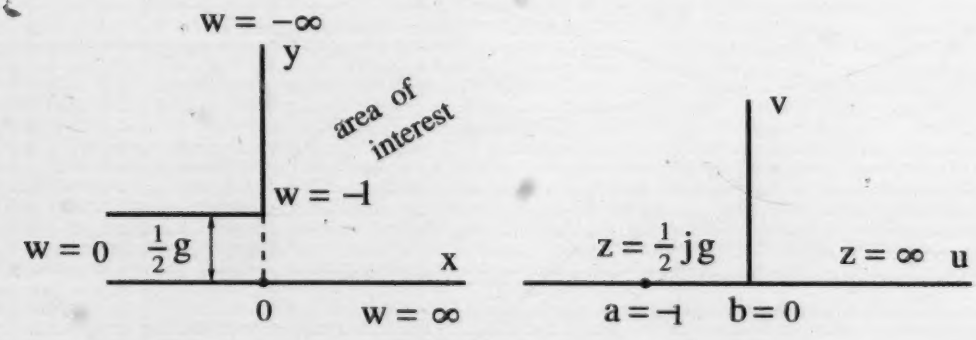

Figure A.4: The air gap in the z-plane and the w-plane.

Choose $w = 0$, when $x = -\infty$, $w = \infty$ when $x = \infty$, $w = -\infty$ when $jy = \infty$, $w = 1$ at the corner of the pole. There are two angles corresponding to two vertices of the polygon:

$$a = -1 \quad , \quad \alpha = \frac{3\pi}{2} \tag{A.7}$$

$$b = 0 \quad , \quad \beta = 0 \tag{A.8}$$

The transformation equation takes form

$$\frac{dz}{dw} = A(w-a)^{\frac{3}{2}-1}w^{-1} = \frac{A(w+1)^{\frac{1}{2}}}{w} \tag{A.9}$$

Integration by w yields

$$z = A\left(2(w+1)^{\frac{1}{2}} + \ln\frac{(w+1)^{\frac{1}{2}}-1}{(w+1)^{\frac{1}{2}}+1}\right) + B \tag{A.10}$$

The origin on the z-plane can be chosen arbitrarily, so assume $B = 0$. Checking the equation, at $w = -\infty$, $z = -j\infty$; at $w = \infty$, $x = \infty$; at $w = 0$, $z = A(2 - \ln\infty) = -\infty$.

To determine the constant A, consider an integral by z over the interval of $\frac{g}{2}$

$$\int_0^{\frac{1}{2}jg} dz = \frac{1}{2}jg \tag{A.11}$$

and assume that $w = re^{j\theta}$ where the radius r is small. When $r \to 0$,

$$dz = \frac{A(w+1)^{\frac{1}{2}}}{w}dw = A\frac{(re^{j\theta}+1)^{\frac{1}{2}}}{re^{j\theta}}jre^{j\theta}d\theta = A(re^{j\theta}+1)^{\frac{1}{2}}d\theta \to Ad\theta \tag{A.12}$$

and from

$$jA\int_0^{\pi} d\theta = jA\pi = \frac{1}{2}jg \tag{A.13}$$

one obtains

$$A = \frac{g}{2\pi} \tag{A.14}$$

Then

$$z = \frac{g}{2\pi}\left((2(w+1)^{\frac{1}{2}} + \ln\frac{(w+1)^{\frac{1}{2}}-1}{(w+1)^{\frac{1}{2}}+1}\right) \tag{A.15}$$

At the corner $w = -1$,

$$z = \frac{g}{2\pi}\ln(-1) = \frac{g}{2\pi}j\pi = \frac{1}{2}jg \tag{A.16}$$

which allows one to conclude that the origin in the z-plane is exactly below the pole corner.

The origin of the t-plane should correspond to $w = -1$, to be aligned with the origin of the z-plane. It was shown in [57] that the point $t = j\pi$ corresponds to $w = -1$.

Distribution of air gap flux density. If a picture of flux lines and equipotentials is drawn in each plane, a difference between two points should

be scaled going from plane to plane. So the air gap magnetic flux density can be calculated as

$$B = \left|\frac{dt}{dz}\right| \mu_0 F = \left|\frac{dt}{dz}\right| \mu_0 \tag{A.17}$$

for unity mmf F across the area of interest. This expression can be replaced by

$$B = \left|\frac{dt}{dw}\frac{dw}{dz}\right| \mu_0 \tag{A.18}$$

From (A.9) and (A.14)

$$\frac{dw}{dz} = \frac{2\pi}{g}\frac{w}{(w+1)^{\frac{1}{2}}} \tag{A.19}$$

From (A.6) $dw = \pi e^{\pi t} dt = \pi w dt$, and

$$\frac{dt}{dw} = \frac{1}{\pi w} \tag{A.20}$$

The expression for magnetic flux density becomes

$$B = \left|\frac{1}{\pi w}\frac{2\pi w}{g(w+1)^{\frac{1}{2}}}\right| \mu_0 = \frac{2}{g}\,\mu_0 \left|(w+1)^{-\frac{1}{2}}\right| \tag{A.21}$$

It is not feasible to draw magnetic flux density versus z directly. Instead, values of w can be picked, and z and B can be calculated using formulas (A.15) and (A.21). The graphs are the simplest, where w is real.

A.3 A problem of rectangular poles against the infinite smooth armature

One rectangular pole. A rectangular pole against an infinite plane of armature has been considered by Carter [58], as shown in Fig. A.5. The purpose of the exercise is to find the potential function (mmf) ϕ that provides potentials of the pole and the armature ϕ_0 and zero, respectively. The area of interest, air enclosed between the two surfaces, has been mapped to the second quadrant of the w-plane $\bar{w}o\eta$, where $w = a$ at the point A (corresponds to the point E), $w = 0$ at the point o (corresponds to the point P). Thus OA corresponds to the bottom of the pole PE, the line $A\bar{\xi}$ corresponds to Ey, $o\eta$ corresponds to $\bar{x}x$.

The transformation is given by

$$z = \frac{2g}{\pi}\left(\frac{\sqrt{a^2 - w^2}}{a} - \ln\left(\frac{a + \sqrt{a^2 - w^2}}{-w}\right) + i\frac{\pi}{2}\right) \tag{A.22}$$

where $z = x + iy$, $w = \xi + i\eta$, g is the air gap length.

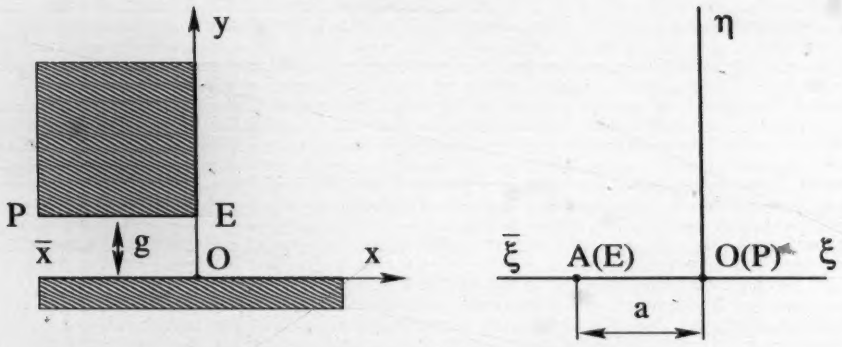

Figure A.5: Mapping from the z-plane to the $\psi\eta$-plane in a one-pole model.

If a function $\zeta = \phi + i\psi$ on the w-plane can be found such that it equals ϕ_0 along $o\bar{\xi}$ and zero along $o\eta$, then after it is transformed to the z-plane by the equation (A.22), flux lines $\psi = \text{const}$ and equipotential lines $\phi = \text{const}$ can be plotted on the original plane by x, y. Such a function is given by

$$\zeta = e^{\frac{\pi}{2} i \frac{\phi + \phi_0 + i\psi}{\phi_0}} \tag{A.23}$$

Denote $a = e^{\frac{\pi}{2}\frac{\psi_0}{\phi_0}}$. The equation for the z-plane becomes

$$z = \frac{2g}{\pi}\left(\sqrt{1 - e^{\pi i\left(\frac{\phi+\phi_0+i(\psi+\psi_0)}{\phi_0}\right)}}\right.$$
$$\left. - \ln\left[e^{\frac{\pi}{2}i\left(\frac{\phi-\phi_0+i(\psi+\psi_0)}{\phi_0}\right)} + \sqrt{e^{-\pi i\left(\frac{\phi-\phi_0+i(\psi+\psi_0)}{\phi_0}\right)} - 1}\right] + i\frac{\pi}{2}\right) \tag{A.24}$$

Thus given a pair (ϕ, ψ) on the w-plane, a corresponding point (x, y) on the z-plane can be obtained, and the field pattern in the area of interest can be drawn.

The flux density distribution along the armature surface can be determined as

$$B = \left|\frac{\partial\psi}{\partial x}\right| \tag{A.25}$$

when $y = 0$. On the armature surface, the potential function $\phi = 0$, and the expression (A.24) becomes

$$x = \frac{2g}{\pi}\left(\sqrt{1 + e^{-\pi\frac{\psi+\psi_0}{\phi_0}}} - \ln\left[e^{\frac{\pi}{2}i}\left(e^{\frac{\pi}{2}\frac{\psi+\psi_0}{\phi_0}} + \sqrt{1 + e^{\pi i\frac{\psi+\psi_0}{\phi_0}}}\right)\right] + i\frac{\pi}{2}\right)$$
$$= \frac{2g}{\pi}\left(\sqrt{1 + e^{-2X}} - \ln\left(e^X + \sqrt{1 + e^{2X}}\right)\right) \tag{A.26}$$

where

$$X = \frac{\pi}{2}\frac{\psi+\psi_0}{\phi_0} \tag{A.27}$$

Then

$$dX = \frac{\pi}{2\phi_0} d\psi \tag{A.28}$$

Taking derivative of x from the equation (A.26) by $d\psi$ and using (A.28), one can obtain

$$\frac{dx}{d\psi} = \frac{\pi}{2\phi_0}\frac{dx}{dX} = \frac{g}{\phi_0}\left(\frac{-e^{-2X}}{\sqrt{1+e^{-2X}}} - \frac{e^{X}}{\sqrt{1+e^{2X}}}\right) = -\frac{g}{\phi_0}\frac{e^{X}+e^{-X}}{\sqrt{1+e^{2X}}} \tag{A.29}$$

The flux density is the inverse of the expression (A.29): -see def of B in Gibbs, others

$$B = \frac{\partial\psi}{\partial x} = \frac{\phi_0}{g}\frac{\sqrt{1+e^{2X}}}{e^{X}+e^{-X}} = B_0\frac{1}{\sqrt{1+e^{-2X}}} \tag{A.30}$$

where $B_0 = \frac{\phi_0}{g}$ is flux density well under the pole. Given a range of X, values of x and B can be calculated from the equations (A.26) and (A.30), and the flux density waveform on the armature surface can be obtained.

Two rectangular poles. Carter [58] points out that magnetic flux density reduces to zero in the middle between two adjacent poles. That does not occur if the "one-pole" model above is used. The model can be corrected, assuming that the line in the middle of the interpole space has zero potential. Then the area of interest is bounded by the pole having the potential ϕ_0, and by the armature and the middle line, both of zero potential. The transformation from the w-plane to the z-plane is given by

$$z = \frac{g}{\pi}\ln\left[w + \frac{a-b}{2} + \sqrt{(w-a)(w-b)}\right] - \frac{c}{\pi}\arcsin\left[\frac{2ab}{(a+b)w} - \frac{a-b}{a+b}\right] \tag{A.31}$$

where

$$c = g\sqrt{\tfrac{a}{b}} \tag{A.32}$$

is a half of the distance between the poles on the xy-plane, a and b are coordinates of the corners of two poles on the w-plane (Fig. A.6). The potential function which reduces to ϕ_0 on the pole and to zero on the armature plane and the median line, is given by

$$\xi = e^{i\pi\frac{\phi+i\psi}{\phi_0}} \tag{A.33}$$

To obtain magnetic flux density on the armature surface, the function ξ is substituted into the equation (A.31) as before. Assuming $\phi = 0$ and $X = \pi\frac{\psi}{\phi_0}$, one can obtain

$$x = \frac{g}{\pi}\ln\left[e^{-X} + \frac{a-b}{2} + \sqrt{(e^{-X}+a)(e^{-X}-b)}\right] - \frac{c}{\pi}\arcsin\left(\frac{2ab}{a+b}e^{X} - \frac{a-b}{a+b}\right) \tag{A.34}$$

$$B = B_0\left(\frac{e^{-X}-b}{e^{-X}+a}\right)^{\frac{1}{2}} \tag{A.35}$$

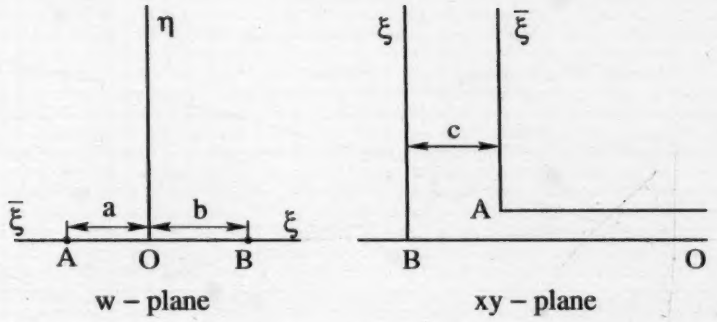

Figure A.6: Mapping from w-plane to xy-plane in a two-pole model.

The origin in Fig.5 has not been yet determined. To make $x = 0$ at the corner of the pole, a and b can be chosen as

$$a + b = 2e^{-\frac{\pi}{2}\frac{c}{g}} \tag{A.36}$$

Due to (A.32), they can be expressed as

$$a = \frac{2c^2}{c^2 + g^2} e^{-\frac{\pi}{2}\frac{c}{g}} \tag{A.37}$$

$$b = \frac{2g^2}{c^2 + g^2} e^{-\frac{\pi}{2}\frac{c}{g}} \tag{A.38}$$

The equations (A.34) and (A.35) allow to obtain the magnetic flux density distribution on the armature surface over the pole pitch, given a range of ψ and $X = \pi\frac{\psi}{\phi_0}$.

Appendix B

Calculation of eddy current loss density at one frequency

For a flux density harmonic at the frequency ω,

$$B = \hat{B}\sin(\theta - \omega t) \tag{B.1}$$

the volumetric eddy current loss density, (5.31), becomes

$$P_e = \frac{\sigma d^2}{12}\,\frac{1}{T}\int_T \left(\frac{dB}{dt}\right)^2 dt = \frac{\sigma d^2}{12}\,\frac{1}{T}\,(B_p\,\omega)^2 \int_T (\cos(\theta - \omega t))^2\,dt \tag{B.2}$$

Using a trigonometric identity

$$\cos^2\alpha = \frac{\cos 2\alpha + 1}{2} \tag{B.3}$$

the integral can be expanded to be

$$\int_T (\cos(\theta - \omega t))^2\ dt = \frac{1}{2}\int_T \cos 2(\theta - \omega t)\ dt + \frac{1}{2}\int_T dt =$$

$$-\frac{1}{2\omega}\sin(\theta - \omega t)|_T + \frac{T}{2} = 0 + \frac{T}{2} = \frac{T}{2}$$

and the volumetric eddy current loss density at the frequency ω becomes

$$P_e = \frac{\sigma d^2}{24}(B_p\,\omega)^2 \tag{B.4}$$

Appendix C

A product of two waves with axial phase shifts

When using the permeance model (see Chapter 4), a product of two waves, each with an axial phase shift, should be obtained. Suppose we have two sinusoidal waveforms,

$$A_1 \cos(m_1\theta + \theta_{1,0} + \alpha_1 z - \omega_1 t)$$

and

$$A_1 \cos(m_2\theta + \theta_{2,0} + \alpha_2 z - \omega_2 t)$$

with axial phase shifts $\alpha_1 = \frac{\beta_1}{l}$ and $\alpha_2 = \frac{\beta_2}{l}$, where β_1, β_2 are skews in radians, l is axial length. Using a trigonometric identity

$$\cos\alpha\cos\beta = \tfrac{1}{2}\left[\cos(\alpha+\beta) + \cos(\alpha-\beta)\right],$$

one can obtain a product as

$$\begin{aligned} &A_1 \cos(m_1\theta + \theta_{1,0} + \alpha_1 z - \omega_1 t) \times A_1 \cos(m_2\theta + \theta_{2,0} + \alpha_2 z - \omega_2 t) = \\ &\quad \tfrac{1}{2}A_1A_2\Big[\cos\big((m_1+m_2)\theta + (\theta_{1,0}+\theta_{2,0}) + (\alpha_1+\alpha_2) - (\omega_1+\omega_2)t\big) \\ &\qquad + \cos\big((m_1-m_2)\theta + (\theta_{1,0}-\theta_{2,0}) + (\alpha_1-\alpha_2) - (\omega_1-\omega_2)t\big)\Big] \end{aligned}$$

A product of two sinusoids yields a sum of two sinusoidal waveforms, with axial phase shifts that include a sum or a difference of skews.